**Title**
Tight-Binding Hamiltonians for Modeling Light Harvesting Systems



**Author**
Lee, Donghyun John

**Publication Date**
2018

Peer reviewed|Thesis/dissertation

**Tight-Binding Hamiltonians for Modeling Light Harvesting Systems**

by

Donghyun John Lee

A dissertation submitted in partial satisfaction of the

requirements for the degree of

Doctor of Philosophy

in

Chemistry

in the

Graduate Division

of the

University of California, Berkeley

Committee in charge:

Professor K. Birgitta Whaley, Chair
Professor Phillip L. Geissler
Professor Michael F. Crommie

Summer 2018

**Tight-Binding Hamiltonians for Modeling Light Harvesting Systems**

## Abstract

Tight-Binding Hamiltonians for Modeling Light Harvesting Systems

by

Donghyun John Lee

Doctor of Philosophy in Chemistry

University of California, Berkeley

Professor K. Birgitta Whaley, Chair

This thesis is concerned with tractable methods for modeling the optical and electronic properties of photosynthetic light harvesting complexes. We begin by investigating the validity of the commonly used Frenkel Exciton Hamiltonian, and find that it is inaccurate at the intermolecular distances commonly encountered in photosynthetic systems. We introduce semi-empirical tight-binding Hamiltonians and dynamics models that are better able to simulate the electronic properties of these chromophores at the proper distances and orientations. These models are validated by comparisons of the predictions to experimental results.

# Contents

# List of Figures

# List of Tables

## Acknowledgments

I would like to first thank my advisor Birgitta Whaley. This work would not have been possible without her support and guidance. I would also like to thank the postdocs Mohan Sarovar, Loren Greenman, and Aleksey Kocherzhenko for their help and advice, and the other members of the Whaley group for the thought provoking discussions that we've had. I am also grateful for all of the wonderful people that I've met throughout my journey, and I thank them for their support and friendship. Lastly, I thank my parents Jaemoon and Euna Lee for all of their love and support.

# Note on previously published work

The following chapters are adaptions of published papers:

- Chapter 3:
  Donghyun Lee, Loren Greenman, Mohan Sarovar, and K. Birgitta Whaley
  "Ab initio calculation of molecular aggregation effects: A coumarin-343 case study"
  Journal of Physical Chemistry A 2013, 117, 11072–11085.
  http://dx.doi.org/10.1021/jp405152h

- Chapter 4:
  Donghyun Lee, Michael A. Forsuelo, Aleksey A. Kocherzhenko, and K. Birgitta Whaley
  "Higher-energy charge transfer states facilitate charge separation in donor-acceptor molecular dyads"
  Journal of Physical Chemistry C 2017, 121, 13043-13051.
  http://dx.doi.org/10.1021/acs.jpcc.7b03197

# Chapter 1

# Introduction

Photosynthesis is the quantum mechanical process that provides the energy for nearly all life on earth. The light harvesting stage of photosynthesis begins with the absorption of a photon by a chromophore, followed by the transport of this electronic excitation energy to the reaction center (RC), and finally the separation of charges at the RC [1]. While the overall steps in this process are known, there is still much discussion regarding the underlying principles behind these photosynthetic properties [2–5]. The work described in this thesis is primarily motivated by the desire to understand the design principles that drives photosynthesis - in particular, how the geometric structure and quantum mechanical properties of chromophore aggregates affect their electronic and optical properties. In order to do so, it is important to begin with a quantum mechanical model that balances efficiency and accuracy.

## 1.1 Outline

### Motivation

This dissertation is focused on theoretical approaches for predicting the electronic and optical properties of chromophore aggregates. We evaluate the validity of these approaches by comparing their predictions to the experimental results obtained from artificial light-harvesting systems that have been synthesized in lab. In chapter 2, we derive the Frenkel exciton model Hamiltonian from first principles, and note all of the assumptions and approximations used throughout the derivation. In chapter 3 we assess the validity of the approximations made in the Frenkel exciton model by examining the regimes in which the model starts to fail for a chromophore dimer. We

introduce a new approach for constructing an improved tight-binding Hamiltonian that works well at the prototypical intermolecular distances and orientations found in photosynthetic chromophore aggregates. Chapter 4 describes and evaluates a tight-binding Hamiltonian model that treats both electronic excitation transfer and charge separation together. Chapter 5 introduces a methodology for quantifying the geometric disorder in a system, and uses the model in Chapter 3 to simulate linear absorption spectra. Ultimately, the collection of models presented in this dissertation provide a framework of theoretical tools for evaluating the electronic and optical properties of real experimental systems, which can be used to screen synthetic candidates for artificial photosynthetic systems.

## Chapter 2

The Frenkel exciton model is a tight-binding Hamiltonian that is commonly used for modeling chromophore aggregates. Starting from the Born-Oppenheimer molecular Hamiltonian, we derive this model while making note of the approximations and assumptions that are used. We state the prerequisite conditions that justifies these approximations, and comment on the implications of using these approximations.

## Chapter 3

We present time-dependent density functional theory (TDDFT) calculations for single and dimerized Coumarin-343 molecules in order to investigate the quantum mechanical effects of chromophore aggregation in molecular aggregate systems designed to function as artificial light-harvesting devices. Using the single-chromophore results, we describe the construction of effective Hamiltonians to predict the excitonic properties of aggregate systems. We compare the electronic coupling properties predicted by such effective Hamiltonians to those obtained from TDDFT calculations of dimers, and to the coupling predicted by the transition density cube (TDC) method. We determine the accuracy of the dipole-dipole approximation and TDC with respect to the separation distance and orientation of the dimers. In particular, we investigate the effects of including Coulomb coupling terms ignored in the Frenkel exciton tight-binding Hamiltonian. We also examine effects of orbital relaxation which cannot be captured by either of these models.

## Chapter 4

We simulate sub-picosecond charge separation in two donor-acceptor molecular dyads where it has previously been observed experimentally [6]. Charge separation

dynamics is described using a quantum master equation, with parameters of the dyad Hamiltonian obtained from density functional theory (DFT) and time-dependent density functional theory (TDDFT) calculations, and the rate of energy dissipation estimated from Ehrenfest-TDDFT molecular dynamics simulations. We find that higher energy charge transfer states must be included in the dyad Hamiltonian in order to obtain agreement of charge separation rates with the experimental values. Golden rule rate constants are found to be inadequate. Our results show that efficient and irreversible charge separation involves both coherent electron transfer from the donor excited state to higher energy unoccupied states on the acceptor and incoherent energy dissipation that relaxes the dyad to the lowest energy charge transfer state. The role of coherence depends on the initial excited state, with electron delocalization within Hamiltonian eigenstates found to be more important than coherence between eigenstates. We conclude that ultrafast charge separation is most likely to occur in donor-acceptor dyads possessing dense manifolds of charge transfer states at energies close to those of Frenkel excitons on the donor, with strong couplings to these states enabling partial delocalization of eigenstates over acceptor and donor.

## Chapter 5

We present molecular mechanics calculations on a prototype artificial light harvesting system consisting of chromophores attached to a tobacco mosaic virus (TMV) protein scaffold. These systems have been synthesized and characterized spectroscopically, but information about the microscopic configurations and geometry of these TMV-templated chromophore assemblies is largely unknown. We use a Monte Carlo conformational search algorithm to determine the preferred positions and orientations of two chromophores, Coumarin 343 together with its linker, and Oregon Green 488, when these are attached at two different sites (104 and 123) on the TMV protein. The resulting geometric information shows that the extent of disorder and aggregation properties, and therefore the optical properties of the TMV-templated chromophore assembly, are highly dependent on the choice of chromophores and protein site to which they are bound. We used the results of the conformational search as geometric parameters together with an improved tight-binding Hamiltonian to simulate the linear absorption spectra and compare with experimental spectral measurements. We found that using the geometries from the conformational search is necessary to reproduce qualitative features of the experimental spectral peaks.

## Chapter 6

We summarize the techniques for modeling chromophore aggregates that have been introduced in this thesis, and discuss some of the design principles for creating artificial photosynthetic systems that have been elucidated by using these techniques. We propose some topics of future research that would be interesting to investigate as an extension to the work in this thesis.

# Chapter 2

# Frenkel Exciton Hamiltonian

## 2.1 Molecular Hamiltonian

The most commonly used Hamiltonian for modeling an aggregate of chromophores is the Frenkel exciton model. In order to arrive at this model, we begin with the Born-Oppenheimer electronic Hamiltonian (in atomic units) [7]:

$$\hat{H}^{\mathrm{el}}(\mathbf{r},\mathbf{R}) = \hat{T}_{el}(\mathbf{r}) + \hat{V}_{el-nuc}(\mathbf{r},\mathbf{R}) + \frac{1}{2}\hat{V}_{el-el}(\mathbf{r},\mathbf{r}) + \frac{1}{2}\hat{V}_{nuc-nuc}(\mathbf{R},\mathbf{R}) \tag{2.1}$$

$$\begin{aligned}
\hat{T}_{el}(\mathbf{r}) &= -\frac{1}{2}\sum_{i\in\mathbf{r}} \nabla_i^2 \\
\hat{V}_{el-nuc}(\mathbf{r},\mathbf{R}) &= -\sum_{i\in\mathbf{r}}\sum_{j\in\mathbf{R}} \frac{Z_j}{|\vec{r}_i - \vec{R}_j|} \\
\hat{V}_{el-el}(\mathbf{r},\mathbf{r}) &= \sum_{i\in\mathbf{r}}\sum_{\substack{j\in\mathbf{r}\\ i\neq j}} \frac{1}{|\vec{r}_i - \vec{r}_j|} \\
\hat{V}_{nuc-nuc}(\mathbf{R},\mathbf{R}) &= \sum_{i\in\mathbf{R}}\sum_{\substack{j\in\mathbf{R}\\ i\neq j}} \frac{Z_i Z_j}{|\vec{R}_i - \vec{R}_j|}
\end{aligned}$$

where $\mathbf{r}$ is the set of electron indices, $\mathbf{R}$ is the set of nuclear indices, $\vec{r}_i$ is the position of the $i^{\text{th}}$ electron, $\vec{R}_i$ is the position of the $i^{\text{th}}$ nucleus, and $Z_i$ is the atomic number of the $i^{\text{th}}$ nucleus. $\hat{T}_{el}$ is the kinetic energy of the electrons, $\hat{V}_{el-nuc}$ is the attractive potential energy between electrons and nuclei, $\hat{V}_{el-el}$ is the repulsive potential energy

between electrons, and $\hat{V}_{nuc-nuc}$ is the repulsive potential energy between nuclei. This is the Hamiltonian over the electronic degrees of freedom, with respect to a fixed set of nuclear coordinates.

## 2.2 Frenkel Exciton Model

We assume that our system is composed of $N$ distinct chromophore molecules, where the set of electron and nuclear indices for chromophore $m$ are $\mathbf{r}_m$ and $\mathbf{R}_m$, respectively. We define the union of all $\mathbf{r}_m$ to be $\mathbf{r}_{tot}$, and the union of all $\mathbf{R}_m$ to be $\mathbf{R}_{tot}$. With this partitioning of indices, the electronic Hamiltonian for the full system can be rewritten as:

$$\hat{H}_{tot} = \sum_{m=1}^{N} \hat{H}_m + \sum_{m=1}^{N}\sum_{n=1}^{N}(\hat{V}_{el-el}(\mathbf{r}_m, \mathbf{r}_n) + \hat{V}_{el-nuc}(\mathbf{r}_m, \mathbf{R}_n) + \hat{V}_{nuc-nuc}(\mathbf{R}_m, \mathbf{R}_n)) \quad (2.2)$$

where $\hat{H}_{tot} = \hat{H}^{\text{el}}(\mathbf{r}_{tot}, \mathbf{R}_{tot})$, and $\hat{H}_m = \hat{H}^{\text{el}}(\mathbf{r}_m, \mathbf{R}_m)$. Eq. 2.2 separates all of the intramolecular interactions (first term) from the intermolecular interactions (second term). $\hat{H}_m$ is the electronic Hamiltonian for the isolated $m^{\text{th}}$ chromophore, with electronic eigenstates $\phi_a^{(m)}(\{\vec{r}_m\})$ and site energies $E_a^{(m)}$ that satisfy the time independent electronic Schrödinger equation:

$$\hat{H}_m|\phi_a^{(m)}\rangle = E_a^{(m)}|\phi_a^{(m)}\rangle \quad (2.3)$$

where the quantum number $a$ enumerates the electronic states of chromophore $m$. If we have the solutions (or approximate solutions) to Eq. 2.3, we can use these monomer wavefunctions to construct a trial wavefunction to solve for the full Hamiltonian using the linear variational method.

The first approximation in the Frenkel exciton model is that the chromophores are well separated enough such that they exhibit little to no wavefunction overlap. This assumption implies that the electrons on different chromophores are distinguishable, and therefore, no intermolecular electron exchange occurs. With this approximation, we can use a Hartree-Product ansatz to construct the $N$-chromophore basis functions

$$|\Phi_{\vec{a}}\rangle = \prod_{m=1}^{N} \phi_{a_m}^{(m)}(\{\vec{r}_m\}) \quad (2.4)$$

where $\vec{a} = (a_1, a_2 ... a_N)$ is an $N$-dimensional tuple, and $a_m$ indicates the electronic state of the $m^{\text{th}}$ chromophore. Thus, we can build our trial wavefunction as:

$$|\Psi_{\text{trial}}\rangle = \sum_{\vec{a}} c_{\vec{a}}|\Phi_{\vec{a}}\rangle \quad (2.5)$$

where the summation is over all possible quantum number permutations, and $c_{\vec{a}}$ are their corresponding probability amplitudes.

The second approximation we make is what is referred to as the Frenkel exciton model in the Heitler-London approximation, in which we only consider the interactions among states where a single chromophore is in it's first excited state (also called the singly excited subspace). Therefore we can amend our trial wavefunction to only include the singly excited subspace:

$$|\Psi_{\text{trial}}\rangle = \sum_{\vec{a}\in\mathcal{H}} c_{\vec{a}}|\Phi_{\vec{a}}\rangle \qquad\qquad \mathcal{H} = \{\vec{a} : \text{sum}(\vec{a}) = 1\} \tag{2.6}$$

The third approximation is to ignore the $V_{el-nuc}(\mathbf{r}_m, \mathbf{R}_n)$ and $V_{nuc-nuc}(\mathbf{R}_m, \mathbf{R}_n)$ terms in Eq. 2.2. This can be justified when the Frenkel exciton model Hamiltonian is used within the framework of an open quantum system model, in which the system of interest (chromophores) is treated separately from the surrounding environment (often a protein) [8]. The approximation is justified by asserting that the nuclei of neighboring chromophores are a part of the environment for a specific chromophore, and that any intermolecular interactions that involve nuclei will be included in the system-environment coupling term for that specific chromophore.

$$\hat{H}_{tot} = \sum_{m=1}^{N} \hat{H}_m + \sum_{m=1}^{N}\sum_{n=1}^{N} \hat{V}_{el-el}(\mathbf{r}_m, \mathbf{r}_n) \tag{2.7}$$

With these three approximations underlying the Frenkel exciton model, we can now begin to construct the secular determinant $(H - ES)c$ that arises from the trial wavefunction in Eq. 2.6. Note that our assumption of non-overlapping monomer wavefunctions implies that our basis functions are orthogonal, so the overlap matrix $S$ is the identity matrix.

The final step is to construct the matrix elements of $H_{tot}$ in the basis of our Hartree-Product wavefunctions

$$\langle\Phi_{\vec{a}}|H_{tot}|\Phi_{\vec{b}}\rangle = \sum_{m=1}^{N}\langle\Phi_{\vec{a}}|\hat{H}_m|\Phi_{\vec{b}}\rangle + \sum_{m=1}^{N}\sum_{n=1}^{N}\langle\Phi_{\vec{a}}|\hat{V}_{el-el}(\mathbf{r}_m, \mathbf{r}_n)|\Phi_{\vec{b}}\rangle \tag{2.8}$$

The first term is already diagonal in our basis:

$$\langle\Phi_{\vec{a}}|\hat{H}_m|\Phi_{\vec{b}}\rangle = E^{(m)}_{a_m}\prod_{l=1}^{N}\delta_{a_l,b_l} \tag{2.9}$$

Each summand within the double-summation of the second term is of the form:

$$\langle\Phi_{\vec{a}}|\hat{V}_{el-el}(\mathbf{r}_m,\mathbf{r}_n)|\Phi_{\vec{b}}\rangle = \sum_{i\in\mathbf{r}_m}\sum_{j\in\mathbf{r}_n}\langle\Phi_{\vec{a}}|\frac{1}{|\vec{r}_i-\vec{r}_j|}|\Phi_{\vec{b}}\rangle \tag{2.10}$$

$$= \left(\sum_{i\in\mathbf{r}_m}\sum_{j\in\mathbf{r}_n}\langle\phi^{(m)}_{a_m}\phi^{(n)}_{a_n}|\frac{1}{|\vec{r}_i-\vec{r}_j|}|\phi^{(m)}_{b_m}\phi^{(n)}_{b_n}\rangle\right)\prod_{l\neq m,n}^{N}\delta_{a_l,b_l} \tag{2.11}$$

where the indices $i$ and $j$ run over the electrons on chromophores $m$ and $n$, respectively. Since the electrons within a given molecule are identical and indistinguishable, and the electrons on differing molecules are distinguishable, each summand within the double-summation over all possible electron pairs in Eq. 2.11 will be identical. Thus, the summation can be replaced with a single term:

$$\sum_{i\in\mathbf{r}_m}^{m^{\text{elec}}_{\text{tot}}}\sum_{j\in\mathbf{r}_n}^{n^{\text{elec}}_{\text{tot}}}\langle\phi^{(m)}_{a_m}\phi^{(n)}_{a_n}|\frac{1}{|\vec{r}_i-\vec{r}_j|}|\phi^{(m)}_{b_m}\phi^{(n)}_{b_n}\rangle = m^{\text{elec}}_{\text{tot}}n^{\text{elec}}_{\text{tot}}\langle\phi^{(m)}_{a_m}\phi^{(n)}_{a_n}|\frac{1}{|\vec{r}_{m_1}-\vec{r}_{n_1}|}|\phi^{(m)}_{b_m}\phi^{(n)}_{b_n}\rangle \tag{2.12}$$

where $m^{\text{elec}}_{\text{tot}}$ and $n^{\text{elec}}_{\text{tot}}$ are the total number of electrons for the molecules $m$ and $n$, and $r_{m_1}$ and $r_{n_1}$ are the first electron coordinates for the molecules $m$ and $n$. Eq. 2.12 can be further simplified by using electron densities [9]:

$$m^{\text{elec}}_{\text{tot}}n^{\text{elec}}_{\text{tot}}\langle\phi^{(m)}_{a_m}\phi^{(n)}_{a_n}|\frac{1}{|\vec{r}_{m_1}-\vec{r}_{n_1}|}|\phi^{(m)}_{b_m}\phi^{(n)}_{b_n}\rangle$$

$$= m^{\text{elec}}_{\text{tot}}n^{\text{elec}}_{\text{tot}}\int\ldots\int\frac{\phi^{*(m)}_{a_m}(\{\vec{r}_m\})\phi^{(m)}_{b_m}(\{\vec{r}_m\})\phi^{*(n)}_{a_n}(\{\vec{r}_n\})\phi^{(n)}_{b_n}(\{\vec{r}_n\})}{|\vec{r}_{m_1}-\vec{r}_{n_1}|}\mathrm{d}\vec{r}_{m_1}\ldots\mathrm{d}\vec{r}_{m_{tot}}\mathrm{d}\vec{r}_{n_1}\ldots\mathrm{d}\vec{r}_{n_{tot}} \tag{2.13}$$

$$= \int\int\frac{\rho^{(m)}_{a_mb_m}(\vec{r}_{m_1})\rho^{(n)}_{a_nb_n}(\vec{r}_{n_1})}{|\vec{r}_{m_1}-\vec{r}_{n_1}|}\mathrm{d}\vec{r}_{m_1}\mathrm{d}\vec{r}_{n_1} \tag{2.14}$$

where the density of a single molecule is defined by:

$$\rho^{(m)}_{a_mb_m}(\vec{r}_{m_1}) = m^{\text{elec}}_{\text{tot}}\int\ldots\int\phi^{*(m)}_{a_m}(\{\vec{r}_m\})\phi^{(m)}_{b_m}(\{\vec{r}_m\})\mathrm{d}\vec{r}_{m_2}\ldots\mathrm{d}\vec{r}_{m^{\text{elec}}_{\text{tot}}} \tag{2.15}$$

Notice that the terms in Eq. 2.11 will appear for both the diagonal and off-diagonal matrix elements.

The fourth approximation made for the Frenkel exciton model is to ignore the perturbations that Eq. 2.11 makes to the diagonal site energies. This is made for

a similar reason as the third approximation - namely any perturbations to the site energies will be captured by the system-environment coupling terms.

We have defined all the matrix elements necessary to solve the secular equation under the stated approximations. After subtracting out the energy of the total ground state, we can express the new effective Hamiltonian as [10]:

$$\hat{H}_{\text{eff}} = \sum_{m=1}^{N} \varepsilon_m \sigma_m^\dagger \sigma_m + \sum_{m \neq n}^{N,N} J_{mn} \sigma_m^\dagger \sigma_n \tag{2.16}$$

$$\varepsilon_m = E_1^{(m)} - E_0^{(m)} \qquad J_{mn} = \int\int \frac{\rho_{01}^{(m)}(\vec{u})\rho_{10}^{(n)}(\vec{v})}{|\vec{u}-\vec{v}|} \mathrm{d}\vec{u}\mathrm{d}\vec{v} \tag{2.17}$$

where $\sigma_m^\dagger \equiv |\phi_1^{(m)}\rangle \langle \phi_0^{(m)}|$ is a Pauli creation operator for an excitation on chromophore $m$, and $\sigma_m \equiv |\phi_0^{(m)}\rangle \langle \phi_1^{(m)}|$ is a Pauli annihilation operator for an excitation on chromophore $m$. Eq. 2.16 is what is known as the Frenkel Hamiltonian (or Frenkel exciton model) in the Heitler-London approximation [11].

# Chapter 3

# Molecular aggregation effects beyond the Frenkel Exciton Hamiltonian

## 3.1 Introduction

The geometry of chromophore aggregates influences how they couple to one another, which in turn determines the electronic properties of the extended system. Deliberate control over the positions and orientations of chromophores can thereby be used to achieve specific properties such as efficient energy transfer [12]. Light harvesting in photosynthesis is an example from nature of how chromophores embedded in proteins have been optimized by evolution to capture light over a specific spectrum and to efficiently transfer the excitation energy to the photosynthetic reaction center [1, 5, 13, 14]. In designing synthetic light harvesting antennae for organic sensors or photovoltaics, it is critical to understand how the structural and orientational properties of the chromophore arrays affects their coupling, and hence their excitonic and optical properties [9, 15–19]. Importantly, recent work has suggested that quantum mechanical effects play a key role in the high efficiency of biological excitation energy transfer (EET) [3, 20–22]. Understanding the details of the quantum mechanical coupling between chromophores is an important step towards probing and exploiting any beneficial effects of quantum mechanical coherence in energy transfer.

Due to its spectroscopic attributes and small size, coumarin-343 (see Figure 3.1) is a molecule of particular interest for use in virus-templated synthetic light harvesting complexes, using *e.g.* the tobacco mosaic virus (TMV) protein scaffold [23]. The TMV protein monomers undergo self-assembly to form complex structures such

as helices and stacked disks [24]. The assembled TMV can be made into a light harvesting array by covalently attaching chromophores such as coumarin-343 onto the protein [23, 25–27]. The stacked disks and helical arrays of chromophores act as aggregate systems with optical properties (spectral width, peak absorption frequency) that differ from those of the free chromophore. It is possible to exercise a fine degree of control over these optical properties by changing the concentration of chromophores and the positions at which they are attached [28].

Conventionally the interaction between excited states of nearby chromophores is modeled using a tight-binding Hamiltonian of the form [14, 29],

$$H = \sum_{i=1}^{N} \epsilon_i \sigma_i^\dagger \sigma_i + \sum_{i \neq j}^{N,N} J_{i,j} \sigma_i^\dagger \sigma_j, \tag{3.1}$$

where $\epsilon_i$ is the transition energy of chromophore $i$, $J_{i,j}$ is the coupling between chromophores $i$ and $j$, $\sigma_i^\dagger \equiv |\psi_1^i\rangle \langle \psi_0^i|$ is a Pauli creation operator for an excitation on chromophore $i$, and $\sigma_i \equiv |\psi_0^i\rangle \langle \psi_1^i|$ is a Pauli annihilation operator for an excitation on chromophore $i$. In this approach each molecule is treated as a two-level system and the number of excitations is conserved. This truncated description of the intermolecular Hamiltonian is often referred to as the Frenkel Hamiltonian (or Frenkel exciton model) in the Heitler-London approximation [11]. Such effective Hamiltonian descriptions constitute the only feasible approach to study large molecular aggregates, since *ab-initio* methods cannot be scaled to such large systems. However, some of the parameters entering the effective Hamiltonian descriptions can be calculated using *ab-initio* methods. For instance, the coupling between chromophores ($J_{i,j}$), which is well-approximated by a Coulombic interaction between the transition densities of chromophores $i$ and $j$, can be calculated exactly using the transition density cube (TDC) method [30]. The most common way to approximate this coupling is by the ideal dipole approximation (IDA) [31] which treats the $1/r$ interaction between the two densities as an interaction between the dipole moments of the transition densities; several papers have compared the accuracy of the IDA to the more complete TDC description in various molecules [32–34]. The effective Hamiltonian in Eq. (3.1) relies on the approximation that the aggregate wavefunction can be reasonably constructed from the product of monomer wavefunctions (a Heitler-London-type picture). However such effective Hamiltonian descriptions may also neglect other potentially important aspects of the intermolecular interactions. In particular, Eq. (3.1) does not include electron exchange between the chromophores, nor does it allow for relaxation of the monomer wavefunctions. To go beyond this approximate description requires making detailed electronic structure calculations on the aggregate, and this is what we undertake in this study.

In the following sections we present time-dependent density functional theory (TDDFT) results for coumarin-343 and compare them to results from the IDA and TDC. We also compare to an effective Hamiltonian that we obtain from expressing the molecular Hamiltonian in a basis constructed from products of monomer wavefunctions. TDDFT provides a middle ground between accuracy and computational expense, and we have performed some benchmarking calculations to determine the quality of TDDFT for coumarin.

The results presented here are similar in spirit to a number of recent *ab-initio* studies of excited states of molecular aggregates, and we briefly review some of these studies here. Firstly, Ref. [35], which perhaps has the most overlap with the results in this work, develops a method referred to as TrEsp for using *ab-initio* calculations of charge and transition densities for monomers to determine energies of excited states of coupled chromophores. Next, some recent papers, *e.g.*, [36, 37], have examined the various components of electronic coupling in condensed media using *ab-initio* methods, separately characterized through-bond and through-space contributions, and analyzed the effects of solvent properties on these. Finally, several works have examined the aggregation mechanisms and subsequent excited states of molecular aggregates of dimers and extended systems using *ab-initio* methods [38–42]. These studies concentrate on aggregates common in molecular crystals (*e.g.*, perylene bisimide (PBI) aggregates) and as a result focus on very densely packed systems; typical inter-molecular separation distances studied in these works are in the range 2-8Å. In such self-assembling aggregates the mechanisms that dictate aggregation geometries and intermolecular potentials – *e.g.*, dispersion forces – are critical to understanding excited state energies. In contrast, in the papers cited above and in this work the focus is on molecular aggregates found in biomimetic or biological systems. In such systems the inter-molecular separation is typically larger, and critically, the forces that dictate aggregation are mostly due to external influences such as protein scaffolds. Therefore in such systems the intermolecular potentials play a smaller role although as we show below they cannot be ignored completely.

An outline of the remainder of this chapter follows. In section 3.3.1, we present these benchmarking calculations and give the TDDFT transition energies and transition dipoles for a single coumarin-343 chromophore. These are the simplest parameters which can be used in Eq. (3.1). Then, in section 3.3.2, we explore using TDDFT the energetics resulting from coupling between two dyes at a number of separation distances and orientations. We compare the TDDFT exciton splitting energies to splittings calculated by approximate methods, and also examine the effects of aggregation on exciton energies and wave functions, in particular, the role of orbital relaxation and deviations from the solutions to the Heitler-London description of monomer coupling.

## 3.2 Methods

The geometries of all the monomers considered in this report have been minimized using the B3LYP/6-31G* level of theory [43–46]. Single-point ground and excited-state energy calculations were then performed using TDDFT [47, 48] with the M06-HF [49], M11 [50], M11-L [51], and PBE [52, 53] functionals and the 6-31G* [44–46], 6-31+G* [44–46, 54], and 6-311G** [55, 56] basis sets. EOM-CCSD [57–59] calculations were performed to benchmark the density functionals, and multi-configurational self-consistent-field (MCSCF) [60] calculations were used to examine the presence of multireference character. The polarized continuum model (PCM) [61] was used to model the effects of water solvation. Range-corrected TDDFT [62] was also used to determine the energetic order of the charge-transfer states, which TDDFT predicts to be too low in energy. All calculations were performed using the GAMESS electronic structure package [63, 64], except for the transition density cube files (the one particle transition density projected onto a 3 dimensional cartesian grid) which were obtained from Q-Chem [65].

The calculations in this chapter use a modified coumarin-343 molecule which has an amide group that is necessary for attaching the dye on to the TMV substrate. For simplicity, in this work we shall refer to this modified molecule as coumarin-343-MA (coumarin-343-methylamide).

## 3.3 Results and Discussion

### 3.3.1 Single-chromophore benchmarking studies and parameter determination

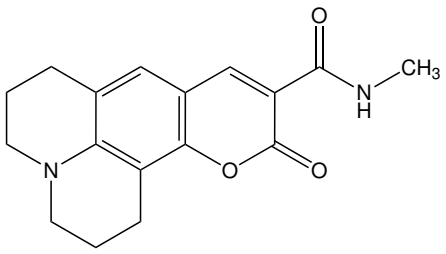


(a) Coumarin-343-MA

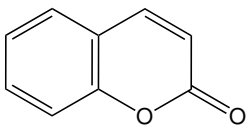


(b) Coumarin

Figure 3.1: (a) Structure of coumarin-343-MA, modified for attachment to TMV substrate. (b) The smaller coumarin molecule, on which we performed larger and more accurate calculations to benchmark the density functionals we used.

In order to choose an appropriate density functional and basis set for coumarin-343-MA, we first ran benchmarking calculations on coumarin (see Figure 3.1). We use the transition energy and the transition dipole moment to gauge accuracy, since these are the key quantities relevant in many effective Hamiltonian approaches. Four TDDFT functionals were compared with the more accurate EOM-CCSD method, and the results are summarized in Table 3.1.

| | | | $1^{st}$ Excited State | | $2^{nd}$ Excited State | |
|---|---|---|---|---|---|---|
| Basis Set | Functional | Ground State Energy [Ha] | Exc. Energy [eV] | $f$ | Exc. Energy [eV] | $f$ |
| 6-31G* | M06-HF | -496.8747 | 4.415 | 0.000 | 4.780 | 0.215 |
| | M11 | -496.7467 | 4.606 | 0.180 | 4.809 | 0.000 |
| | M11-L | -496.8800 | 4.152 | 0.052 | 4.407 | 0.000 |
| | PBE | -496.4380 | 3.625 | 0.000 | 3.822 | 0.060 |
| | B3LYP | -496.7418 | 4.182 | 0.111 | 4.396 | 0.000 |
| | EOM-CCSD | -495.5607 | 4.563 | 0.089 | 5.126 | 0.000 |
| 6-31+G* | M06-HF | -496.8921 | 4.457 | 0.000 | 4.699 | 0.241 |
| | M11 | -496.7619 | 4.548 | 0.197 | 4.848 | 0.000 |
| | M11-L | -496.8908 | 4.078 | 0.055 | 4.414 | 0.000 |
| | PBE | -496.4571 | 3.705 | 0.000 | 3.782 | 0.062 |
| | B3LYP | -496.7612 | 4.129 | 0.119 | 4.453 | 0.000 |
| | EOM-CCSD | -495.5870 | 4.497 | 0.098 | 5.121 | 0.000 |
| 6-311G** | M06-HF | -497.0182 | 4.481 | 0.000 | 4.707 | 0.239 |
| | M11 | -496.8850 | 4.552 | 0.181 | 4.775 | 0.000 |
| | M11-L | -497.0357 | 4.090 | 0.054 | 4.320 | 0.000 |
| | PBE | -496.5658 | 3.618 | 0.000 | 3.781 | 0.060 |
| | B3LYP | -496.8725 | 4.132 | 0.111 | 4.383 | 0.000 |
| | EOM-CCSD | -495.7996 | 4.502 | 0.095 | 5.068 | 0.000 |

Table 3.1: Density functional benchmarking for coumarin in the gas phase. The TDDFT excitation energies and oscillator strengths ($f$) for five functionals and three basis sets were compared with the EOM-CCSD results. The B3LYP functional matched both the excitation energy and the oscillator strength of EOM-CCSD within our tolerance. The results show only a very weak dependency to the choice of basis set.

For each basis set, the EOM-CCSD method predicts a first excitation energy of 4.5-4.6 eV and an oscillator strength of 0.09-0.10. The M11 functional is able to reproduce the excitation energy well, but it significantly overestimates the oscillator strength and transition dipoles. Since the accuracy of the transition dipole directly affects the accuracy of the chromophore couplings, the B3LYP functional offered a better combination of accuracy in the energetics and the transition dipoles. There is not a large basis set effect for the basis sets considered, and so we performed further calculations at the B3LYP/6-31G* level of theory.

We also check for multireference character, which occurs when multiple Slater determinants are needed to accurately express the zeroth-order wavefunction. This

is common for large or conjugated molecules. MCSCF calculations were run on coumarin-343-MA using an active space of 7 electrons in 7 $\pi$-orbitals. The natural orbital occupation numbers, which are the eigenvalues of the one-electron reduced density operator [66],

$$\gamma(r_1, r_1') = N \int \cdots \int \psi^*(r_1, r_2 \dots r_N)\psi(r_1', r_2 \dots r_N)\mathrm{d}r_2 \dots \mathrm{d}r_N, \tag{3.2}$$

are useful for determining multireference character; occupation numbers that deviate significantly from 0.0 or 2.0 indicate that a multireference wavefunction is needed. We find that the occupation numbers of the occupied and unoccupied orbitals were all greater than 1.9 or less than 0.12. This indicates that there is little multireference character for this dye and so the benchmark calculations and TDDFT calculations are both adequate.

| | | M06-HF | M11 | M11-L | B3LYP | B3LYP (Water) |
|---|---|---|---|---|---|---|
| Ground State Energy [Ha] | | -993.5938 | -993.3408 | -993.5986 | -993.2967 | -993.3128 |
| $1^{st}$ Excitation Energy [eV] | | 3.927 | 3.839 | 3.445 | 3.465 | 3.199 |
| Transition Dipole [Debye] | x | 0.062 | 0.070 | -0.014 | 0.000 | -0.076 |
| | y | -0.022 | 0.114 | -0.018 | 0.000 | 0.034 |
| | z | 7.228 | 7.029 | 6.101 | 6.706 | 7.611 |
| Oscillator Strength | | 0.778 | 0.729 | 0.486 | 0.591 | 0.703 |

Table 3.2: TDDFT results for Coumarin-343. The ground-state and excitation energies, transition dipoles, and oscillator strengths are given for each functional using the 6-31G* basis set. The PBE functional is not included as it performed poorly in the benchmark calculations on the coumarin molecule. The final column gives the B3LYP result using a continuum model to describe solvation in water.

The B3LYP/6-31G* excitation energies and transition dipoles for coumarin-343-MA are given in Table 3.2, together with results for the other functionals. At this level of theory, the first excitation energy is 3.465 eV and the oscillator strength is 0.591. The transition dipole between the ground and first excited states of coumarin-343-MA is pictured in Figure 3.2a. We see that the transition dipole lies flat along the plane of the molecule, on the axis formed between the center of the molecule and the nitrogen atom of the amide group.

### 3.3.2 Two-dye coupling calculations

Now we turn to assessing the magnitude of the coupling between excited states of pairs of molecules, where these are denoted as A and B. Using the benchmarking

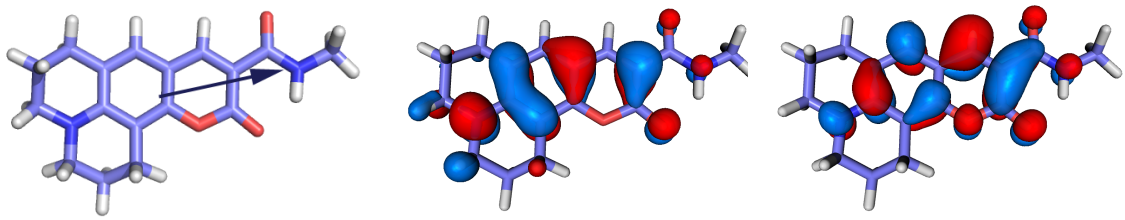

(a) transition dipole moment (b) HOMO (c) LUMO

Figure 3.2: (a) The transition dipole of coumarin-343-MA calculated at the TD-B3LYP/6-31G* level of theory. (b) The highest occupied molecular orbital (HOMO) of coumarin-343-MA. (c) The lowest unoccupied molecular orbital (LUMO) of coumarin-343-MA.

studies described in the previous subsection, we calculated the energetics of two coumarin-343-MA molecules at various separation distances and different relative orientations, using the B3LYP/6-31G* functional and basis set.

In order to systematically sample the possible dimer orientations, we begin with the molecules held at a fixed intermolecular separation along the x-axis. The transition dipole moment of each molecule is aligned along the z axis, with the plane of the molecule flat on the y-z plane as shown in the Parallel-0° geometry in Figure 3.10. The orientation of each molecule can be characterized by the three angles: the roll angle (rotation of the molecule about the transition dipole moment axis), the polar angle $\theta$, and the azimuthal angle $\phi$. These three angles correspond to the Euler angles $\alpha$, $\beta$, and $\gamma$, respectively. We have found that varying the roll angle does not affect the magnitude of coupling very much, since the roll angle does not change the direction of the transition dipole moment, therefore we do not sample over these angles.

To create our dimer geometries, we first fix the azimuthal angle of molecule A by constraining its transition dipole moment to lie on the x-z plane. We sample over the remaining 3 angular degrees of freedom: the polar angles $\theta_A$ and $\theta_B$, and the azimuthal angle $\phi_B$. These angles are defined in Figure 3.3a. Next, molecule A is rotated about the $y$-axis by $\theta_A$, and molecule B is rotated about the $(\hat{y}\cos\phi_B - \hat{x}\sin\phi_B)$ axis by $\theta_B$. In Figure 3.3b, we show examples of the resulting relative orientations possible for two chromophores.

In the following we will use $E_i$ ($\tilde{E}_i$) to denote the monomer (dimer) energies calculated using TDDFT.

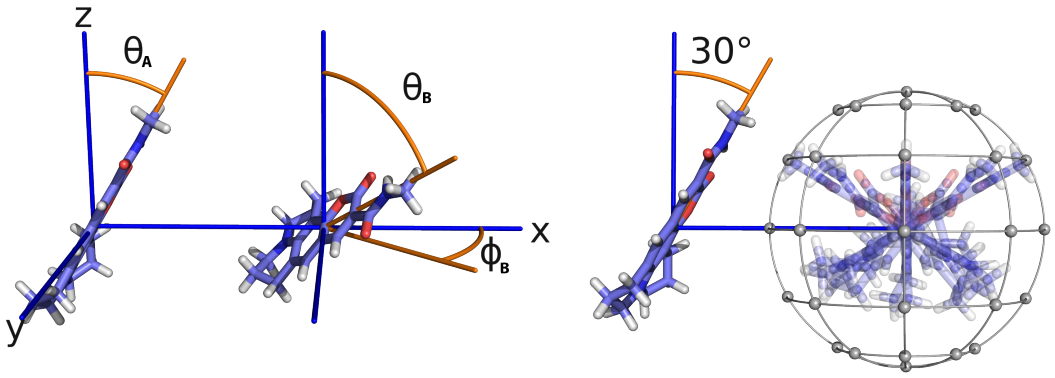


(a) Orientation angles for the chromophores.

(b) Example of dimer configurations where the polar angle of the first dye is held at 30°, while sweeping over the various relative orientations of the second dye.

Figure 3.3: Definition and examples of the three angles used to sample the relative orientations between two molecules.

For a homo-dimer, the tight-binding effective Hamiltonian of Eq. (3.1) reduces to

$$\hat{H} = \begin{array}{c} \\ \langle 10| \\ \langle 01| \end{array} \begin{array}{c} \begin{array}{cc} |10\rangle & |01\rangle \end{array} \\ \begin{pmatrix} \epsilon_0 & J \\ J & \epsilon_0 \end{pmatrix} \end{array} \tag{3.3}$$

in a basis of excitations on the left ($|10\rangle$) and right ($|01\rangle$) chromophores, where $\epsilon_0 = E_1 - E_0$ is the first excitation energy of the monomer and $J$ is the coulombic coupling between monomers. As mentioned in the Introduction, in the absence of exchange this coupling can be captured as the Coulomb interaction between transition densities (e.g. in the TDC method), and this can be further approximated as a dipole-dipole interaction (as in the IDA). Diagonalizing the matrix in Eq. (3.3) results in delocalized exciton states with symmetrically split energies, also known as Davydov splitting [67],

$$|\psi_\pm\rangle = \frac{|10\rangle \pm |01\rangle}{\sqrt{2}} \qquad \epsilon_\pm = \epsilon_0 \pm J. \tag{3.4}$$

W emphasize that this theory predicts a symmetric splitting of the exciton energies according to Eq. (3.4). In this section we will assess the degree to which TDDFT

calculations agree with the tight-binding effective Hamiltonian description of the excited states of the coumarin-343-MA homo-dimer. In particular, we will examine three specific aspects, for various chromophore separation distances and chromophore orientations: (i) we will compare the TDDFT description of the Coulombic coupling magnitude $J$ to the magnitudes provided by IDA and TDC, (ii) we will assess the validity of the form of the symmetric eigenstates given in Eq. (3.4), and (iii) we will assess the validity of the symmetric splitting of eigenenergies given in Eq. (3.4).

**Coulomb coupling energy**

Figure 3.7 shows the splitting of the excited state energies ($\frac{\tilde{E}_2-\tilde{E}_1}{2}$) for TDDFT as a function of the inter-chromophore separation distance for three different relative orientations. For comparison, we have also plotted the energetic splitting predicted by Eq. (3.4) when the Coulomb coupling $J$ is calculated using the IDA and TDC methods. Comparison of this predicted energetic splitting is the most consistent methods for comparing the three methods.

From Figure 3.7 we see that the numerically integrated TDC method agrees very well with the TDDFT calculations, while the IDA over-predicts for the 0° relative orientation (parallel and anti-parallel) and under-predicts for the 30° relative orientation. As the intermolecular separation increases, the IDA values begin to qualitatively match the TDDFT/TDC values after 12Å separation, however the convergence of the percent error is still quite slow. The percent error of the IDA splitting decreases to 10% only after 30Å separation (averaged over the three orientations). This shows that the IDA can be a poor description of Coulombic coupling for inter-chromophoric distances that are less than 30Å. More sophisticated methods such as TDC should be used in such cases. This conclusion is in agreement with Refs. [32–34].

Calculations where the relative orientation between dimers is explored while keeping the distance separation fixed were also done. In Figures 3.4 – Figure 3.6, we hold $\theta_A$ fixed and plot the coupling as a function of different relative orientations of the second dye. Our sampling scheme leads to 42 possible relative orientations of the second dye. Only half the sphere is shown because the reverse side was found to be quite symmetric due to the high symmetry of charge density across the plane of the page.

The results confirm that the TDC can reliably predict the energetic splittings. TDC systematically outperforms IDA, and is also able to predict the correct splitting in geometries where the molecules are nearly in contact with one another. In general, IDA overestimates for configurations that resemble H-aggregates (when $\theta_A$ is 0°) and underestimates for the configurations that resemble J-aggregates (when $\theta_A$ is 180°).

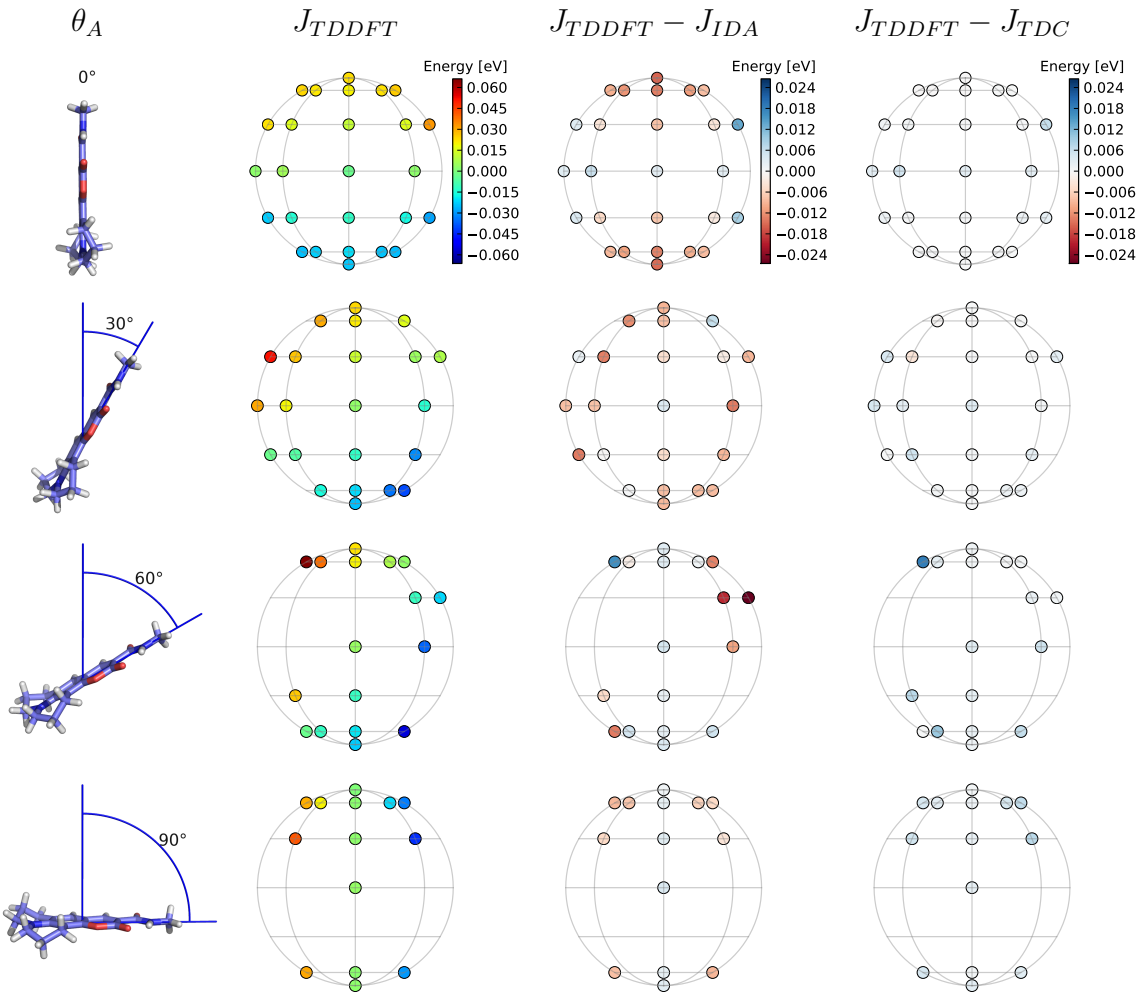


Figure 3.4: Dimer relative orientational dependence of electronic coupling at 9 Å separation. The first column depicts the polar orientation of the first molecule while the position on the polar plots on the right represents the orientation of the second molecule relative to the first (see Figure 3.3b). Columns 2-4 show the magnitude of $J_{\mathrm{TDDFT}}$, the value of the coupling given by TDDFT (column 2), the error resulting from the IDA approximation to this (column 3) and the error resulting from the TDC estimate (column 4), as a function of the relative orientation.

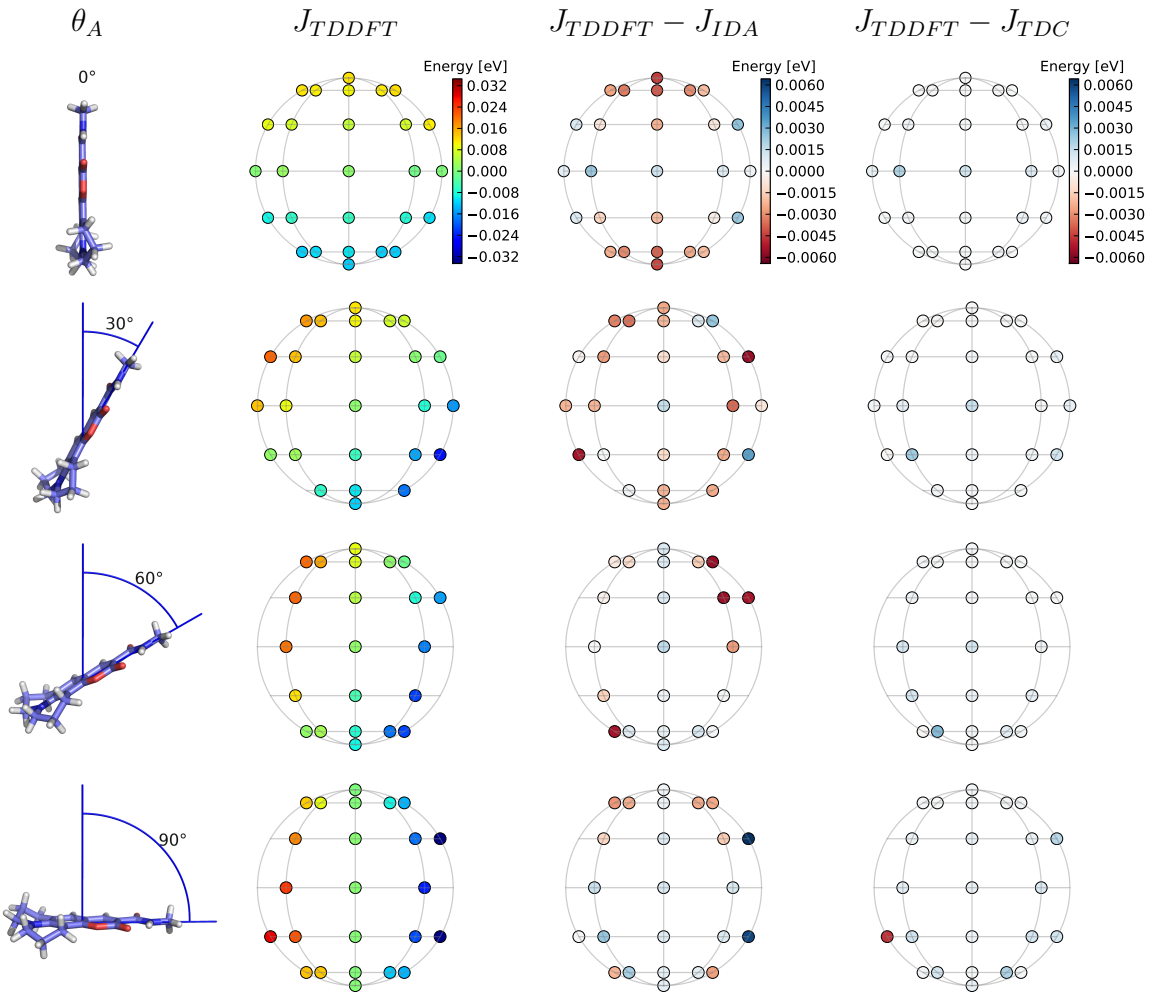


Figure 3.5: Dimer relative orientational dependence of electronic coupling at 12 Å separation. The first column depicts the polar orientation of the first molecule while the position on the polar plots on the right represents the orientation of the second molecule relative to the first (see Figure 3.3b). Columns 2-4 show the magnitude of $J_{\mathrm{TDDFT}}$, the value of the coupling given by TDDFT (column 2), the error resulting from the IDA approximation to this (column 3) and the error resulting from the TDC estimate (column 4), as a function of the relative orientation.

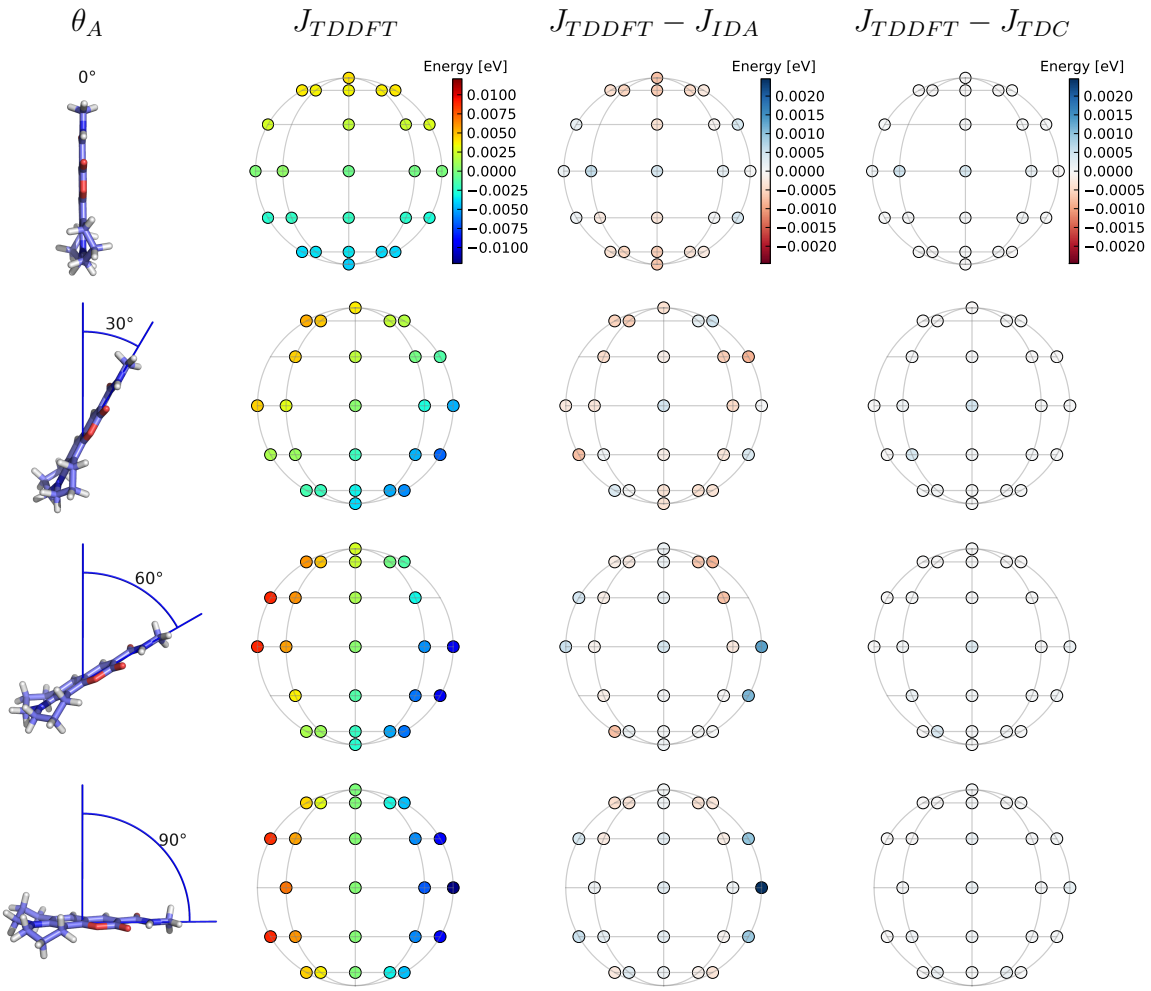


Figure 3.6: Dimer relative orientational dependence of electronic coupling at 18 Å separation. The first column depicts the polar orientation of the first molecule while the position on the polar plots on the right represents the orientation of the second molecule relative to the first (see Figure 3.3b). Columns 2-4 show the magnitude of $J_{\mathrm{TDDFT}}$, the value of the coupling given by TDDFT (column 2), the error resulting from the IDA approximation to this (column 3) and the error resulting from the TDC estimate (column 4), as a function of the relative orientation.

Since the IDA is by definition an approximation to the TDC coupling, the over and underestimation of IDA is due to the approximation of using a point dipole to approximate a charge density. The TDC coupling itself seems to perform well over most configurations, giving good agreement with the TDDFT results. There are a few data points for which TDC matches poorly to TDDFT; in these configurations, the spatial extent of the molecules overlaps enough to allow significant interaction between the two molecules.

**Exciton energies and site energy shifts**

Figure 3.8 shows TDDFT excitation energies as a function of inter-chromophore distance at three different orientations. The most striking feature of these plots is that the excitation energies split asymmetrically from the energy of the monomer excited state (indicated by the dashed line). This is in disagreement with the tight-binding effective Hamiltonian which predicts a symmetric splitting of the energies around the monomer energy (see Eq. (3.4)).

To explain this discrepancy we must re-examine the full molecular Hamiltonian of the coupled chromophore system. In a basis of single-chromophore ground states and single excitations,

$$|00\rangle = |\psi_0^A\rangle \otimes |\psi_0^B\rangle \qquad |10\rangle = |\psi_1^A\rangle \otimes |\psi_0^B\rangle$$
$$|11\rangle = |\psi_1^A\rangle \otimes |\psi_1^B\rangle \qquad |01\rangle = |\psi_0^A\rangle \otimes |\psi_1^B\rangle$$

where $|\psi_i^A\rangle \otimes |\psi_j^B\rangle$ indicates a direct product wavefunction between molecule A in state $i$ and molecule B in state $j$, the Born-Oppenheimer molecular Hamiltonian is written as [10]

$$\hat{H} = \begin{array}{c} \\ \langle 00| \\ \langle 10| \\ \langle 01| \\ \langle 11| \end{array} \begin{array}{c} \begin{array}{cccc} |00\rangle & |10\rangle & |01\rangle & |11\rangle \end{array} \\ \begin{pmatrix} 2E_0 + J_{\text{gs}}^{\text{gs}} & J_{\text{trans}}^{\text{gs}} & J_{\text{gs}}^{\text{trans}} & J_{\text{trans}}^{\text{trans}} \\ J_{\text{trans}}^{\text{gs}} & E_0 + E_1 + cJ_{\text{es}}^{\text{gs}} & J_{\text{trans}}^{\text{trans}} & J_{\text{es}}^{\text{trans}} \\ J_{\text{gs}}^{\text{trans}} & J_{\text{trans}}^{\text{trans}} & E_0 + E_1 + cJ_{\text{gs}}^{\text{es}} & J_{\text{trans}}^{\text{es}} \\ J_{\text{trans}}^{\text{trans}} & J_{\text{es}}^{\text{trans}} & J_{\text{trans}}^{\text{es}} & 2E_1 + J_{\text{es}}^{\text{es}} \end{pmatrix} \end{array} \tag{3.5}$$

where $E_i$ are the relevant monomer energies. Ignoring the effects of quantum mechanical exchange, which we have determined from the TDDFT calculations to be small at these distances, the coupling terms $J_i^j$ indicate coulomb integrals between either a charge or transition density on molecule A and either a charge or transition

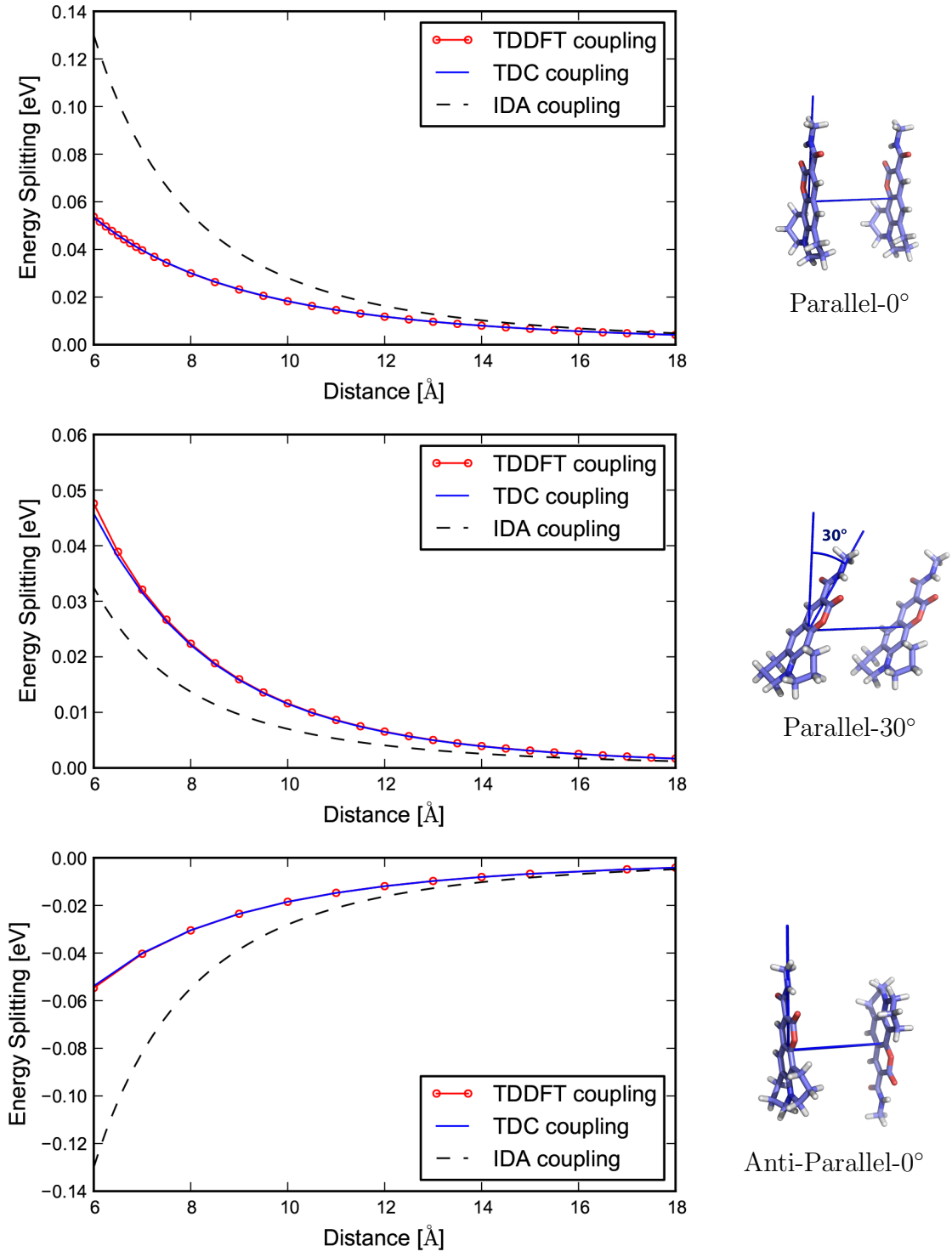


Figure 3.7: The energy splittings between the dimer excited states are shown for TDDFT, TDC and IDA calculations. The TDDFT points show $\frac{\tilde{E}_2-\tilde{E}_1}{2}$, while the TDC and IDA lines show $\frac{\epsilon_+-\epsilon_-}{2}$ with the $J$ coupling calculated using the respective approximation. The TDC and TDDFT predictions mostly overlap.

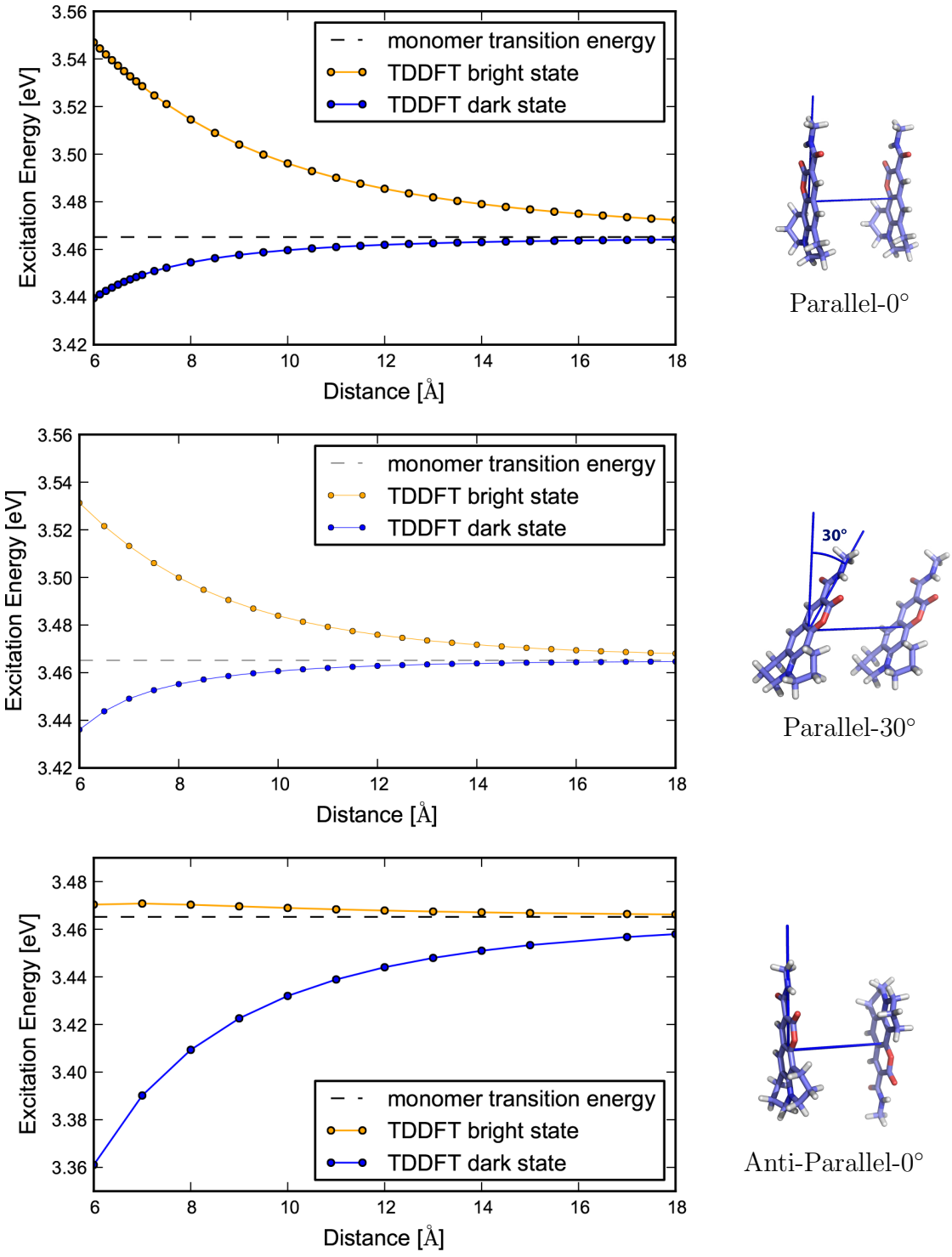


Figure 3.8: TDDFT excitation energies ($\tilde{E}_1 - \tilde{E}_0$ and $\tilde{E}_2 - \tilde{E}_0$) for the coupled excited states of the coumarin-343-MA dimer. Orientation of the dimer is shown to the right. Erroneous charge transfer states are not shown, since they do not mix into the optical states (explained in Figure 3.12).

density on molecule B, i.e.

$$J_{\mathrm{i}}^{\mathrm{j}} = \int \rho_i^A(r_1)\frac{1}{|r_1 - r_2|}\rho_j^B(r_2)\mathrm{d}r_1\mathrm{d}r_2. \tag{3.6}$$

with $i, j$ equal to either $gs$ (ground state charge density), $es$ (excited state charge density), or $trans$ (transition density). The charge densities and transition densities are defined for molecule A as

$$\rho_{\mathrm{gs}}^A(r_1) = N\int\cdots\int \psi_0^{A*}(r_1, r_2 \ldots r_N)\psi_0^A(r_1, r_2 \ldots r_N)\mathrm{d}r_2 \ldots \mathrm{d}r_N \times \sum_{n\in A} Z_n\delta(R_n - r_1) \tag{3.7}$$

$$\rho_{\mathrm{es}}^A(r_1) = N\int\cdots\int \psi_1^{B*}(r_1, r_2 \ldots r_N)\psi_1^B(r_1, r_2 \ldots r_N)\mathrm{d}r_2 \ldots \mathrm{d}r_N \times \sum_{n\in B} Z_n\delta(R_n - r_1) \tag{3.8}$$

$$\rho_{\mathrm{trans}}^A(r_1) = \int\cdots\int \psi_0^{A*}(r_1, r_2 \ldots r_N)\psi_1^A(r_1, r_2 \ldots r_N)\mathrm{d}r_2 \ldots \mathrm{d}r_N, \tag{3.9}$$

and similarly for molecule B, where $Z_n$ and $R_n$ correspond to the charge and positions of the nuclei in their respective molecules, and $N$ is the total number of electrons in a molecule. The coefficient $c$ is a parameter used to scale the magnitude of the ground-state/excited-state Coulomb integral (see discussion below).

In order to reduce this Hamiltonian into the tight-binding effective Hamiltonian in Eq. (3.3) a number of approximations must be made. Firstly, the Coulomb integrals are assumed to be much smaller than the energetic differences and therefore the matrix in Eq. (3.5) is approximated as block diagonal, with each block labeled by the number of excited states. Explicitly, $J_i^j \ll E_1 - E_0$ but $J_{\mathrm{es}}^{\mathrm{gs}} \approx J_{\mathrm{gs}}^{\mathrm{es}}$, and therefore we can ignore all off-diagonal terms except for those coupling $|10\rangle$ and $|01\rangle$. This approximation is sometimes referred to as the Heitler-London approximation in the literature [68]. Typically, the intermolecular Coulomb interaction terms are ignored i.e., one assumes that $J_{\mathrm{gs}}^{\mathrm{gs}} \approx J_{\mathrm{es}}^{\mathrm{gs}} \approx J_{\mathrm{gs}}^{\mathrm{es}} \approx 0$, and then the only Coulomb interaction terms that remain are the $J_{\mathrm{trans}}^{\mathrm{trans}}$ terms. Under this approximation the in the single excitation subspace (after a shift of the diagonal energies by $2E_0$) is the one given in Eq. (3.3),

$$\hat{H} - 2E_0 = \begin{array}{c} \\ \langle 10| \\ \langle 01| \end{array} \begin{array}{c} \begin{array}{cc} |10\rangle & |01\rangle \end{array} \\ \begin{pmatrix} \epsilon_0 & J_{\mathrm{trans}}^{\mathrm{trans}} \\ J_{\mathrm{trans}}^{\mathrm{trans}} & \epsilon_0 \end{pmatrix} \end{array} \tag{3.10}$$

with $\epsilon_0 = E_1 - E_0$.

We assess the validity of these approximations by evaluating the expanded $4 \times 4$ effective Eq. (3.5). In order to calculate the matrix elements of this larger we use

Mulliken partial atomic charges [69] for the ground state and excited state densities instead of density cubes. This is because density cube calculations are not constrained to reproduce the correct multipole expansion of the electron densities. These errors can be corrected for the transition density, as shown by Kreuger et al. [30], however the errors are more pronounced in the ground state and excited state densities, making them sensitive to the choice of grid resolution. In Figure 3.10, we show the results of using this expanded effective . It is evident from Figure 3.10 that we are able to reproduce the asymmetric shifts in excitonic energies using Eq. (3.5).

The primary effects that invalidate the approximations leading to Eq. (3.10) are electrostatic in nature. The neglect of the $J^{\text{es}}_{\text{trans}}, J^{\text{gs}}_{\text{trans}}, J^{\text{trans}}_{\text{es}}, J^{\text{trans}}_{\text{es}}$ and the $J^{\text{trans}}_{\text{trans}}$ terms coupling the ground state $|00\rangle$ to the two-exciton state $|11\rangle$ (Heitler-London approximation) is valid since these are much less than $E_1 - E_0$ at all the inter-chromophore distance scales we examined. However, the electrostatic corrections to the diagonal elements of Eq. (3.5), $J^{\text{gs}}_{\text{gs}}, J^{\text{gs}}_{\text{es}}, J^{\text{es}}_{\text{gs}}, J^{\text{es}}_{\text{es}}$, are significant and cannot be neglected. These are shifts to monomer energies due to the presence of the charges on the other chromophore. These electrostatic shifts are dependent on the inter-chromophoric distance and the exact orientation of the chromophores. Using the Mulliken partial atomic charge approach we are able to capture these electrostatic shifts and thereby get very good agreement with the TDDFT energies. The static dipole for the ground state and excited state both lie nearly parallel to the transition dipole moment. Consequently, the direction of the shifts is consistent with what is expected from the interaction of two electronic dipoles - the parallel dimers have a repulsive electrostatic effect while the anti-parallel dimers have an attractive effect.

While the asymmetric splitting is immediately captured by including these electrostatic distance-dependent shifts, scaling the ground-state/excited-state coulomb integrals by $c = 0.66$ is necessary in order to achieve quantitative agreement with the TDDFT energies. The value of this scaling factor is specific to a chromophore pair, but once determined for a particular orientation and distance separation, it holds for nearly all inter-chromophore separations and orientations. We have confirmed this by explicit calculation of energies at additional orientations and distances not presented in Figure 3.10. We interpret this parameter as the screening of the Coulomb integral by the other electrons in the molecular dimer.

We remark here that similar electrostatic shifts of proximal chromophores were identified in Ref. [70]. Such electrostatic shifts to monomer energies can be a significant source of disorder in multi-chromophoric assemblies. It is widely accepted that protein residues cause energetic shifts that are important for providing a favorable energetic landscape for energy transfer [71]. Our results indicate that in addition to the effect of the proteins, the electrostatic environment provided by neighboring chromophores should also be taken into account when calculating energetic shifts

and disorder in multi-chromophoric arrays. From a design perspective, this implies that the exact orientation and placement of chromophores are important not only for the precise engineering of the excitonic coupling between chromophores but also for engineering the energetic landscape.

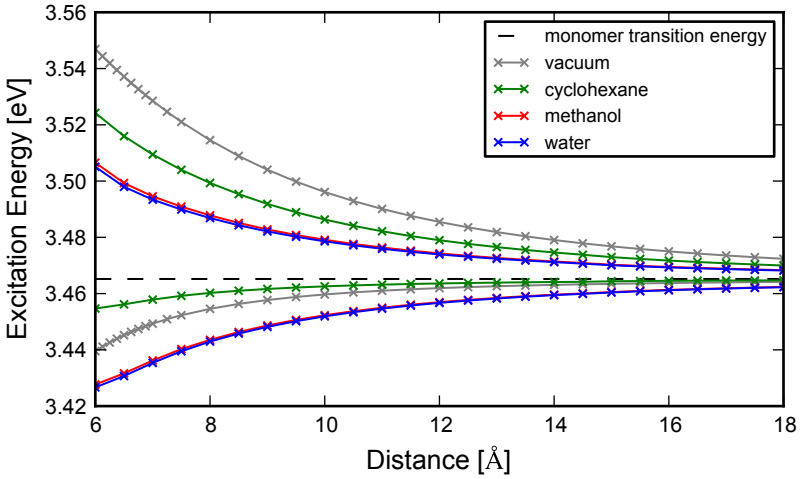


Figure 3.9: TDDFT excitation energies ($\tilde{E}_1 - \tilde{E}_0$ and $\tilde{E}_2 - \tilde{E}_0$) for the coupled excited states of the coumarin-343-MA dimer in various solvent environments (modeled using PCM). Only results for the parallel oriented dimer are shown.

We note that the electrostatic shifts identified here can be strongly affected by the polarity of the solvent [36]. In particular, charge screening by a polar solvent can reduce the value of electrostatic integrals such as $J_{\text{gs}}^{\text{es}}$. These integrals are likely to be more suppressed than the transition density integrals, e.g. $J_{\text{trans}}^{\text{trans}}$, and therefore the energy shifts can be suppressed even though the excitonic coupling (which is largely determined by $J_{\text{trans}}^{\text{trans}}$) may be only marginally effected by solvent screening [37]. To demonstrate this we calculated the excitations energies of the coumarin-343-MA homo-dimer in various solvent environments modeled using a polarizable continuum model (PCM). The results are shown in Figure 3.9 for the parallel oriented dimer. Clearly, as the polarity of the solvent increases the asymmetry of the excitation energy splitting around the monomer energy decreases. This demonstrates that it is important to integrate information about the solvent environment when modeling excitonic properties of molecular aggregates; solvent polarity will dictate the amount of influence electrostatic effects have on excitonic energies.

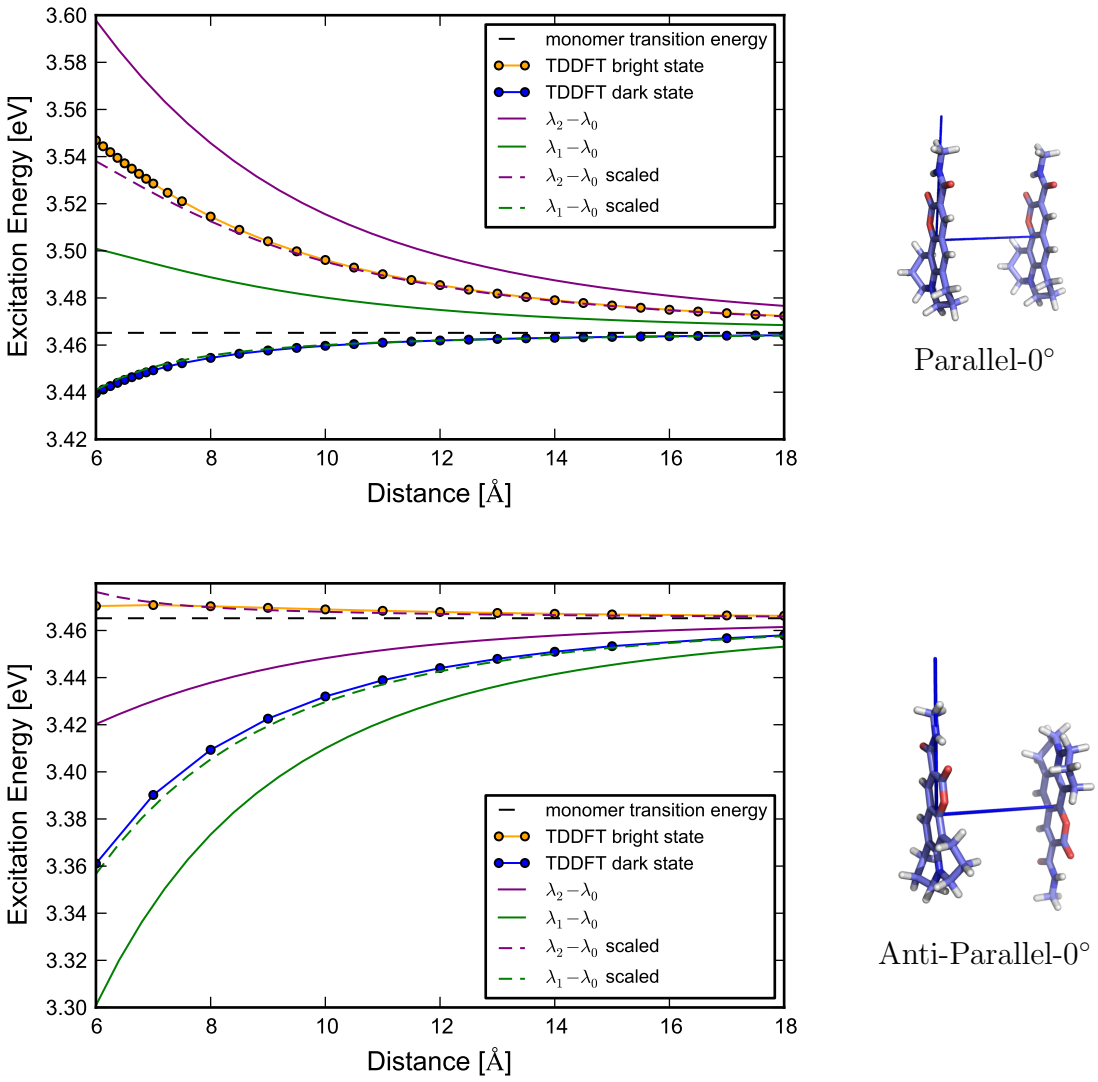


Figure 3.10: The energy levels calculated using TDDFT are together with the excited states of the 4x4 in Eq. (3.5). For the latter, the excited states are plotted as $\lambda_1 - \lambda_0$ and $\lambda_2 - \lambda_0$ where $\lambda_i$ is the $i^{\text{th}}$ eigenvalue.

**Exciton wave functions**

We now investigate the character of the TDDFT excited states to examine whether they are well described by products of monomer wavefunctions, as predicted by Eq. (3.4). The tight-binding effective description of the excited states can break down if either the dimer orbitals change with respect to the monomer orbitals, or the nature of the excited state changes significantly as a function of distance. The TDDFT excited states are written as linear combinations of basis functions which represent single-particle excitations from the DFT ground state. If the coefficients of this linear expansion are distance-dependent, the predictions of the effective in Eq. (3.3) are invalid. This is because the exciton wave functions in Eq. (3.4) are constructed from symmetric and anti-symmetric combinations of the monomer states (i.e. Eq. (3.4)), and are therefore independent of the magnitude of the coupling energy $J$ and hence of the inter-chromophoric separation. Figure 3.11 shows these coefficients for the bright state of the parallel orientation of the monomers as a function of distance. We see from this figure that the nature of the TDDFT excited state is relatively constant as a function of distance, until we get to small separation distances (below 8 Å). In particular, the dominant single-particle excitation, that from the highest occupied molecular orbital (HOMO) to the lowest unoccupied molecular orbital (LUMO) on each monomer, begins to change at intermolecular distances less than 8 Å. However, some of the other minor excitations which contribute to the TDDFT excited state begin to change gradually as a function of distance already at 12 Å.

Some of the single-particle excitations which contribute below 7 Å represent charge-transfer excitations from molecule A to molecule B. The existence of charge transfer, especially between 6 and 7 Å, is a feature present also for range-corrected TDDFT functionals (Figure 3.12). It is well known that TD-B3LYP is poor at predicting the energetics of charge transfer states, as are other functionals without 100% Hartree-Fock exchange [72, 73]. Figure 3.12 shows that TD-B3LYP predicts low-lying charge transfer states for the coumarin-343-MA dimer. However, the range-corrected DFT calculations show that the charge transfer states are much higher in energy. The splitting between the exciton states is consistent between B3LYP and the range corrected calculations. This suggests that the low lying charge transfer states predicted by B3LYP do not affect the character of the exciton states. Therefore, we may safely disregard these charge transfer states and use only the exciton states in our analysis.

In Figure 3.13, we show the overlap integral of the monomer molecular orbitals

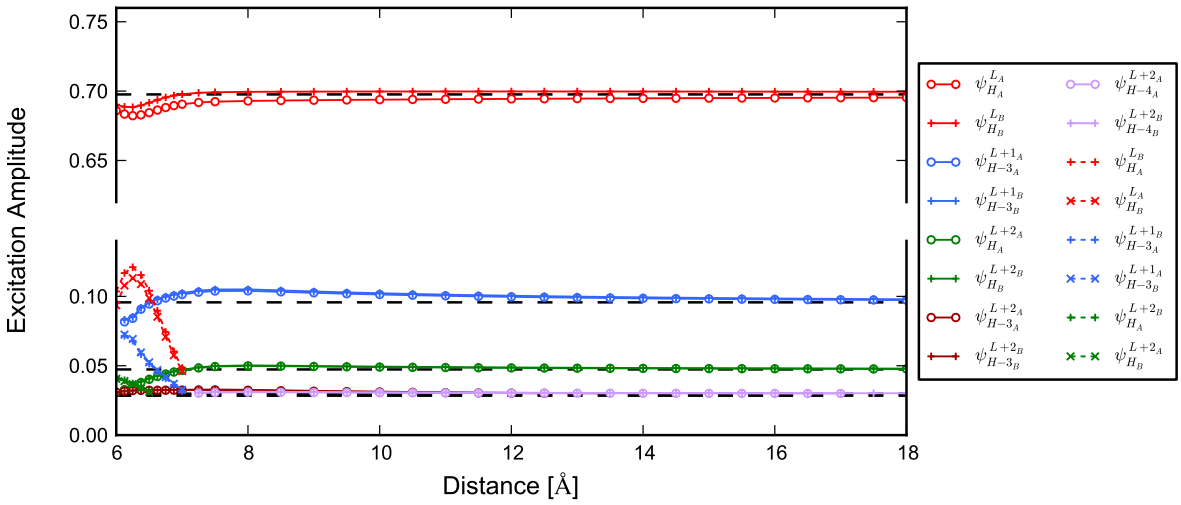


Figure 3.11: The expansion coefficients of the parallel-oriented bright state shown as a function of distance. Dashed lines represent the corresponding coefficients in the monomer TDDFT excited states. The top panel shows the dominant single-particle excitation, which corresponds to the excitation of an electron in the highest occupied molecular orbital (HOMO) to the lowest unoccupied molecular orbital (LUMO) of each monomer. The bottom panel shows other single-particle excitations which make up the TDDFT excited state. Molecular orbitals are labeled with respect to their energetic position below the HOMO ($H-n$) or above the LUMO ($L+n$). The excitations that are doubly degenerate (e.g. $\psi^{\mathrm{L}_A}_{\mathrm{H}_A}$ and $\psi^{\mathrm{L}_B}_{\mathrm{H}_B}$) have been averaged and plotted without their molecule index.

and the corresponding dimer orbitals,

$$\int \phi_n^{\mathrm{dimer}}(r)\phi_n^{\mathrm{monomer}}(r)\mathrm{d}r. \tag{3.11}$$

In the limit of infinite separation between the two dyes, each dimer molecular orbital is doubly degenerate, possessing unit overlap with a corresponding monomer molecular orbital. For the HOMO and LUMO, which are the most important orbitals in the bright state (Figure 3.11), the correspondence between monomer and dimer MOs is almost perfect for distances greater than 7 Å. Between 6 and 7 Å, these orbitals change by about 8% . Some orbitals change already at larger distances, such as the LUMO+1 and the LUMO+2 orbitals, which begin to deform as the intermolecular distance is decreased below 8 Å. Finally, the HOMO-3, which with the LUMO+1 forms the next most dominant excitation in the bright state, changes continuously

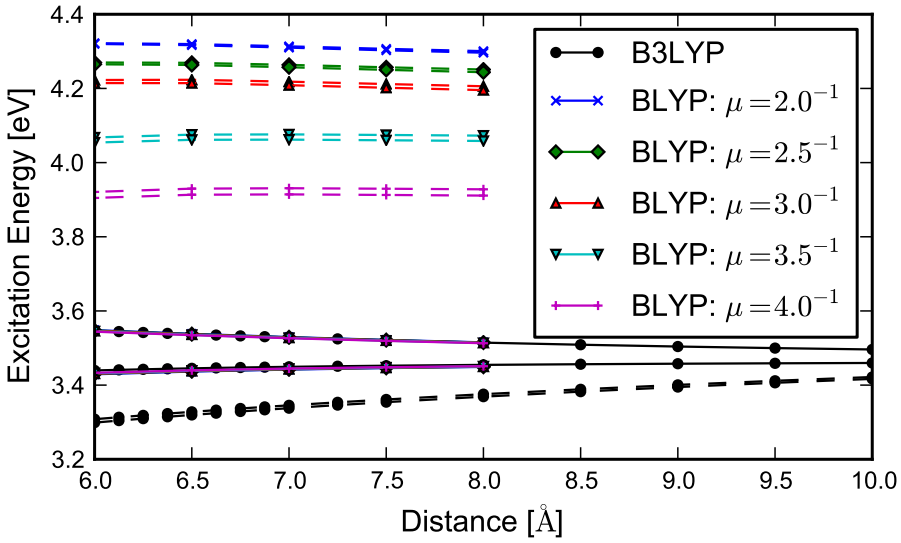


Figure 3.12: Coumarin-343 energy levels predicted by B3LYP and range-corrected BLYP. The coupled exciton states (solid lines) for B3LYP and the range corrected calculations are shown overlapped, while the energies of the charge transfer states (dashed lines) varies based on the functional. The range corrected BLYP energies have been shifted such that the first excited state energies of the monomer calculations are all aligned to that of B3LYP. This is done to compare the energies of the charge transfer states relative to the coupled exciton states.

at distances less than 18 Å; however, it changes by only 2% and furthermore it does not form the majority of the excited state, so this effect is diminished in the excited state energies and couplings.

To summarize this investigation of excited state wave functions, we find that for coumarin-343-MA, it is reasonable to describe the dimer wavefunctions in a basis of monomer wavefunctions for separation distances greater than 8 Å. For smaller distances the B3LYP calculations indicate possible mixing in of charge transfer character into the excited state wavefunction, although the extent of this mixing is not conclusive from this level of calculation.

## 3.4 Conclusions

In this work we have made a critical assessment of the conventional effective approach of modeling the excitonic properties of molecular aggregates, using the

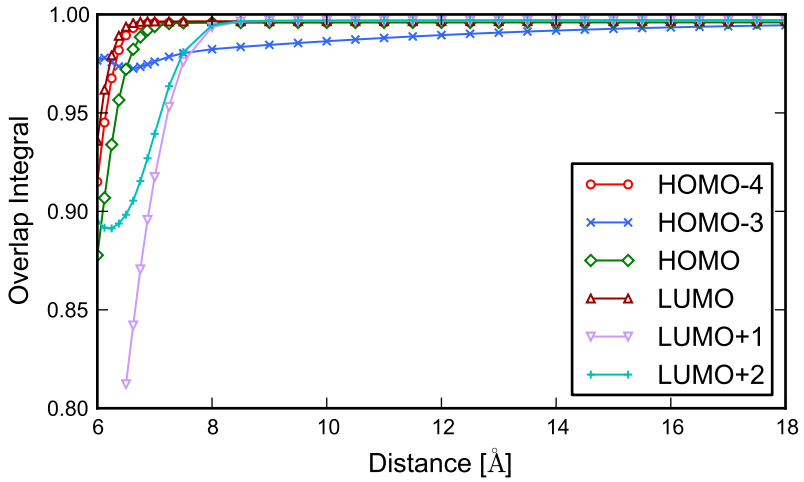


Figure 3.13: Overlaps of the bright state dimer molecular orbitals with their corresponding monomer molecular orbitals (See Eq. (3.11))

coumarin-343-MA dye as a case study. Results from *ab-initio* electronic structure calculations using TDDFT were compared with predictions from the conventional tight-binding effective for a homo-dimer (the Heitler-London approximation). Most interestingly, we found that the conventional effective for a homo-dimer does not reproduce the asymmetric energy splittings calculated using TDDFT. In particular, the ideal dipole approximation of the excited state coupling was found to give a very inaccurate representation of the TDDFT energy splittings. While the TDC method was found to perform much better, both the IDA and the TDC descriptions were found to be unable to reproduce the asymmetric nature of the splitting between bright and dark state energy levels that is predicted from TDDFT. We showed that this is a result of ignoring non-negligible electrostatic energy shifts resulting from the proximity of the two chromophores. We outlined a method for reincorporating these electrostatic shifts using a simple approach that only requires calculating Coulomb integrals based on Mulliken partial atomic charges. This approach is an efficient method for forming more complete effective descriptions that capture all the relevant physical effects; it only requires TDDFT calculations of dimers of chromophores (of each dimer combination of species present in the aggregate) and the remaining elements are accurately captured by Coulomb integrals. We find that the combination of a TDC description of the transition density coupling together with proper incorporation of electrostatic shifts produces an excellent effective description of excitonics in molecular aggregates. We also demonstrated the importance of

incorporating details of solvent polarity into the molecular aggregate model, since this also determines the degree of influence the electrostatic effects have on excitonic energies.

Additionally, we scrutinized the assumptions of the conventional Heitler-London tight-binding picture of excitonic coupling, by examining changes in the character of the excited state and the coupled molecular orbitals as a function of intermolecular distance. These effects were determined to be small but nonzero for intermolecular distances greater than 7-8 Å, while TDDFT predicts a significant departure from the Heitler-London picture at smaller distances. It also predicts some charge-transfer character at these smaller distances. In the future it would be useful to develop more reliable estimates of this charge-transfer character [15] in order to analyze the interplay between excitonic and charge transfer states in chromophore arrays relevant to natural photosynthesis, such as, e.g., the bacterial reaction center [74].

We expect that our investigation and refinement of effective Hamiltonian descriptions of molecular aggregates will inform the modeling of large molecular aggregates formed by direct aggregation or aggregation by protein templated assembly. Such aggregates show promise as the basis for next-generation light harvesting or sensing devices with tailored properties, and efficient modeling of their excitonic properties through effective Hamiltonians will be important for rational design and engineering of such devices.

# Chapter 4

# Unified description of excitation energy transfer and charge separation

## 4.1 Introduction

Organic photovoltaic (OPV) cells can be low-cost, light-weight, and flexible, making them a promising alternative to silicon based photovoltaic cells.[75, 76] The power conversion efficiencies of the best OPV cells has recently exceeded 10% [77, 78], yet this is still far from the theoretical limit of efficiency (20-24%) for single-junction OPV cells.[79] Typical organic semiconductors have low dielectric constants,[80] usually in the range 2–5 vs. 11.7 for bulk monocrystalline silicon.[81] Consequently, electrostatic interactions between charges in organic materials are not effectively screened, and interaction with light predominantly produces excitons (Coulomb-bound electron-hole pairs), rather than free charge carriers.[82] To generate a current in an OPV cell, the electron and the hole that form an exciton must move in opposite directions. However, the exciton binding energy often exceeds the available thermal energy by an order of magnitude or more.[83] The energy needed for spatially separating the electron and the hole is therefore typically supplied by the local electric field at an interface between a domain of electron-donating and electron-accepting molecules (D-A interface).

One factor limiting the efficiency of OPV cells is the bimolecular recombination of excitons before they reach a D-A interface.[84] To minimize recombination, typical OPV cells rely on bulk heterojunctions: purposely disordered blends of electron-donor and electron-acceptor materials with linear dimensions of donor and acceptor

domains smaller than the exciton diffusion length.[85] However, the morphology of such structures is difficult to control precisely. Furthermore, small donor and acceptor domains are often thermodynamically unfavorable, and phase segregation of the donor and the acceptor molecules may lead to a decrease in the efficiency of OPV cells over time.[86] It is possible to avoid these problems by using covalently bound donor-acceptor dyads (as well as triads or higher polyads that offer more control over charge separation and could also find applications in molecular electronics).[4, 6, 87–89]

Recent experiments have shown that charge separation on ultrafast timescales below 100 fs occurs in a variety of donor-acceptor dyads and of blends where the donor and acceptor species are not covalently bound.[6, 87, 88, 90–94]. It has been suggested that the rate of charge separation in such donor-acceptor blends is limited by diffusion of excitons to the D-A interface, and that excitons that are formed close to the D-A interface are responsible for ultrafast charge separation.[95] However, even in the case of donor-acceptor dyads, where all excitons are necessarily formed directly at the D-A interface, the rate of charge separation can vary significantly and depends on the strength of coupling between orbitals that are occupied by the electron and the hole in the initial excited state and in the charge separated state.[87] Based on spectroscopic studies and calculated magnitudes of electronic couplings, it has been suggested that in blends of organic molecules and fullerene derivatives the rate of electron transfer from the excited states on the donor to higher energy unoccupied states on the acceptor is higher than the rate of electron transfer to the acceptor LUMO. [94, 96] However, such studies do not address the details of electron dynamics at D-A interfaces in ultrafast charge separation processes. A better theoretical understanding of the dynamics of excited state evolution during charge separation would provide a basis for the rational design of more efficient photovoltaic materials.

In this chapter, we model the dynamics of ultrafast charge separation in two donor-acceptor dyads (Figure 4.1) that have been synthesized and characterized experimentally by Pillai, et. al.[6] The electron donor is a carotenoid for both dyads; the electron acceptor is a Zn-porphyrin derivative for dyad 1 and a fullerene derivative for dyad 2. Although in both dyads charge separation occurs on timescales below 1 ps, transient absorption spectroscopy measurements have shown that the rate of this is 1.2-3 times faster for dyad 2 than for dyad 1.[6] Investigation of the reason for this difference in charge separation rates using calculations based on a quantum master equation model shows that charge separation in these donor-acceptor dyads occurs via multiple higher-energy charge transfer states. We also analyze the significance of coherence for electron transfer from the donor to the acceptor, and characterize its dependence on the nature of the initial excitation. Our results show

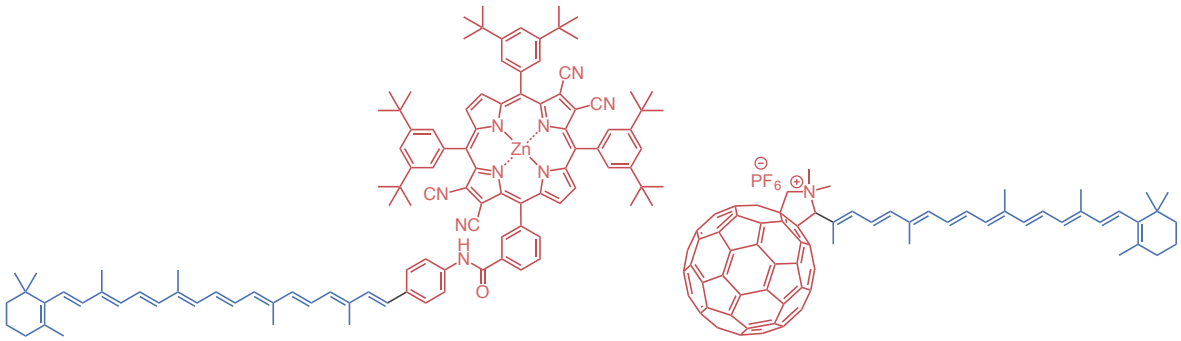


(a) Dyad 1 (b) Dyad 2

Figure 4.1: Molecular structures of dyads 1 and 2. The donor fragment (shown in blue) is a carotenoid for both dyads, and the acceptor fragment (red) is a porphyrin for dyad 1 and fullerene for dyad 2.

that higher energy acceptor states must be included in simulations in order to obtain accurate charge separation rates and reveal key design principles for optimizing ultrafast charge separation.

## 4.2 Methods

We simulated charge transfer in two molecular dyads (Figure 4.1) that have been synthesized and spectroscopically studied by Pillai et al.[6] The geometries of both dyads were optimized using the Q-Chem electronic structure package's implementation of density functional theory (DFT), with the B3LYP hybrid exchange-correlation functional and the 6-31G* basis set.[97] Each dyad was partitioned into a donor and an acceptor fragment. The donor fragment (shown in blue in Figure 4.1) is a carotenoid for both dyads, and the acceptor fragment (shown in red in Figure 4.1) is a porphyrin derivative for dyad 1 and a fullerene derivative for dyad 2. The boundary between the donor and acceptor fragments was chosen so that the donor fragment has similar electronic properties in both dyads.

Transient absorption spectroscopy has been used to track the electron and exciton dynamics in both dyads after an initial excitation to the (bright) second excited state of the carotenoid (donor).[6] For carotenoids, the lowest energy excited state is typically a (dark) double excitation state that is not captured by standard time-dependent density functional theory (TDDFT) calculations[98]. Experimental results suggest that the initial excitation can undergo efficient internal conversion, on a timescale of the order of 100 fs, to the lowest-energy carotenoid excited state.

However, charge separation from this state has a timescale of about 11 ps for dyad 1 and is also on the order of several picoseconds for dyad 2.[6] This state acts as a trap state and decreases the yield of subpicosecond charge separation that is the focus of our study, but does not significantly affect its dynamics. Therefore, we do not include this state in the simulations presented in this chapter.

The carotenoid's orbitals are well separated in energy, therefore higher excited states on the donor fragment are not significantly populated during the charge separation process. Only the lowest two single-excitation states on the carotenoid contribute to ultrafast charge separation and thus need to be included in the simulations.

For dyad 1, transient absorption spectroscopy suggests that exciton transfer from the donor to the acceptor fragment is negligible.[6] This is likely due to the low transition dipole strength of the Q-band in porphyrins, which is an order of magnitude smaller than in structurally similar materials that are known for efficient energy transfer, such as chlorophylls, pyropheophorbides, and phthalocyanines.[99] Therefore, excitons localized on the acceptor need not be included in simulations of charge separation in dyad 1.

For dyad 2, the rate of resonant energy transfer between the donor and the acceptor fragments is comparable to the rate of valence electron transfer, but the rate of hole transfer from the acceptor to the donor is an order of magnitude smaller.[6] Consequently, excitons localized on the acceptor have a negligible direct contribution to charge separation in dyad 2: rather, they can undergo efficient energy transfer back to the donor, followed by efficient electron transfer to the acceptor. Because energy transfer between the acceptor and the donor is not a rate-limiting step, excitons localized on the acceptor have little effect on the rate of charge separation. Therefore, these states do not need to be included in simulations of charge separation in dyad 2.

The two Frenkel exciton states on the carotenoid that are populated within the first 100 fs of excitation can transfer the excited electron to a number of unoccupied acceptor orbitals. In our simulations, we include as many lowest-energy charge transfer (CT) states with the hole on the donor and the electron on the acceptor as are necessary for convergence of the charge separation rates: 20 CT states for dyad 1 and 28 CT states for dyad 2. The complete basis set for our charge separation simulations consists then of two Frenkel excitons localized on the donor fragment, and charge transfer states with the electron on the acceptor and the hole on the donor. We will henceforth refer to the Frenkel exciton states with the electron in the donor LUMO or LUMO+1 as $\mathrm{Exc}_1$ and $\mathrm{Exc}_2$, respectively, and to the charge transfer states, enumerated by increasing energy, as $\mathrm{CT}_3$, $\mathrm{CT}_4$, ..., $\mathrm{CT}_N$ ($N = 22$ for dyad 1 and $N = 30$ for dyad 2).

Using this basis set, we construct a tight binding Hamiltonian for the dyad:

$$\hat{\mathrm{H}} = \sum_{i=1}^{N} \varepsilon_i \hat{\mathrm{a}}_i^\dagger \hat{\mathrm{a}}_i + \sum_{i=1}^{N} \sum_{j=1}^{i-1} J_{ij} \left( \hat{\mathrm{a}}_i^\dagger \hat{\mathrm{a}}_j + \hat{\mathrm{a}}_i \hat{\mathrm{a}}_j^\dagger \right), \tag{4.1}$$

where $\hat{\mathrm{a}}_i^\dagger$ and $\hat{\mathrm{a}}_i$ are creation and annihilation operators, respectively, for basis state $i$, $\varepsilon_i$ is the energy of state $i$, and $J_{ij}$ is the coupling between states $i$ and $j$.

For excitonic states, $\mathrm{Exc}_i$ $(i = 1, 2)$, $\varepsilon_i$ are given by the TDDFT excitation energies that correspond to the HOMO-LUMO and HOMO-LUMO+1 excitations, respectively. These energies account for the difference in orbital energies, as well as the binding energy of the exciton.

The energies of charge transfer states, $\mathrm{CT}_i$ $(i = \overline{3, N})$, are given by:

$$\varepsilon_i = E_i^{\mathrm{A}} - E^{\mathrm{D}} - \frac{e^2}{4\pi\epsilon_0} \int \mathrm{d}\mathbf{r}_1 \mathrm{d}\mathbf{r}_2 \frac{\left|\phi_i^{\mathrm{A}}(\mathbf{r}_1)\right|^2 \left|\phi^{\mathrm{D}}(\mathbf{r}_2)\right|^2}{|\mathbf{r}_1 - \mathbf{r}_2|}, \tag{4.2}$$

where $\phi^{\mathrm{D}}(r)$ and $E^{\mathrm{D}}$ are the HOMO of the donor fragment and its energy, $\phi_{\mathrm{i}}^{\mathrm{A}}(r)$ and $E_{\mathrm{i}}^{\mathrm{A}}$ are the $i^{\mathrm{th}}$ unoccupied orbital of the acceptor fragment and its energy, $\epsilon_0$ is the vacuum permittivity, and the integration is over all space. This expression approximates the donor cation and acceptor anion energies using Koopman's theorem, and the binding energy as the Coulomb attraction between the electron and hole probability densities.

The fragment molecular orbital energies and probability densities in Eq. (4.2) are obtained from Kohn-Sham density functional theory using the Amsterdam Density Functional package (ADF) [100] with the B3LYP hybrid exchange-correlation functional using a double-zeta polarized basis set, DZP. In order to obtain the couplings $J_{ij}$, the fragment orbitals can be used as a basis set in a subsequent DFT calculation on the entire dyad.[101–103] In this basis, the coupling between two fragment orbitals is the generalized charge transfer integral[104]:

$$J_{ij} = \frac{H_{ij}^{\mathrm{KS}} - \frac{1}{2} S_{ij} \left( H_{ii}^{\mathrm{KS}} + H_{jj}^{\mathrm{KS}} \right)}{1 - S_{ij}^2}, \tag{4.3}$$

where $H^{\mathrm{KS}}$ is the dyad Kohn-Sham Hamiltonian and $S$ is the overlap matrix.

Although perturbative Markovian master equations are known to underestimate coherence lifetimes for charge and energy transfer processes [105], they nevertheless do describe the overall rate of population transfer rather well [106]. Therefore, as in an earlier paper that examines exciton and charge transfer dynamics in systems consisting of multiple interacting chromophores,[107] we describe the dynamics of

electron transfer in the dyad after the initial excitation using a Lindblad master equation: [108]

$$\frac{\mathrm{d}\rho}{\mathrm{d}t} = -\frac{i}{\hbar}[\hat{\mathrm{H}}, \rho] + \sum_{k,l} \lambda_{kl} \left( \hat{\mathrm{L}}_{kl} \rho \hat{\mathrm{L}}_{kl}^{\dagger} - \frac{1}{2} \{ \hat{\mathrm{L}}_{kl}^{\dagger} \hat{\mathrm{L}}_{kl}, \rho \} \right), \tag{4.4}$$

where $k$ and $l$ index the system Hamiltonian eigenstates, the Lindblad operators are transfer operators of the form $\hat{\mathrm{L}}_{kl} = |k\rangle \langle l| = \hat{\mathrm{L}}_{lk}^{\dagger}$, $\hat{\mathrm{H}} |k\rangle = E_k |k\rangle$, and the decoherence parameters $\lambda_{kl}$ are defined as

$$\lambda_{kl} = \begin{cases} \frac{\nu f(R_{kl})}{Z}, & E_l > E_k, \\ \frac{\nu f(R_{kl})}{Z} \exp\left( \frac{E_l - E_k}{k_B T} \right), & E_l < E_k, \\ 0, & l = k, \end{cases} \tag{4.5}$$

where

$$f(R_{kl}) = 1 - \frac{1}{2} \left| \sum_{i=1,2} c_{ik}^* c_{ik} - c_{il}^* c_{il} \right| - \frac{1}{2} \left| \sum_{i \geq 3} c_{ik}^* c_{ik} - c_{il}^* c_{il} \right| \tag{4.6}$$

$T = 300$ K, $c_{ik}$ is the $i^{\text{th}}$ probability amplitude for the $k^{\text{th}}$ Hamiltonian eigenstate in the basis that consists of $\mathrm{Exc}_i$, $i = 1, 2$ and $\mathrm{CT}_i$, $i = \overline{3, N}$.

The function $f(R_{kl})$ given by Eq. (4.6) describes the spatial overlap of Hamiltonian eigenstates $|k\rangle$ and $|l\rangle$. Most perturbations of the dyad Hamiltonian that promote charge transfer between its eigenstates are expected to be local. Thus, incoherent charge transfer is more likely to occur between eigenstates with similar charge distributions.[107] The overlap function given by Eq. (4.6) treats any two states with electrons localized on the same molecule as having unity overlap, suppressing direct incoherent transfer between Frenkel exciton states and charge transfer states. The first summation in Eq. (4.6) is over the two Frenkel exciton states, and the second summation is over all the charge transfer states.

The energy dissipation rates in Eq. (4.5) are of Miller-Abrahams form.[109] We have previously fit the parameter $\nu$ in similar rate expressions to reproduce inverse coherence lifetimes for typical chromophoric systems.[107] In this study, we take the more predictive microscopic route of approximating the parameter $\nu$ from an Ehrenfest-TDDFT molecular dynamics simulation, a quantum-classical approach that combines TDDFT with classical Ehrenfest dynamics [4]. These calculations are performed using the *octopus* electronic structure package [110].

The Ehrenfest dynamics simulation begins with the molecule in its ground state equilibrium geometry. A TDDFT calculation is carried out using the Local Density Approximation with the modified Perdew-Zunger exchange correlation functional,

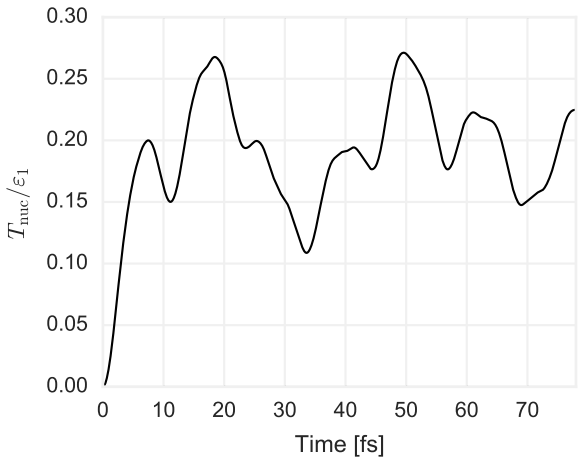


Figure 4.2: The nuclear kinetic energy in units of the initial excitation energy for dyad 2, obtained from Ehrenfest-TDDFT molecular dynamics.

with a grid spacing of 0.16 Å [111]. The enforced time-reversal symmetry algorithm is used to propagate the system with a timestep of 1.2 as. The initial electronic state is prepared by promoting an electron from the HOMO (that is mostly localized on the donor fragment) into the lowest unoccupied molecular orbital that is mostly localized on the same fragment. The resulting state thus approximates the lowest energy Frenkel exciton localized on the donor, with excitation energy $\varepsilon_1$. At the start of the simulation, the total energy of the system is equal to $\varepsilon_1$; it is confined to the electronic degrees of freedom and the nuclei are frozen in place. As the simulation progresses, the excitation energy redistributes between the electronic and nuclear degrees of freedom. The total energy of the system is conserved:

$$T_{\mathrm{nuc}}(t) + E_{\mathrm{KS}}(t) = \varepsilon_1, \tag{4.7}$$

where $T_{\mathrm{nuc}}$ is the nuclear kinetic energy and $E_{\mathrm{KS}}$ is the Kohn-Sham energy, with the initial conditions: $T_{\mathrm{nuc}}(0) = 0$ and $E_{\mathrm{KS}}(0) = \varepsilon_1$. The fraction of the total energy that is in the nuclear subsystem is shown as a function of time in Figure 4.2.

At short times (1-10 fs, the timescale of the fastest vibrations), energy transfer from the electronic to the nuclear subsystem occurs (Figure 4.2). During this time, the increase in the nuclear kinetic energy can be approximated by a linear function:

$$T_{\mathrm{nuc}}(t) \approx \varepsilon_1 \nu t. \tag{4.8}$$

We approximate the characteristic rate $\nu$ of energy dissipation in Eq. (4.5) by the rate of this energy redistribution; $\nu = 0.0267$ fs$^{-1}$, corresponding to a lifetime $\nu^{-1} =$

37.5 fs. The $\nu$ value found in this way is the upper bound for the dissipation rate because it assumes that all energy transferred to the nuclear degrees of freedom is irreversibly lost.

## 4.3 Results and Discussion

The energies of Frenkel exciton states $\mathrm{Exc}_i$, $i = 1, 2$ and charge transfer states $\mathrm{CT}_i$, $i = \overline{3, N}$, as well as the coupling strengths between $\mathrm{Exc}_i$ and $\mathrm{CT}_i$ states for dyads 1 and 2 are shown in Figure 4.3. Because the Frenkel exciton states and the charge transfer states are not eigenstates of the dyad Hamiltonian, the couplings between $\mathrm{Exc}_1$ and $\mathrm{Exc}_2$, and between $\mathrm{CT}_i$ and $\mathrm{CT}_j$, $i \neq j$, are also non-zero. However, these couplings are relatively small and not represented in Figure 4.3.

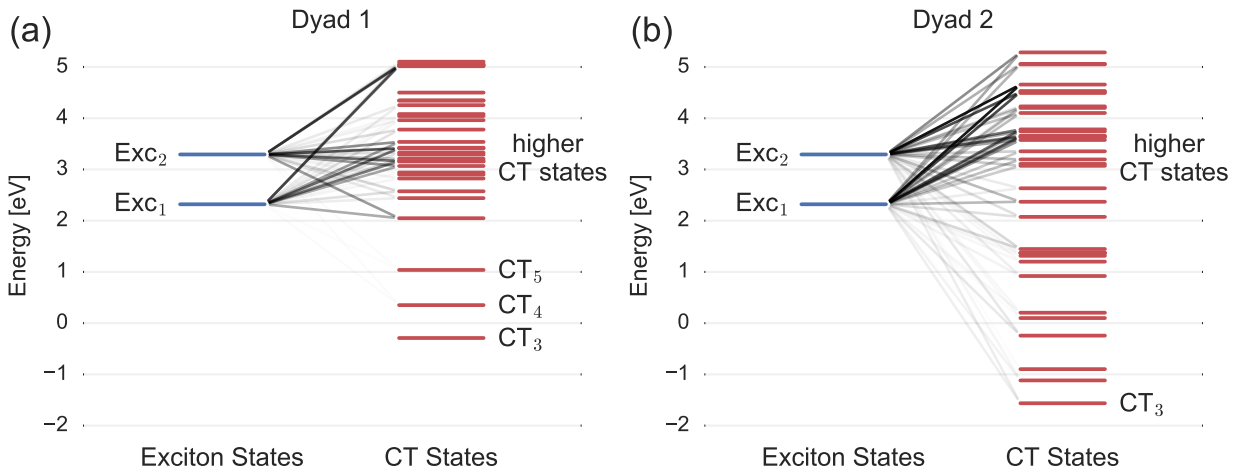


Figure 4.3: Energies of Frenkel excitons localized on the donor fragment (blue lines) and of charge transfer states (red lines). The intensity of the gray/black lines connecting states in these two groups indicates the magnitude of the couplings between the Frenkel exciton and charge transfer states.

Figure 4.3 shows that the states $\mathrm{Exc}_1$ and $\mathrm{Exc}_2$ couple strongly to a select few higher energy charge transfer states. This strong coupling is due to the large orbital overlap between Frenkel exciton and charge transfer states for states with significant electron density on atoms near the interface between the donor and the acceptor fragments. Consequently, Hamiltonian eigenstates contain contributions from both Frenkel exciton and higher-lying charge transfer states. Thus, the electrons in Hamiltonian eigenstates can be significantly delocalized over both the donor and

the acceptor. For eigenstates that have some charge transfer character, the overlap with $CT_3$ given by Eq. (4.6) is non-zero. Thus, these eigenstates can incoherently relax to $CT_3$. Most of their population eventually transfers to $CT_3$ as energy dissipation brings the system to thermal equilibrium. When using our Lindblad quantum master equation, we find that including the higher energy charge transfer states is a prerequisite for observing charge transfer in dyads 1 and 2 on timescales that are consistent with experiments. Indeed, we found that a rather large number of higher energy charge transfer states need to be included before the rate of electron transfer from the donor to the acceptor fragment converges and no longer changes upon inclusion of further states in the Hamiltonian. For dyad 1, convergence was achieved with 20, and for dyad 2 with 28 charge transfer states; all of these states were included for all simulations presented in this chapter.

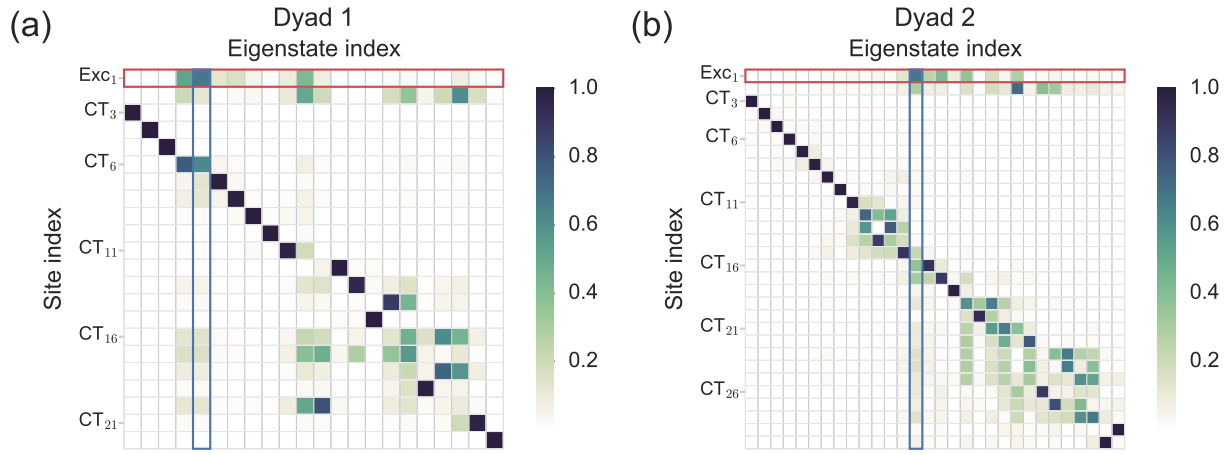


Figure 4.4: The absolute value of the Hamiltonian eigenstate expansion coefficients in the basis that consists of $\mathrm{Exc}_i$, $i = 1, 2$ and $\mathrm{CT}_i$, $i = \overline{3, N}$. Eigenstates are enumerated from left to right, in order of increasing energy. The localized initial state $\mathrm{Exc}_1$ ($\mathrm{IC}_{\mathrm{exc}}$) is shown enclosed by the red box. The eigenstate with the highest contribution of $\mathrm{Exc}_1$ ($\mathrm{IC}_{\mathrm{eig}}$) is enclosed by the blue box.

Figure 4.4 shows the absolute values of the Hamiltonian eigenstate expansion coefficients in the basis that consists of $\mathrm{Exc}_i$, $i = 1, 2$ and $\mathrm{CT}_i$, $i = \overline{3, N}$. For both dyads, it is evident that the lowest energy charge transfer states do not couple strongly to any other states. Therefore, the lowest energy Hamiltonian eigenstates are the localized charge transfer states. If the initial excitation is primarily localized on the donor fragment (in other words, is dominated by the contributions of Frenkel exciton states), then there is virtually no coherent electron transfer to $CT_3$. From

Eqs. (4.5) and (4.6), it follows that there is also little incoherent relaxation of the initial excitation to state $CT_3$. If no charge transfer states beyond $CT_3$ are included in the system Hamiltonian, then no significant electron transfer is observed in our simulations over a timescale of several picoseconds. However, experimental results suggest that charge separation on femtosecond timescales occurs in both dyads 1 and 2.[6]

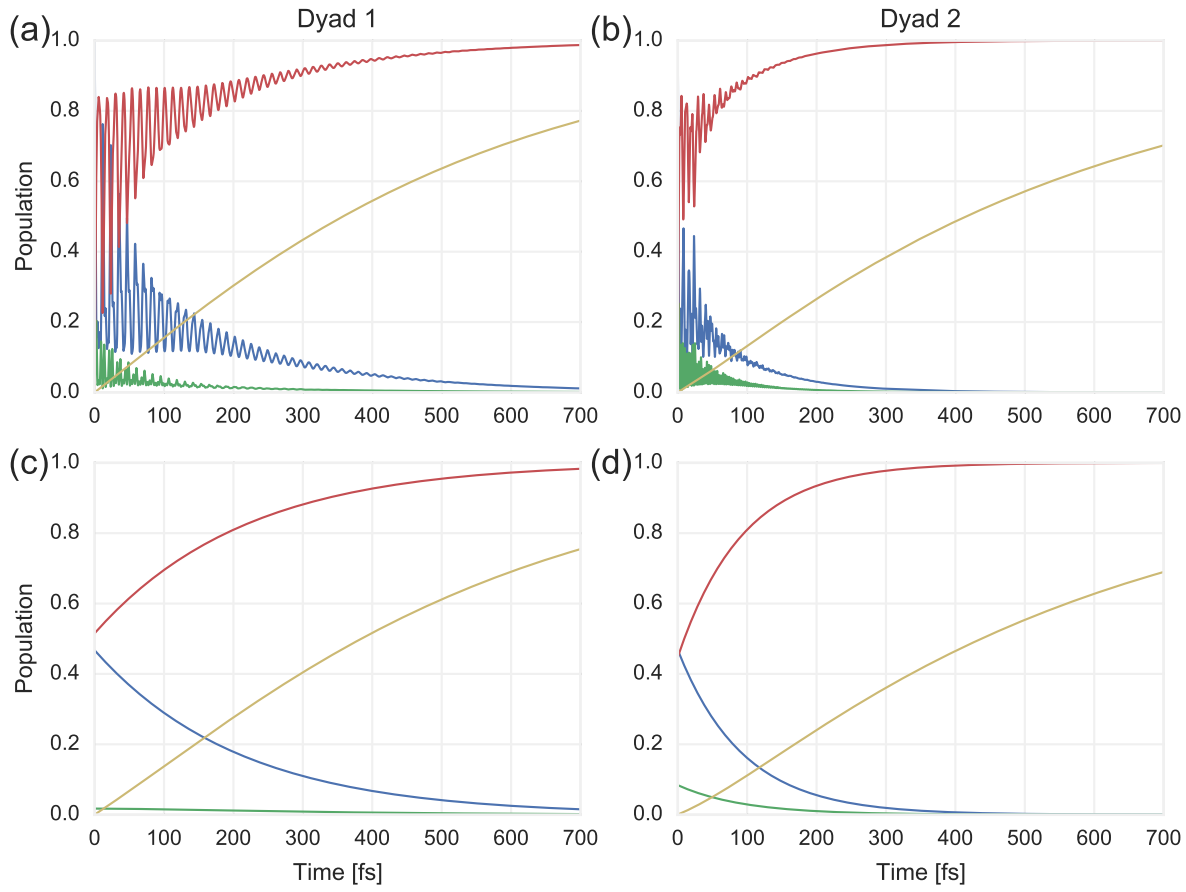


Figure 4.5: Populations of the Frenkel exciton states $Exc_1$ (blue line) and $Exc_2$ (green line), of all charge transfer states (red line), and of the lowest energy charge transfer state (yellow line) for dyad 1 (a,c) and dyad 2 (b,d). Simulations (a,b) are initialized into $IC_{exc}$, and (c,d) into $IC_{eig}$. The calculated charge transfer rates are 215.4 fs (a), 92.1 fs (b), 210.5 fs (c), and 94.1 fs (d).

Figure 4.5 shows the population dynamics in dyads 1 and 2 calculated using our Lindblad model with the full basis of Frenkel exciton and charge transfer states

($N = 22$ states for dyad 1, $N = 30$ states for dyad 2). For each dyad, we simulate dynamics using two different initial conditions: the lowest energy Frenkel exciton localized on the donor fragment, $\mathrm{Exc}_1$, and the eigenstate of the Hamiltonian given by Eq. (4.1) that has the largest contribution of $\mathrm{Exc}_1$. We will refer to these two initial conditions as $\mathrm{IC}_{\mathrm{exc}}$ and $\mathrm{IC}_{\mathrm{eig}}$, respectively. They are shown in Figure 4.4 by the red and blue boxes, respectively.

When the initial state of the dyad is $\mathrm{IC}_{\mathrm{exc}}$ (Figures 4.5a and 4.5b), both coherent and incoherent dynamics clearly play a role in electron transfer. The oscillations indicate that the electron on the donor fragment can coherently transfer to higher-energy excited states on the acceptor fragment, from which it can irreversibly relax to $\mathrm{CT}_3$. In contrast, coherent evolution does not lead to population transfer between the Hamiltonian eigenstates of the dyad. Consequently simulations starting from $\mathrm{IC}_{\mathrm{eig}}$ (Figures 4.5c and 4.5d) do not exhibit coherent oscillations in state populations.[107] In this case, charge separation is driven exclusively by the energy dissipation terms in Eq. (4.4) that bring the populations of the spatially extended Hamiltonian eigenstates into thermal equilibrium. For both choices of the initial condition, we find that the overall charge separation timescales are similar.

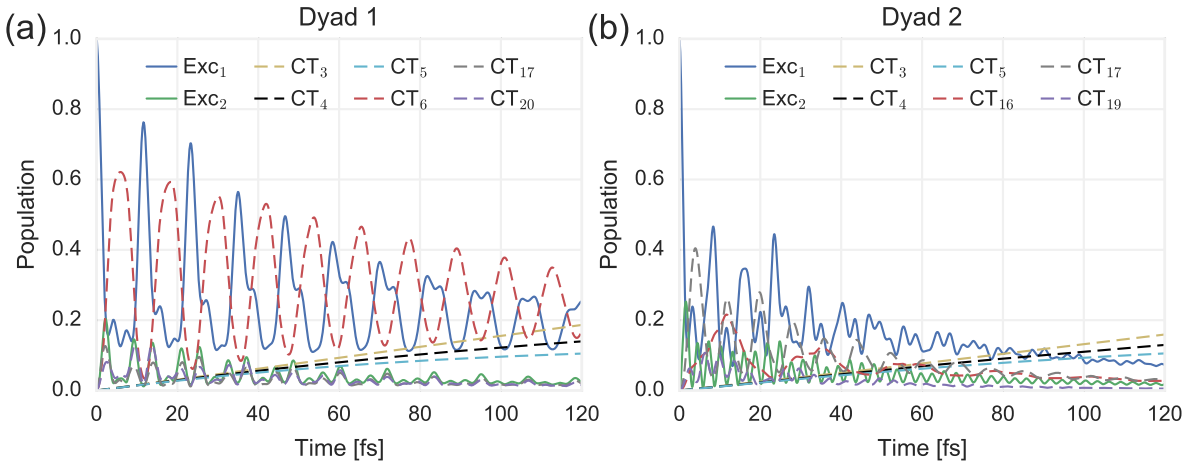


Figure 4.6: The populations of individual Frenkel exciton states (solid lines) and charge transfer states (dashed lines) during the first 120 fs of the simulations shown in Figures 4.5a and 4.5b. Only basis states that acquire significant populations during the charge transfer process are included.

Figure 4.6 shows the time dependence of the populations for basis states that acquire significant populations in the process of charge separation, when both dyads are initialized in $\mathrm{IC}_{\mathrm{exc}}$. For dyad 1, $\mathrm{Exc}_1$ couples most strongly to the charge transfer

state $CT_6$, as seen in Figure 4.3a. In Figure 4.6a, it is evident that the populations of $Exc_1$ and $CT_6$ coherently oscillate in counterphase. The magnitudes of these oscillations decay as energy dissipation redistributes the population from $CT_6$ to the three lower-energy charge transfer states, $CT_3$, $CT_4$, and $CT_5$. At long times, the populations of all states are given by the Boltzmann distribution, with most of the population in the lowest charge transfer state, $CT_3$. There is also a second pathway for charge separation: through the higher-energy Frenkel exciton state, $Exc_2$. Because Frenkel exciton states of the donor are not eigenstates of the dyad Hamiltonian, Eq. (4.1), $Exc_1$ has a non-zero coupling to $Exc_2$. Consequently, some population can transfer coherently to this state, and to higher energy charge transfer states that couple strongly to $Exc_2$. For dyad 1, the states most strongly coupled to $Exc_2$ are $CT_{17}$ and $CT_{20}$. Figure 4.6a shows that these states oscillate in phase with $Exc_2$.

The Frenkel exciton states in dyad 2 couple strongly to multiple charge transfer states, resulting in a less straightforward behavior of the coherent oscillations of state populations (Figure 4.6b).

We have previously shown in [107] that charge separation is sensitive to the relative timescales of coherent and incoherent dynamics that is determined by the energy dissipation parameter $\nu$. Using the value of the energy dissipation parameter $\nu = 0.0267$ fs, estimated from Ehrenfest-TDDFT simulations, the timescale of charge transfer is estimated to be 215 fs for dyad 1 and 95 fs for dyad 2. However, regardless of the value of $\nu$, we find that dyad 2 always exhibits faster charge transfer than dyad 1. This is consistent with the results of transient absorption spectroscopy measurements of Pillai et al. that found the fastest charge separation on a timescale of 600 fs for dyad 1, and on a timescale of 200-500 fs for dyad 2.[6]

The difference in relative charge separation timescales for dyads 1 and 2 can be understood by examining the energy levels and couplings shown in Figure 4.3. The fullerene acceptor in dyad 2 has a denser manifold of charge transfer states at energies similar to or lower than the initial exciton states; the couplings between electronic and charge transfer states also tend to be larger. Consequently, coherent transfer between Frenkel exciton states on the donor fragment and higher-energy charge transfer states that, in turn, incoherently transfer population to $CT_3$ is more efficient in dyad 2 than in dyad 1.

We compare the timescales of charge separation dynamics in dyads 1 and 2 calculated using our model to the timescales estimated by using Fermi's golden rule[7]:

$$\tau_{ij}^{-1} \approx \frac{2\pi}{\hbar}|J_{ij}|^2 \frac{1}{|\varepsilon_j - \varepsilon_i|}. \tag{4.9}$$

Here, $\tau_{ij}^{-1}$ is the rate of charge transfer between the LUMOs of the donor and the

acceptor.

Table 4.1: Charge transfer timescales and associated Hamiltonian parameters using Fermi's golden rule [7] with $i = \mathrm{Exc}_1$ and $j = \mathrm{CT}_3$

| | $\lvert J_{ij}\rvert$ [eV] | $\lvert\varepsilon_j - \varepsilon_i\rvert$ [eV] | $\tau_{ij}$ [ps] |
|---|---|---|---|
| dyad 1 | 0.00048 | 2.61 | 1170 |
| dyad 2 | 0.024 | 3.88 | 0.718 |

Fermi's golden rule is often used to estimate the rate of charge separation, with an implicit assumption that this process occurs directly between the initial excitation and the lowest charge transfer state. Applying Eq. (4.9) with the states $\mathrm{Exc}_1$ and $\mathrm{CT}_3$ results in timescales ($\tau_{ij}$) of 1170 ps and 0.718 ps for dyad 1 and 2, respectively. The timescale for dyad 2 is comparable to experimental results and to the results of simulations using our model. However, the timescale for dyad 1 calculated using Fermi's golden rule is too large by 3 to 4 orders of magnitude, i.e., the golden rule rate is far too slow to account for the charge separation. The difference between the timescales of dyad 1 and dyad 2 can be attributed to the difference in the direct electronic coupling between $\mathrm{Exc}_1$ and $\mathrm{CT}_3$ (Table 4.1). Any other dynamical description that ignores couplings to higher energy unoccupied orbitals on the acceptor will similarly underestimate the charge separation rate.

We also investigate the role of coherence in charge separation dynamics. It is important to recognize that coherence is dependent on the choice of basis. We quantify coherence using the $\mathrm{L}_1$-norm of the off-diagonal terms of the density matrix[112]:

$$C_{L_1}[\rho] = \sum_{k \neq l} |\rho_{kl}|. \tag{4.10}$$

where we take $\rho$ to be in the basis of Hamiltonian eigenstates. In this basis, any individual eigenstate has zero coherence, $C_{L_1}[\rho]$, even if that state is spatially delocalized. Therefore, $C_{L_1}[\rho]$ is a measure of coherence between eigenstates, rather than within an eigenstate. It is independent of charge delocalization within individual eigenstates. Under unitary time evolution, only the phases of $\rho_{kl}$ change and not their magnitudes. Therefore, the $\mathrm{L}_1$-norm coherence does not change under unitary dynamics, and decays monotonically under dissipative dynamics.[112]

Note that if a Hamiltonian eigenstate is a superposition of several Frenkel excitons and/or charge transfer states, then it will have non-zero coherence in the basis that consists of $\mathrm{Exc}_i$, $i = 1, 2$ and $\mathrm{CT}_i$, $i = \overline{3, N}$. However for the remainder of this chapter, we only discuss coherence in the basis of Hamiltonian eigenstates.

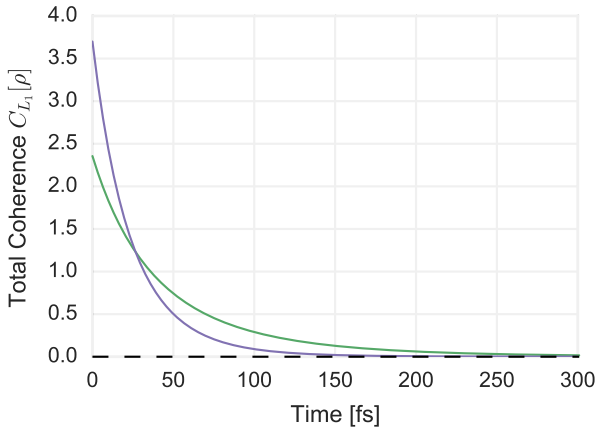


Figure 4.7: Total coherence between Hamiltonian eigenstates, quantified by the $L_1$ norm of the off-diagonal terms of the density matrix in the basis of Hamiltonian eigenstates as a function of time (Eq. (4.10)). The green and purple lines correspond to dynamics initialized in $IC_{exc}$, for dyad 1, and dyad 2, respectively. The dashed black line corresponds to dynamics initialized in $IC_{eig}$, and is zero at all times for both dyads.

Figure 4.7 shows $C_{L_1}[\rho]$ as a function of time. For $IC_{exc}$, initially dyad 2 has more coherence than dyad 1, because more eigenstates contribute to the initial state (compare the red rectangles in Figures 4.4a and 4.4b). However, the coherence also decays faster for dyad 2 than for dyad 1 because irreversible charge separation is more efficient: in other words, dyad 2 exhibits faster transfer to the fully incoherent state $CT_3$. $IC_{eig}$ is an eigenstate, and therefore has no coherence in the basis of Hamiltonian eigenstates. With this initial condition all subsequent dynamics is purely incoherent, as evident from Figures 4.5c and 4.5d.

In both dyads 1 and 2 the rates of charge separation are similar for $IC_{exc}$ and $IC_{eig}$. Thus, it is clear that the amount of coherence in the system does not directly determine the efficiency of charge separation. However, in order for charge separation to occur, the electron in the excited state must be able to reach the acceptor side of the dyad. For $IC_{exc}$, the initial state that is completely localized on the donor, coherence enables the electron to delocalize onto the acceptor. This coherent transfer is more efficient in dyad 2, where the initial Frenkel exciton state is strongly coupled to a large number of charge transfer states. For $IC_{eig}$, the initial state that is already partially delocalized between the donor and the acceptor, charge separation can occur by means of purely incoherent population transfer to lower energy Hamiltonian eigenstates. Therefore, the role that coherence plays in charge separation is largely

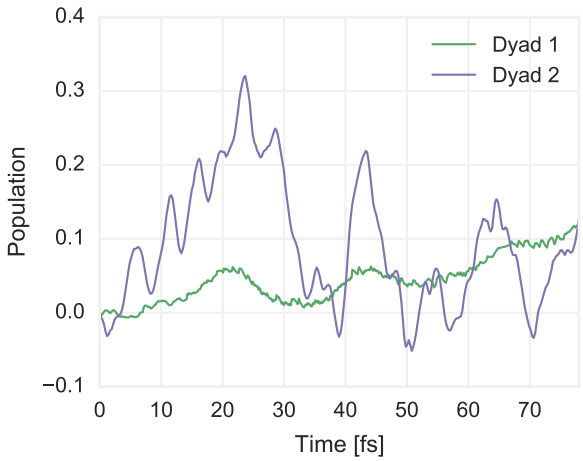


Figure 4.8: The amount of charge transfer as a function of time, quantified using Voronoi analysis on the charge densities found from Ehrenfest-TDDFT, for dyad 1 (green line) and dyad 2 (purple line).

determined by the initial state of the system.

We also estimated charge transfer timescales in dyads 1 and 2 from fully atomistic Ehrenfest-TDDFT simulations. These simulations result in trajectories of the charge density. The redistribution of charge density is quantified using a Voronoi analysis that allows mapping each charge density voxel to a specific atom.[113] The initial state of the Ehrenfest-TDDFT simulations is an excitation into an unoccupied Kohn-Sham orbital that is localized on the donor fragment. This state is similar to state $IC_{eig}$ (the initial condition used in our Lindblad dynamics simulations in Figures 4.5c and 4.5d). Figure 4.8 shows the time-dependence of the total population of all charge transfer states for Ehrenfest-TDDFT dynamics. These simulations are not directly comparable to Lindblad dynamics, because in Ehrenfest-TDDFT simulations energy is never removed from the dyad, and is only transferred between its electronic and nuclear degrees of freedom. In contrast, the Lindblad master equation includes irreversible energy dissipation to an infinitely extensive thermal bath. However, it is evident from Figure 4.8 that charge transfer between the donor and acceptor fragments occurs on a faster timescale for dyad 2 than for dyad 1. This is consistent with both the Lindblad dynamics simulations and transient absorption experiments.[6]

## 4.4 Conclusions

We have simulated the charge separation that follows the optical excitation of typical donor-acceptor dyads using a perturbative Markovian master equation in Lindblad form. The Hamiltonian of the donor-acceptor dyad was constructed using a basis of Frenkel exciton states on the donor and charge transfer states with the electron on the acceptor and the hole on the donor, similarly to Ref.[107]. Hamiltonian parameters were obtained from DFT and TDDFT calculations. The energy dissipation parameters in the Lindblad equation were selected to achieve a thermal distribution of state populations at long times. Additionally, we set the rates of incoherent population transfer between each pair of states to be proportional to the degree of spatial overlap between the states involved. This requirement effectively assumes that most perturbations of the system that cause incoherent repopulation of its electronic states occur locally. The rate of energy dissipation was estimated from Ehrenfest-TDDFT molecular dynamics simulations and found to be of the order of tens of femtoseconds.

Because both the electronic coupling and the spatial overlap between an initial excitation that is primarily localized on the donor and the lowest-energy charge transfer state are negligible, direct transfer between these states contributes little to the overall charge separation dynamics. Irreversible charge separation is a process that involves both coherent and incoherent electron transfer. Within the framework of our model, if population is initially excited into the Frenkel exciton state localized on the donor, it can coherently transfer to higher energy charge transfer states. Concurrently, relaxation from higher to lower-energy charge transfer states occurs. However, for population initially excited into a Hamiltonian eigenstate that is already partially delocalized onto the acceptor, coherent transfer between this and other Hamiltonian eigenstates is not required to achieve charge separation. We found that the rate of charge separation is similar for both initial conditions, implying that the extent of spatial delocalization of the Hamiltonian eigenstates rather than the amount of coherence between eigenstates primarily determines the efficiency of charge separation Thus, the importance of coherence in the Hamiltonian eigenstates for efficient charge separation depends on the initial state of the system. Note that spatial delocalization of eigenstates will give rise to coherence in any non-eigenstate basis, such as the basis consisting of $\mathrm{Exc}_i$, $i = 1, 2$ and $\mathrm{CT}_i$, $i = \overline{3, N}$.

We have shown that for typical donor-acceptor dyads a large number of charge transfer states (20 for dyad 1 and 28 for dyad 2) affect the rate of charge separation. Since the higher lying states facilitate charge separation, approximations that neglect these states will tend to underestimate the rate, sometimes by several orders of magnitude. All of these states must be included in the simulation of charge separation

dynamics to obtain reasonable agreement with both atomistic Ehrenfest-TDDFT molecular dynamics simulations and charge separation rates obtained from transient absorption experiments.[6]

In agreement with the experimental results of Pillai et al. [6], in our simulations the dyad with a fullerene-based electron acceptor shows higher charge separation rates than the dyad with a porphyrin-based acceptor. We attribute this to the former acceptor having a larger number of charge transfer states that are close in energy and are strongly coupled to the lowest two Frenkel exciton states localized on the donor.

The theoretical analysis presented in this chapter reveals key design criteria that enable rational selection of donor acceptor pairs for the synthesis of molecular dyads that exhibit ultrafast charge separation. First, the donor and acceptor constituents of the dyad should be chosen to ensure a dense manifold of charge transfer states at energies close to that of the donor Frenkel exciton. Second, the constituents should be chosen to ensure strong coupling between the donor Frenkel exciton state and the higher-lying charge transfer states, allowing some extent of delocalization of the Hamiltonian eigenstate over both the donor and the acceptor.

# Chapter 5

# Simulations of a prototypical synthetic light harvesting system

## 5.1 Introduction

Light harvesting antennae of photosynthetic organisms are exquisitely organized biomolecular structures [114, 115]. Although nearly every photosynthetic species on the planet has evolved a light harvesting antenna that is customized to its environment, all these antennae are actually composed of relatively few types of pigment molecules, e.g., chlorophylls, bacteriochlorophylls, carotenoids, phycobiliproteins. Two additional factors beyond the choice of pigment are critical in the customization of the antennae to very different environments. These are the tailored structural organization of the pigments, and the tuning of pigment spectral properties by their in-vivo protein environment. In essence, all LHCs are composed of densely packed pigments that are usually encased in structure-preserving proteins and bound to membranes. The dense packing of pigments leads to strong electronic coupling between chromophores. Some LHCs also have a high degree of organization that aligns neighboring dipoles to further enhance electronic coupling. An example of this is the LH2 system found in purple bacteria, which consists of pigment-protein complexes in which the proteins form helical subunits enclosing rings of 18 and 9 pigments [116]. This strong coupling, along with screening from solvent effects afforded by the binding to photosynthetic membranes, is believed to be the structural basis for the long-lived quantum coherent effects recently observed in a number of light harvesting complexes [2].

Quantum mechanics also plays an important role in the performance of LHCs as antennae for light, both in determining their effective absorption cross-section

and the excitation energy transfer subsequent to photon absorption. As mentioned above, the quantum mechanical coupling of several pigments can alter the oscillator strength of electronic transitions in pigment-protein complexes. It is believed that this is used to advantage to increase the efficiency of light absorption in several LHCs. The most striking example of this comes from green sulfur bacterium, a primitive photosynthetic organism that lives in extremely low light conditions and possesses a highly effective antenna structure, the chlorosome, that has recently been identified as large concentric nanotubes of tightly packed bacteriochlorophyll molecules [117]. This particular structure leads to very strong inter-pigment coupling and greatly enhanced electronic transition oscillator strengths for efficient light capture and energy transfer. Much of the drive for construction of artificial light harvesting complexes is to design and construct synthetic molecular complexes that mimic these features of the chlorosome.

The key to producing synthetic mimics of natural light harvesting systems is the establishment of the necessary distance relationships between multiple chromophores. Although this could, in principle, be achieved using elaborately designed synthetic molecules, this approach is typically quite laborious, is difficult to scale, and leads to highly aromatic systems with poor solubility and limited processing possibilities. A number of studies have instead used polymers and dendrimers as scaffold materials that establish an upper limit to the distance between chromophores [118, 119], but these systems generally lack the rigidity needed to control transition dipole orientation and to prevent excimer-based quenching pathways. As an alternative, several groups have developed ways to self-assembly of the chromophores themselves, generating large bundles of porphyrins that show energy transfer behavior [120, 121]. While these provide interesting chlorosome mimics, it is quite difficult to optimize the performance of these systems to meet specific applications, since the use of new chromophores with different optical properties can lead to unpredictable assembly outcomes. As an alternative, one can employ self-assembling protein coats of viruses as rigid scaffolds that can template the formation of synthetic light harvesting systems [27]. In particular, architectures based on the capsid protein monomer of the tobacco mosaic virus (TMV), can be conveniently produced and employed for the assembly of chromophore arrays by introducing cysteine residues at specific positions that allow the covalent attachment of a wide variety of commercially-available chromophores with varied optical characteristics. One particularly interesting aspect of rod-like light harvesting arrays is the fact that they are inherently three-dimensional, and thus could possess redundant energy transfer pathways that could circumvent defect sites better than linear or ring-like systems. An additional advantage of the synthetic system is that the electronic properties of the aggregate complex can be chemically controlled by changing the type of chromophore, the type of linker used to

covalently attach the chromophore to the protein, and the position where it attaches to the protein.

In this work we investigate features of the quantum design of synthetic pigment-protein structures for light harvesting that are based on TMV-templated chromophore assemblies. The close proximity of the chromophores in the TMV assemblies suggests that their excited electronic states will be closely coupled. To motivate the design and synthesis of new systems with enhanced electronic coupling, we analyze here several potential synthetic structures using theoretical modeling and spectroscopic characterization. We employ molecular mechanics simulations of the chromophore-protein systems to provide insight about the geometry and disorder. This is important given that these are systems for which crystal structures are hard to obtain, and thus direct experimental information about the geometry is lacking. A key focus of the present study is to understand both the geometry and the mobility of the chromophores, and the extent to which these factors are determined by microscopic details of the surface of the protein, which typically forces the chromophores to fit into a solvent-accessible pocket. Different chromophores will be oriented differently and can have varying degrees of mobility depending on their point of linkage and the nature of the link to the protein. Such geometric and mobility information provides a systematic way to compare and screen for optimal chromophore-protein candidates for synthesis of artificial light-harvesting complexes. The geometry of the chromophores is also critical to understanding the optical properties of these aggregate systems, since the electronic coupling between chromophores is primarily determined by the relative orientations of their transition dipole moments (TDMs) [5]. In the present work, the geometries of the conformers found from the molecular mechanics simulations are used in a tight-binding model to simulate the optical properties of the system, with comparison to experimental spectra.

The remainder of the chapter is constructed as follows. Section 5.2 describes the TMV and chromophore structures employed here and summarizes the computational methods used for the molecular mechanics structural studies with ground state chromophores, as well as the ab initio calculations for electronically excited chromophores and construction of the tight-binding model for simulation of the optical spectra. Section 5.3 presents the structural results with analysis of geometry, orientation and ordering of the chromophores, followed by analysis of the linear absorption spectra. Section 5.4 concludes with an assessment of the implications for quantum informed molecular design of artificial light harvesting systems.

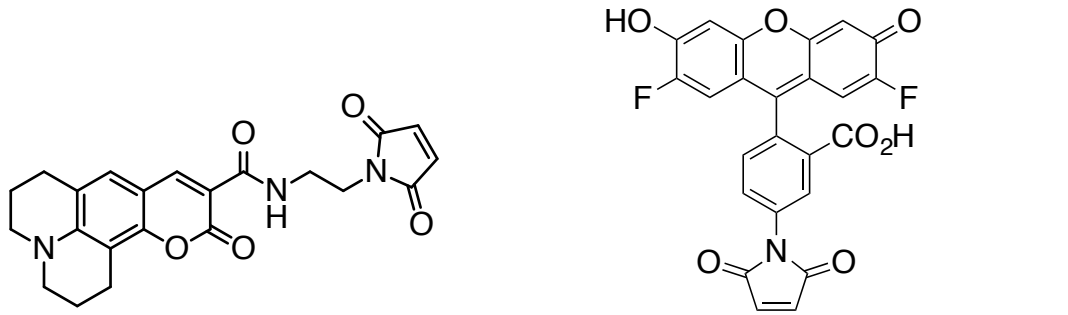


(a) Coumarin 343 + Ethyl-Maledimide (b) Oregon Green 488

Figure 5.1: Molecular structures of modified Coumarin 343 (i.e. Coumarin 343 with a linker molecule, ethyl-maledimide) and Oregon Green 488.

## 5.2 Computational Details

### 5.2.1 The TMV Protein and Chromophores

The chromophore-protein complexes studied in this work have all been experimentally synthesized. Two of us (D.T.F. and M.B.F.) have successfully attached chromophores to the TMV protein and the theoretical study of this complex is the focus of this chapter. The details of the self-assembly of TMV are available in ref. [27] and the details of attaching chromophores to the TMV protein are presented in ref. [122] .

The TMV systems are self-assembled into a double-disk with 17-fold radial symmetry. We have then studied the chromophores, Coumarin 343 and Oregon Green 488 (OG), which are attached to the TMV protein at either the 104 (inner ring) or 123 (outer ring) residue positions. OG can be attached directly to the residues without modification while Coumarin 343 requires a linker molecule. Coumarin 343 has been attached to both the 104 and 123 positions with a linker, ethyl-maledimide. We refer this complex of Coumarin 343 and the linker molecule as CE. The molecular structures of CE and OG are available in Figure 5.1. The 104 and 123 positions differ in the distance from the center of the disk, thereby controlling the distance between neighboring chromophores as illustrated in Figure 5.2. These systems will henceforth be referred to as CE-104, CE-123, OG-104, and OG-123.

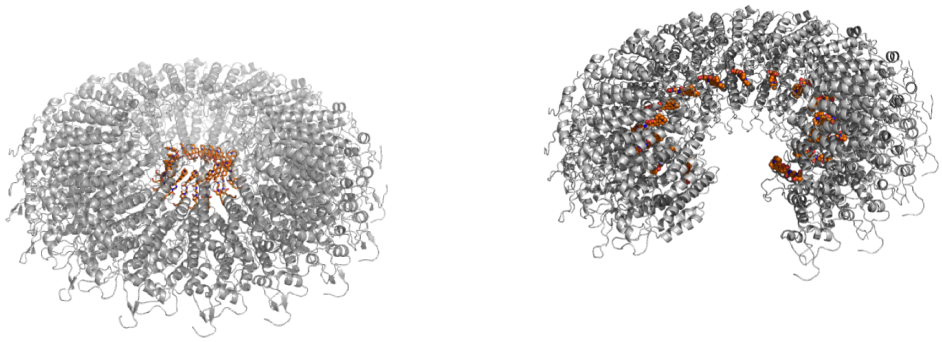

(a) 104 position (b) 123 position

Figure 5.2: TMV-chromophore double-disk system. Protein colored grey, and chromophore colored orange. (a) Chromophore attached at the 104-residue position (inner ring) (b) Chromophore attached at the 123-residue position (outer ring)

### 5.2.2 Conformational search using Monte Carlo Multiple Minimum

This TMV-chromophore system is rather complex and nearly impossible to treat fully quantum-mechanically. Therefore, we tried to explore the complex configurational space of the system using the Monte Carlo Multiple Minimum (MCMM) algorithm with the force field of OPLS2005 [123]. All molecular mechanics simulations presented here were run with the Schrodinger's MacroModel software suite.[124] The double disk system has 34 monomers arranged with 17 monomers per layer, which includes roughly 200 rotatable bonds. For the simulations presented before, we focus on only one layer. An MC search over the full parameter space is computationally intractable as the required time scales exponentially with the number of rotatable bonds.

In the simulations of all but CE-104, we considered five monomers on each layer in the TMV due to limited computational resources under the assumption that chromophores that are separated by two monomers are non-interacting. We took only the middle three on the top layer for later analyses. We validated this assumption by comparing CE-104 simulations that included the full 17 ring monomer and found that the the average parameters (position and orientation) do not change significantly by

using the truncated system.

During the conformational search, the chromophore and linkers were freely movable atoms. In order to reduce the parameter space further in a 5-monomer subset, all atoms within 14 residues of the chromophore are constrained to their initial position using a harmonic potential with a force constant of 200 kJ $mol^{-1}Å^{-2}$, and all atoms between 15 and 29 residues are frozen in place. All other atoms were ignored as they are too far away for any significant interaction with the free atoms. The resulting conformations are collected and minimized using the Polak-Ribiere Conjugate Gradient (PRCG) method [125].

### 5.2.3 Ab-initio calculations of excited states

For the spectral simulations shown later, we needed transition dipole moments (TDMs) and this was achieved by performing time-dependent density functional theory (TDDFT) with B3LYP[126]/6-31G(d)[127, 128]. We truncated the linker molecule of CE and replaced the linker with a methyl group for simplicity. TDDFT calculations employed 75 radial grid points and 302 Lebedev angular grid points. We also employed equation-of-motion coupled-cluster singles and doubles (EOM-CCSD) to further verify excitation energies and TDMs within the same basis set. These calculations were run with the development version of Q-Chem. [129]

| | | B3LYP | EOM-CCSD |
|---|---|---|---|
| first excitation energy (eV) | | 3.4742 | 3.7753 |
| transition dipole (au)* | x | 2.6354 | 2.7087 |
| | y | 0.0057 | 0.1280 |
| | z | 0.0060 | -0.0231 |
| oscillator strength | | 0.5912 | 0.7609 |

Table 5.1: Electronic structure results for Coumarin-343. The ground-state and excitation energies, transition dipoles, and oscillator strengths are given for TDDFT-B3LYP, and EOM-CCSD. *EOM-CCSD transition dipole is for the ground state → excited state transition.

EOM-CCSD and TDDFT both yield similar wavefunctions in terms of dominant configurations, excitation energies, and TDMs as shown in Table 5.1. As the first excited states in both systems are of singly-excited open-shell singlet character, the excitation energies from them are expected to be very accurate. The largest source of error is likely the limited size of basis set employed here, but in chapter 3 it was shown that employing a larger basis such as 6-311G* does not significantly affect the excitation energies (i.e. change is 0.5 eV for EOM-CCSD and 0.1 eV for TDDFT).

For the spectral simulation, we used the TDDFT TDMs due to the following reasons. First, TDDFT calculation is expected to be closer to its complete basis set (CBS) limit as EOM-CCSD calculation is more sensitive to increasing the basis set size. Second, it was pointed by Koch et al. that EOM-CC does not yield size-intensive TDMs, and thus EOM-CC may become a less reliable way to obtain TDMs for large systems [130]. For these reasons, the analyses requiring TDMs were carried out based on TDDFT.

### 5.2.4 Spectral Simulations

#### Hamiltonian Parametrization

A tight-binding Hamiltonian of the chromophores using the Frenkel Exciton model is often used to describe the electronic and optical properties of chromophore-protein systems[14, 29] and we have employed a similar model as well:

$$\hat{\mathrm{H}} = \sum_{i=1}^{N} \varepsilon_i \hat{\mathrm{a}}_i^{\dagger} \hat{\mathrm{a}}_i + \sum_{i=1}^{N} \sum_{j=1}^{N} J_{ij} \hat{\mathrm{a}}_i^{\dagger} \hat{\mathrm{a}}_j \tag{5.1}$$

where $\epsilon_i$ is the on-site energy and $J_{ij}$ is the coupling parameter between the site $i$ and the site $j$. The coupling $J_{ij}$ is a function of the positions of chromophores $i$ and $j$, and the relative orientations of each of their transition dipole moments. This is the same model as described in 3.1. The close proximity between some of the chromophores in our system means that we cannot expect that the commonly used ideal dipole-dipole approximation (IDA) for $J_{ij}$ couplings to hold.

We define $\Delta E_n^{\mathrm{dimer}}$ to be the $n^{\mathrm{th}}$ electronic excitation energy of the dimer and $\Delta E_n^{\mathrm{monomer}}$ to be the $n^{\mathrm{th}}$ electronic excitation energy of the monomer. In the case of a well-separated dimer, both $\Delta E_1^{\mathrm{dimer}}$ and $\Delta E_2^{\mathrm{dimer}}$ approach to $\Delta E_1^{\mathrm{monomer}}$ and therefore the average of $\Delta E_1^{\mathrm{dimer}}$ and $\Delta E_2^{\mathrm{dimer}}$ is identical to $\Delta E_1^{\mathrm{monomer}}$. However, our previous work shows that at close distances ($< 12$ Å), the average will begin to deviate from the monomer excitation energy ($\Delta E_1^{\mathrm{monomer}}$). The extent of the deviation will depend on the distance and relative orientations of the two interacting chromophores [131].

In order to account for the geometry-dependent effect, we obtain more accurate Hamiltonian parameters based on pairwise TDDFT calculations, which are defined as follows:

$$\varepsilon_i = \Delta E_1^{\mathrm{monomer}} + \sum_{i \neq j} V^{\mathrm{TDDFT}}(\vec{R}_i, \vec{\mu}_i, \vec{R}_j, \vec{\mu}_j) \tag{5.2}$$

$$V^{\mathrm{TDDFT}}(\vec{R}_i, \vec{\mu}_i, \vec{R}_j, \vec{\mu}_j) = \frac{\Delta E_2^{\mathrm{dimer}} + \Delta E_1^{\mathrm{dimer}}}{2} - \Delta E_1^{\mathrm{monomer}} \tag{5.3}$$

$$J_{ij} = J^{\mathrm{TDDFT}}(\vec{R}_i, \vec{\mu}_i, \vec{R}_j, \vec{\mu}_j) = \frac{E_2^{\mathrm{dimer}} - E_1^{\mathrm{dimer}}}{2} \tag{5.4}$$

where $\vec{R}_i$ denotes the position of the $i^{\mathrm{th}}$ chromophore and $\vec{\mu}_i$ denotes the orientation of the $i^{\mathrm{th}}$ chromophore.

Among all of our molecular mechanics configurations, there are about $10^7$ pairwise interactions. Running a TDDFT calculation for each pairwise interaction in every configuration instance is computationally intractable and also redundant since many of the pairs will have similar geometries. Our approach is to run a TDDFT calculation at selected distances and orientations and interpolate to predict ab-initio values for other geometries. The precise procedure is as follows:

1. We parametrize the relative orientation of two interacting monomers: $r, \theta_A, \theta_B, \phi_B$ as defined in 3.3b.

2. We then discretize the space along those variables and calculate the TDDFT energies at the geometries defined by the following grid points: r = [5 Å, 5.25 Å, 5.75 Å, 6 Å, 6.25 Å, 6.5 Å, 6.75 Å, 7 Å, 7.5 Å, 8 Å, 8.5 Å, 9 Å, 10 Å, 12 Å, 14 Å], $\theta_A$ = [-90°, 90°] with a 15° increment, $\theta_B$ = [0°, 180°] with a 15° increment, and $\phi_B$= [0, 180] with 30° increment. Out of the possible 18928 geometries, we discard the points that yield unphysical geometries, which result in a training set of 4456 energies.

3. We employ a model function (see below) with three free parameters each for $J_{ij}$ and $V_{ij}$, and fit these parameters by using linear regression to match $J^{\mathrm{TDDFT}}$ and $V^{\mathrm{TDDFT}}$, respectively, at each of the grid points.

The model functions used to describe $V$ and $J$ are

$$J_{ij}^{\mathrm{model}}(r, \theta_i, \theta_j, \phi_j) = C_J(r) J_{ij}^{\mathrm{IDA}}(r, \theta_i, \theta_j, \phi_j) \tag{5.5}$$

$$V_{ij}^{\mathrm{model}}(r, \theta_i, \theta_j, \phi_j) = C_V(r) V_{ij}^{\mathrm{IDA}}(r, \theta_i, \theta_j, \phi_j) \tag{5.6}$$

$$C_k(r) = \frac{c_1^k}{(c_2^k - \exp(r/c_3^k))} \tag{5.7}$$

where $J_{ij}^{IDA}$ and $V_{ij}^{IDA}$ are the couplings obtained from IDA, and $C_k$ is a logistic function, with three free parameters. If $C_J$ and $C_V$ deviate significantly from 1, then that is precisely when IDA breaks down. The fitted parameters are found to be: $c_1^V = 0.10388804$, $c_2^V = 0.21424357$, $c_3^V = 2.2014798$ $c_1^J = 0.2889955$, $c_2^J = 1.50871422$, $c_3^J = 3.14407206$.

**Linear Absorption Spectra**

In order to simulate the linear absorbance of the full double disk TMV system, we first sample small slices (i.e. 5 monomers) from the MCMM configurations and concatenate the middle three chromophores to generate the full system. Since 17 is a prime number, we need to take 5 samples of three chromophores, and 1 sample of two chromophores, all of which are sampled randomly. This is repeated for both the upper and lower disks. For each geometry sample, we extract the center of mass positions and the transition dipole moments ($R$ and $\mu$) of each chromophore. Next, the tight binding Hamiltonian in Eq. (5.1) is constructed using the parameters $\varepsilon_i$ and $J_{ij}$ described in Eq. (5.5). The Hamiltonian is diagonalized to yield exciton states and energies:

$$\hat{H}|\psi_k\rangle = E_k|\psi_k\rangle \tag{5.8}$$

$$|\psi_k\rangle = \sum_i^N c_{ik}|\phi_i\rangle. \tag{5.9}$$

The linear absorption spectra for a given Hamiltonian is calculated using

$$\vec{\mu}_k = \sum_i^N c_{ik}\vec{\mu}_i \tag{5.10}$$

$$\mathrm{Abs}(E) \propto \sum_k^N \|\vec{\mu}_k\|^2 \exp\left[-\frac{(E-E_k)^2}{2\sigma^2}\right]. \tag{5.11}$$

where $\vec{\mu}_k$ is the $k^{\text{th}}$ exciton's transition dipole moment, and is defined as a linear combination over the molecular transition dipole moments [7]. The summation in Eq. 5.11 describes a discrete convolution between a gaussian function, and the Hamiltonian's eigenvalue stick spectrum, weighted by the 2-norm squared of the exciton transition dipole moment. The variance of the gaussian function ($\sigma$) is the line broadening parameter for our simulated linear absorption spectrum. In the limit where $\sigma \to 0$, we obtain the eigenvalue stick spectrum. Eq. 5.11 yields the spectra for a single geometry instance. This process is repeated 5000 times (large enough to obtain converged spectra) to average over the different possible geometry configurations, then normalized by the maximum absorbance.

## 5.3 Results and Discussion

### 5.3.1 Geometric Distributions of Chromophores

We analyze the MCMM conformations based on the center of mass (CM) positions of the chromophores and the orientations of TDMs of the chromophores. Those two collective variables are particularly useful in understanding the geometric distribution as we shall see below.

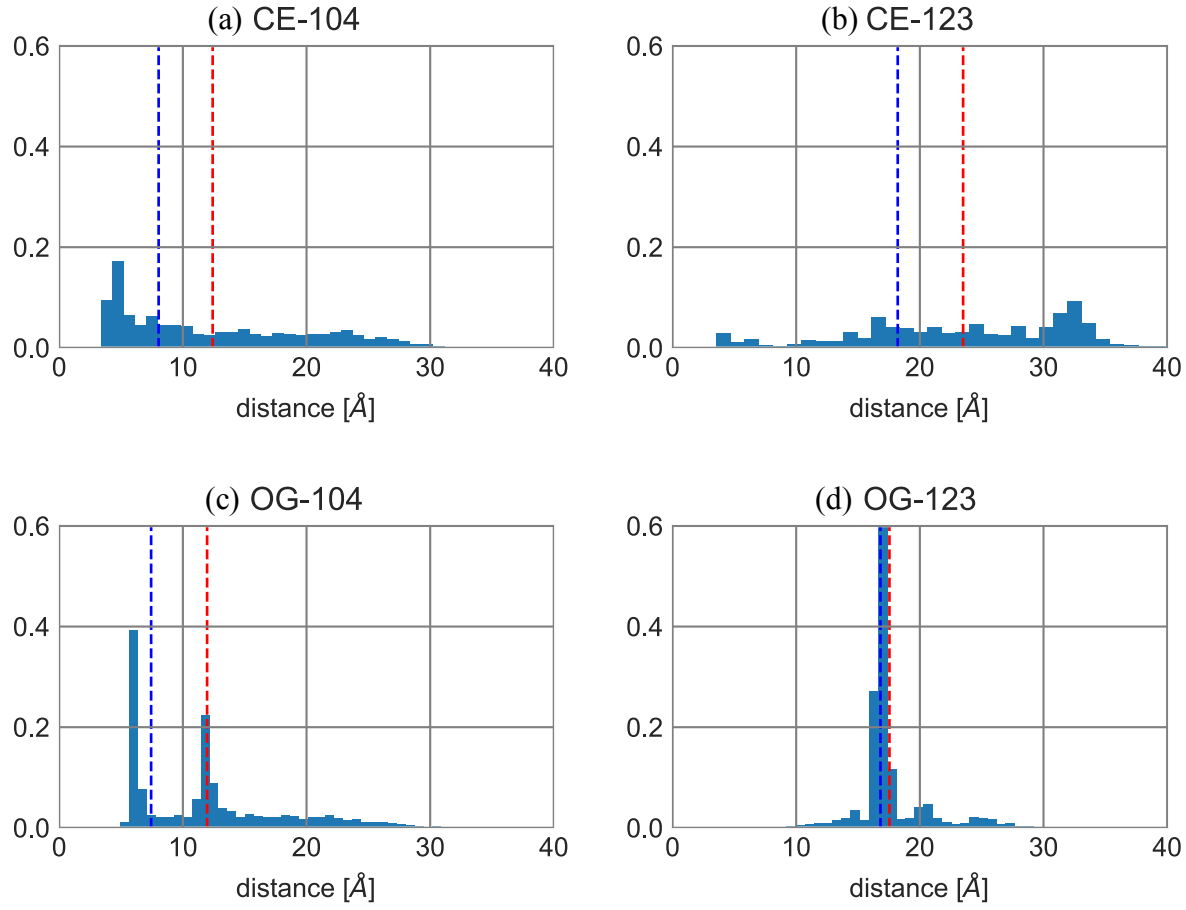


Figure 5.3: Normalized histograms of the center-of-mass distances between nearest-neighboring chromophores in (a) CE-104, (b) CE-123, (c) OG-104, and (d) OG-123. The blue dotted line indicates the "ideal" nearest-neighbor distance, and the red dotted line indicates the mean distance, which are defined in the main text. The number of samples used in each histogram is 3607, 5499, 5918, and 5810, respectively.

Figure 5.3 shows a histogram of distances between the CM positions of nearest-neighboring chromophores. We first note that both CE-104 and CE-123 exhibit significant multimodal behaviors while bimodal and monomodal behaviors are observed for OG-104 and OG-123, respectively. The qualitative difference between CE and OG can be explained simply: the linker molecule in CE allows Coumarin to move easily its CM position whereas OG has no linker molecule in our study. We further computed the "ideal" nearest-neighbor distance, $r_{\text{ideal}}$, which assumes an equilateral 17-polygon, and the mean of nearest-neighbor distances, $\bar{r}$. Those two values are not meaningful in the case of highly multimodal histograms as in the CE cases. In the case of OG-123, two values are almost identical whereas each of two peaks in OG-104 roughly corresponds to $r_{\text{ideal}}$ and $\bar{r}$.

The significance of Figure 5.3 is that some chromophores (in particular CE-104 and OG-104) in the TMV systems are not far enough; the distance between nearest neighbors is often less than 12 Å. Based on our previous study of Coumarin 343 in chapter 3, when two chromophores are closer than 12 Å, it is likely that the usual dipole approximation to the Hamiltonian starts to fail quite catastrophically. This was indeed our motivation to go beyond the dipole approximation, and this will be discussed further later in this chapter. We note that in the previous study, Coumarin was considered without a linker molecule. However, we expect the failure of dipole approximations to behave similarly. We also expect qualitatively the same conclusion for OG.

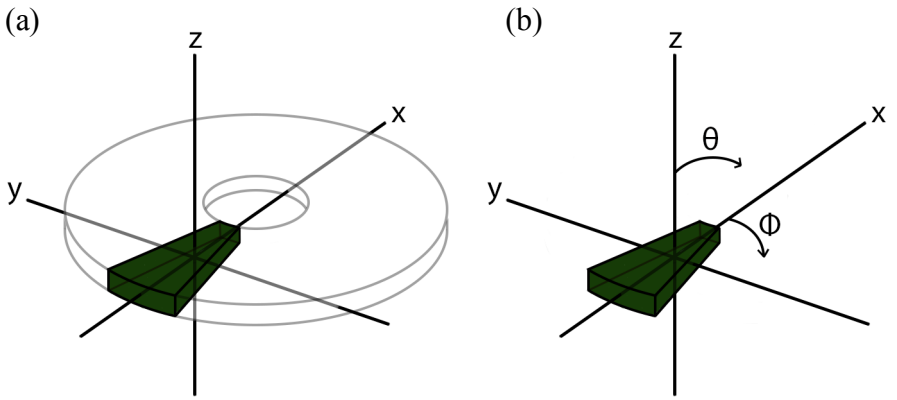


Figure 5.4: (a) Schematic description of the monomer frame embedded into the entire TMV represented by a disk. The monomer is represented by the wedge. (b) Schematic description that represents the polar angle $\theta$ and the Azimuthal angle $\phi$ in the monomer frame.

For the purpose of analysis, we introduce the monomer frame illustrated in Figure 5.4. We define the monomer frame as follows: for every chromophore, the x-axis points towards the center of TMV disk, the z-axis is parallel to the axis of rotational symmetry, and the y-axis is defined in the conventional way for given those x- and z-axes (i.e. $\hat{y} = \hat{z} \times \hat{x}$). The radial axis of the polar plot ranges from 0° to 180°, and corresponds to the polar angle of the monomer frame. The angular axis of the polar plot ranges from 0° to 360°, and corresponds to the azimuthal angle of the monomer frame.

Figure 5.5 shows a histogram of the orientation of TDMs measured in the monomer frame. It shows that the CE systems are more spread than are those in the OG systems. In other words, OG systems are far more confined than CEs. This does not necessarily mean that OG systems are more ordered and the quantification of order-disorder will be discussed later in the chapter. The wider distribution in the CE systems can be understood by considering the effect of the presence of a linker molecule. We see similar trends in both chromophores when attached to the 104 or 123 position. The 104 position exhibits a wider vertical spread compared to the 123 position whereas the 123 position shows a wider horizontal spread compared to the 104 one. The broad distribution of the CE systems is somewhat surprising given that the chromophore molecules are surrounded by the TMV protein environment. The linker molecule gives enough flexibility to the Coumarin chromophore which results into a broad geometric distribution. This is one of the reasons that make atomistic simulations of the system intractable.

### 5.3.2 Order, Disorder, and Correlation Among Chromophores

We discuss one-body and two-body observables of this system to further quantify the order and disorder present in the system. There is a simple analogy between our system and one-dimensional classical Heisenberg model of 17 sites with periodic boundary conditions. In other words, a TMV disk can be reduced down to a lattice with 17 sites and the chromophore of each monomer can be considered a classical spin on each site. This analogy allows us to utilize one-body and two-body measures that are widely used to quantify order in spin systems. In passing we note that all the orientation vectors of TDMs used in the following analyses are all normalized and measured in the monomer frame. As we analyze only five monomers per sample, the periodic boundary condition was not applied throughout the analysis.

The one-body measure considered here is the average of the magnetization of

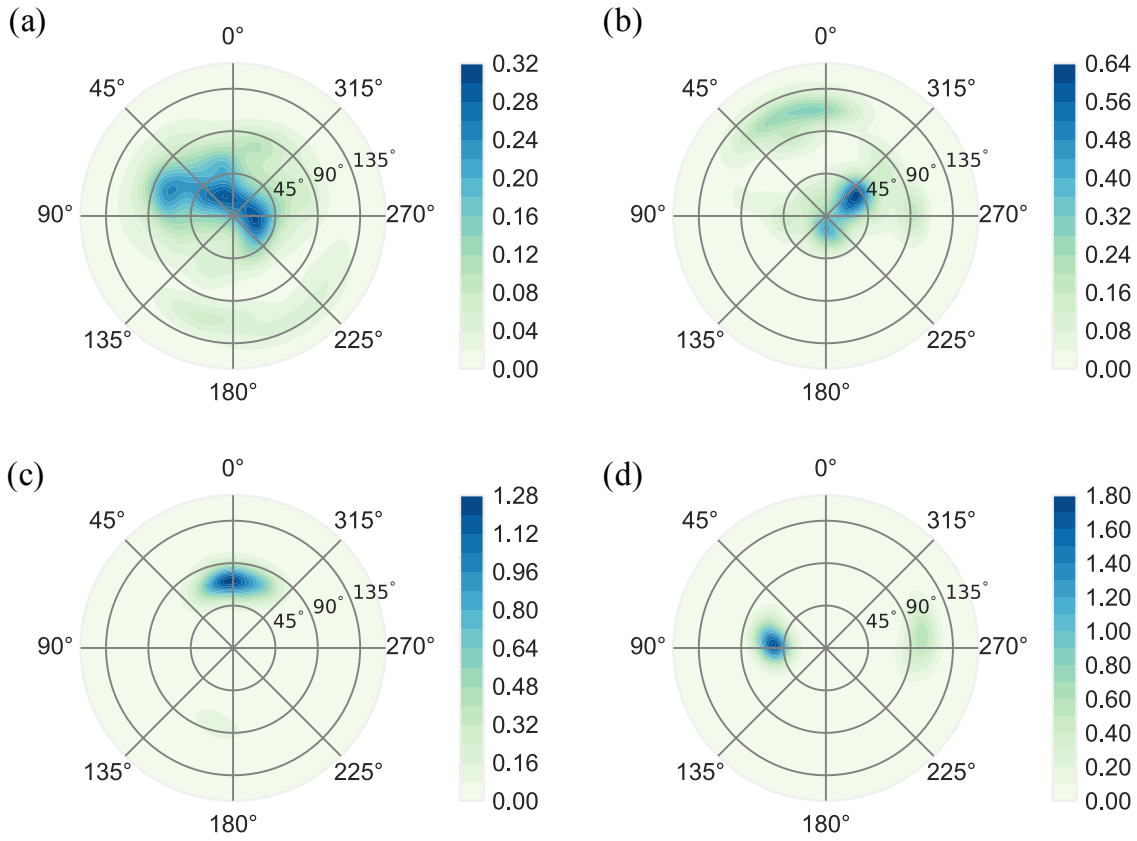


Figure 5.5: Normalized distributions of the transition dipole moments orientation for (a) CE-104, (b) CE-123, (c) OG-104, and (d) OG-123. The radial distance indicates $\theta$ and the angular orientation indicates $\phi$. $\theta$ and $\phi$ are defined in Figure 5.4. We fitted the TDM vectors to a bivariate gaussian kernel density estimator with a 0.2 bandwidth to obtain this figure.

spins, which in our case is the average of the orientation vector of TDMs, defined as

$$\langle \vec{\mu} \rangle = \frac{1}{N_{\text{samples}} N_{\text{spins}}} \sum_{i}^{N_{\text{samples}}} \sum_{\alpha}^{N_{\text{spins}}} \vec{\mu}_{\alpha}(i). \tag{5.12}$$

$\langle \vec{\mu} \rangle$ is a normalized vector and each cartesian component ranges from 0 to 1. In the case of ferromagnets, this measure is enough to conclude whether the system is ordered. A small value of $\vec{\mu}$ indicates a disordered phase and a large value indicates

| | CE-104 | CE-123 | OG-104 | OG-123 |
|---|---|---|---|---|
| $\langle \mu_x \rangle$ | 0.336 | 0.179 | 0.587 | 0.069 |
| $\langle \mu_y \rangle$ | -0.253 | 0.220 | -0.058 | -0.194 |
| $\langle \mu_z \rangle$ | 0.410 | 0.458 | 0.148 | 0.145 |

Table 5.2: The average of the TDM vector orientation (a.u.) along each cartesian axis in the monomer frame.

| | CE-104 | CE-123 | OG-104 | OG-123 |
|---|---|---|---|---|
| $\langle \lvert\mu_x\rvert \rangle$ | 0.558 | 0.389 | 0.824 | 0.159 |
| $\langle \lvert\mu_y\rvert \rangle$ | 0.408 | 0.464 | 0.284 | 0.821 |
| $\langle \lvert\mu_z\rvert \rangle$ | 0.538 | 0.609 | 0.293 | 0.429 |

Table 5.3: The average of the absolute value of the TDM vector (a.u.) along each cartesian axis in the monomer frame.

an ordered phase. However, in the case of antiferromagnets, a small value of $\vec{\mu}$ is not enough to conclude that it is a disordered phase. This is because a perfect antiferromagnet would exhibit negligible average magnetizations.

Table 5.2 shows the average of the orientation vector of TDMs along each cartesian axis in the monomer frame. CE and OG present a qualitative difference as OG has at least one direction that has very small values. Therefore, the small values along $y$-axis in OG-104 and $x$-axis in OG-123 are particularly interesting as they may indicate an antiferromagnetic ordering along those axes. To further investigate this, we computed $\langle |\vec{\mu}| \rangle$ which is similarly defined as Eq. (5.12). Those numbers are presented in Table 5.3. If there is no difference between $\langle |\vec{\mu}| \rangle$ and $\langle \vec{\mu} \rangle$ then the system is a perfect magnet while a significant difference between them indicates a antiferromagnetic system. The $y$-component of OG-104 and the $x$-component of OG-123 show a significant difference and this indicates antiferromagnetism along those axes. On the other hand, other values all indicate spontaneous magnetism to certain degree.

We have investigated a two-body correlation function (or a two-point correlators). The spin-spin correlation function, $C_{\text{spin}}$, reads

$$C_{\text{spin}} = \sum_{\langle \alpha\beta \rangle} \langle \vec{\mu}_\alpha \cdot \vec{\mu}_\beta \rangle = \frac{1}{N_{\text{samples}} N_{\text{neighbors}}} \sum_{i}^{N_{\text{samples}}} \left( \sum_{\langle \alpha\beta \rangle} \vec{\mu}_\alpha^{\,i} \cdot \vec{\mu}_\beta^{\,i} \right). \tag{5.13}$$

We note that $C_{\text{spin}}$ involves only nearest neighbor correlations even though the underlying interaction between spins in our case is long-ranged. This was done on

purpose as the interaction is still dominated by nearest neighbor interactions and it is easier to interpret the physical meaning of $C_{\text{spin}}$ this way. This measure has a range between -1 and 1, where the limit of 1 is a perfect ferromagnetic order, -1 means a perfect antiferromagnetic order, and 0 means no order or a perfect disorder. We also define $C^i_{\text{spin}}$ where $i \in \{x, y, z\}$ to quantify the same types of orders along each cartesian axis which can be trivially defined similarly to Eq. (5.13).

| | CE-104 | CE-123 | OG-104 | OG-123 |
|---|---|---|---|---|
| $C_{\text{spin}}$ | 0.433 | 0.390 | 0.386 | 0.035 |
| $C^x_{\text{spin}}$ | 0.108 | 0.078 | 0.376 | 0.006 |
| $C^y_{\text{spin}}$ | 0.101 | 0.026 | -0.007 | 0.018 |
| $C^z_{\text{spin}}$ | 0.224 | 0.286 | 0.017 | 0.011 |

Table 5.4: Spin-spin correlation functions for each system

Using this measure, in Table 5.4 we see that CE-104, CE-123 and OG-104 are all much more ordered than OG-123. CE-104 exhibits isotropic ferromagnetic ordering. However, CE-123 exhibits ferromagnetic ordering mostly along $z$-axis. Given the results in Table 5.3, CE-123 exhibits non-negligible orientations along $x, y$-axis. Therefore, Table 5.4 suggests that CE-123 is disordered along $x, y$-axis but ferromagnetically ordered along $z$-axis. OG-104 exhibits ferromagnetic ordering along $x$-axis and disorders along $y, z$-axis. As illustrated in Figure 5.5, OG-104 is confined along positive $x$-axis. Therefore, OG-104 is confined and at the same time well-ordered. OG-123 is interesting in the sense that it is disordered along every axis. As suggested in Figure 5.5, it is however confined in space. Although OG-123 is spatially confined by the TMV protein environment, its orientation from one another is almost completely random. In passing we note that OG-104 would be a good future candidate for further theoretical studies as it is spatially well confined and chromophores are ordered so that we would not need to explore the entire phase space.

### 5.3.3 Linear Absorption Spectrum

In Figure 5.6(a), we show simulated linear absorption spectra averaged over the MCMM geometries, using the TDDFT-derived Hamiltonian parameters in Eq. 5.5 for the CE-104 and CE-123 system as described in the Spectral Simulations section. For these simulations, we set $\Delta E_1^{\text{monomer}} = 2.8$ eV (442.8 nm) for all of the Coumarin 343 spectral simulations, which is different from the vacuum TDDFT excitation energy reported in Table 5.1. This results in a global energy shift and was done to shift the simulated spectra to better coincide with the experimental spectra. The choice of

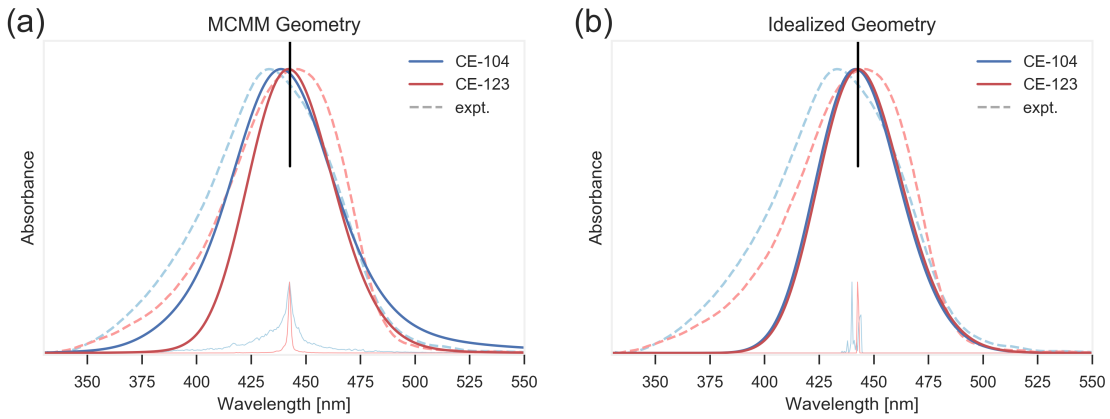


Figure 5.6: Simulations of linear absorption spectra using the TDDFT-improved Hamiltonian parameters in Eq. 5.5. (a) Spectra averaged over the MCMM-geometries (b) spectra of a single idealized, 17-fold symmetric geometry. Dotted lines are the absorption spectra obtained from experiment, and the vertical black line is the monomer excitation energy $\Delta E^{\text{monomer}}$. The line broadening parameter $\sigma$ is set to 0.12 eV. Below these simulated spectra, we show simulations of the same system using $\sigma = 0.01$ eV.

$\Delta E_1^{\text{monomer}}$ does not affect our results since our conclusions are all based on relative energy differences. The line broadening parameter $\sigma$ is set to 0.12 eV for all simulated spectra. At the bottom of these plots, we also show the same spectral simulations with $\sigma$ set to 0.001 eV. Since this broadening value is lower than the resolution of the x-axis, this plot can be interpreted as a histogram of the unbroadened eigenvalue stick spectrum.

The distribution of the sticks in the stick spectrum for the CE-123 system is narrower than that of CE-104, which is due to the fact that the CE-123 geometries have chromophores further apart, and therefore smaller offdiagonal couplings and smaller range in eigenvalues. In the limit of infinite separation, these eigenvalues become degenerate and would yield a delta function. The CE-104 system has a much wider stick spectrum, with non-zero absorption between 400-475 nm. This wide distribution of spectral lines validates our use of using only a gaussian broadening parameter in our simulations, since the coupling between chromophores is much greater than individual chromophores coupling to an environment. The features in the spectra for CE-104 will be dominated by static disorder, leading to significant inhomogeneous broadening.

To see the effect of the chromophore geometries, in Figure 5.6(b) we compute the spectra for an ideal $C_{17h}$ symmetric geometry where the positions and orientations of

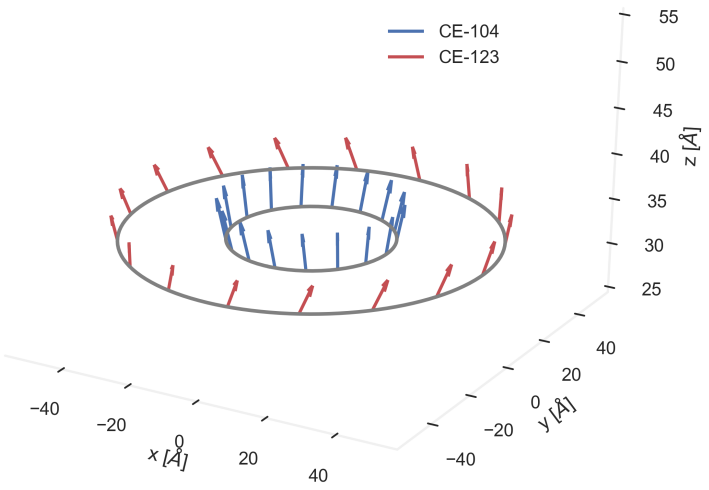


Figure 5.7: Idealized $C_{17h}$ symmetric geometry where the positions and orientations of the chromophores are obtained from the average over all the MCMM configurations. Arrows indicate the orientation of the transition dipole moment. The blue arrows describe the CE-104 system, while the red arrows describe the CE-123 system.

the chromophores are obtained from the average over all the MCMM configurations. The geometry for the top half of the disk is shown for both the CE-104 and CE-123 systems in Figure 5.7. The symmetry of these geometries implies that every nearest-neighbor pair of chromophores has an identical geometry relative to each other, so no pair couples more strongly than any of the others. For the symmetric geometry, the resulting Hamiltonian will yield eigenvalues with a smaller spread, therefore, we see a tighter spectrum for CE-104 in Figure 5.6(b) than in Figure 5.6(a). We find that the simulation using the MCMM-derived geometries is better able to reproduce the blue shift that occurs when going from the CE-123 system to the CE-104 system.

In Table 5.5, we show the Hamiltonian matrix elements for each system, averaged over all 34 sites. For the systems derived from the MCMM geometries, the average is also over all of the geometry configurations. From this table, we see that the average

| | $\langle \varepsilon_i \rangle$ [nm] | $\langle J_{ij} \rangle$ [nm] | $\langle \lvert J_{ij} \rvert \rangle$ [nm] |
|---|---|---|---|
| CE-104 MCMM | 2.842 | $2.00 \times 10^{-3}$ | $6.82 \times 10^{-3}$ |
| CE-123 MCMM | 2.806 | $3.44 \times 10^{-4}$ | $1.28 \times 10^{-3}$ |
| CE-104 symmetric | 2.812 | $9.58 \times 10^{-4}$ | $9.58 \times 10^{-4}$ |
| CE-123 symmetric | 2.800 | $4.53 \times 10^{-6}$ | $4.83 \times 10^{-5}$ |

Table 5.5: Hamiltonian parameters, averaged over all sites and all geometry configurations. $\varepsilon_i$ are the diagonal Hamiltonian matrix elements, and $J_{ij}$ are the offdiagonal Hamiltonian matrix elements. These are obtained from the same systems used to generate spectra in Figure. 5.6

off-diagonal coupling values for both CE-104 and CE-123 are positive. A positive coupling value is characteristic of H-aggregates, which occur when transition dipoles are perpendicular to the intermolecular axis, and aligned parallel to each other[132]. This geometric property is consistent with the orientation distribution histogram in Figure 5.5 - while both CE-104 and CE-123 tend to be disordered, the average orientation is one where the dipole is aligned with the z-axis. H-aggregates also tend to exhibit blue-shifted absorption spectra. This phenomena occurs because the geometric symmetry of H-aggregates renders the energetically favorable exciton states to be optically dark, leaving only the higher energy excitons free to absorb light. While there is still a large amount of static disorder in the system, we find that on average, the CE-104 pigment-protein systems resembles an H-aggregate, while the chromophores of the CE-123 system are situated too far apart to exhibit spectral shifts.

However, it is not just the positive-valued off-diagonal couplings that cause the blue shift. The average site energies ($\varepsilon_i$) for the CE-104 position are also shifted 0.04 eV above the monomer transition energy that we chose (2.842 vs 2.8 eV). While the conventional Frenkel Exciton Hamiltonian does not include any perturbative corrections to the site energies [13], the Hamiltonian parameters we use defined in Eq. 5.2 include corrections to account for the classical Coulomb couplings between chromophores. The distance and orientation dependence of this correction has been throughouly studied in Chapter 3, and Figure 3.10 shows that for H-aggregates, the site energy for Coumarin 343 dimers tends to increase at closer distances.

In Figure 5.8, we plot the same MCMM-derived systems as in Figure 5.6(a), but setting $\varepsilon_i = \Delta E_1^{\text{monomer}}$, and dipole-dipole coupling to calculate all of the offdiagonal matrix elements. We find that the CE-104 simulated spectrum is exhibits much more spectral broadening than the spectra in Figure 5.6. This result is explained in Chapter 3, Figure 3.7, which compares the coupling obtained from the ideal dipole

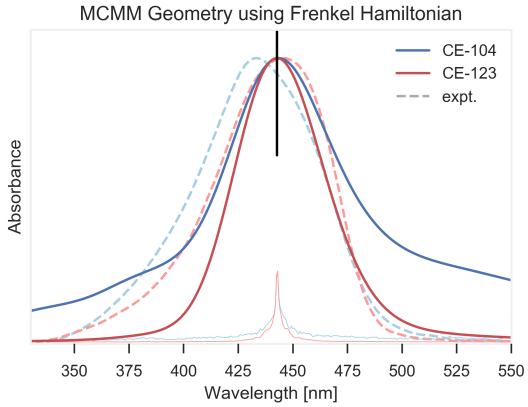


Figure 5.8: The simulated linear absorption spectrum for the MCMM-geometries, using $\Delta E_1^{\text{monomer}}$ for all the diagonal energies, and dipole-dipole coupling for the off-diagonal energies of the Hamiltonian. Refer to Figure 5.6 for an explanation of the other lines.

| | $\lambda^{\text{avg}}_{\text{CE-104}}$ [nm] | $\lambda^{\text{avg}}_{\text{CE-123}}$ [nm] | $\Delta_{\text{avg}}$ [nm] |
|---|---|---|---|
| Experiment [122] | 429.28 | 435.14 | 5.86 |
| MCMM | 438.32 | 442.78 | 4.46 |
| Idealized | 442.42 | 443.60 | 1.18 |

Table 5.6: Average Absorbance. $\Delta_{\text{avg}}$ is the difference between CE-104 and CE-123 average absorbances ($\lambda^{\text{avg}}_{\text{CE-123}} - \lambda^{\text{avg}}_{\text{CE-104}}$).

approximation to one derived from TDDFT. For Coumarin 343 dimers that resemble H-aggregates, the dipole approximation overestimates couplings at close intermolecular separation distances. At 6 $\mathring{A}$ separation, the dipole approximation overestimates the value by factor of 2.5. Figure 5.3 shows that the closest interchromophore distances in the MCMM geometries can be as close as 5 $\mathring{A}$, so it is necessary to use an appropriate Hamiltonian model that can account for the deviations at these close distances. Therefore, we find using the ideal dipole approximation to be unsuitable for modeling our system.

In Table 5.6, we quantify the differences between the spectra in Figure 5.6 by calculating the average absorbance for each spectra:

$$\lambda^{\text{avg}} = \frac{\sum_\lambda \text{Abs}(\lambda) * \lambda}{\sum_\lambda \text{Abs}(\lambda)}. \tag{5.14}$$

We compare the average absorbance for each of the simulations and compare these to the values obtained from experimental spectra [122]. To summarize our results,

the experimental spectrum exhibits a blue shift when going from the CE-123 system to the CE-104 system. While both the simulations using the MCMM geometries and the idealized geometries exhibit a blue shift, the simulation that incorporates disorder is able to match this trend much better. We conclude that the disorder in the geometry of the CE-104 and CE-123 systems is an important feature of these systems, and it is important to account for this disorder in order to model optical properties accurately.

## 5.4 Conclusions

In this work, we present a protocol that generates conformations using a Monte Carlo multiple minima (MCMM) conformation search algorithm, parametrizes a semiempirical tight-binding Hamiltonian based on ab-initio TDDFT calculations and combines those to generate a linear absorption spectrum that can be directly compared to experiments.

In particular, we applied this protocol to study a recently synthesized artificial light harvesting system consisting of chromophores attached to a tobacco mosaic virus (TMV) protein. We studied Coumarin 343 (along with a linker) and Oregon Green 488 attached to the 104 and 123 sites on the TMV protein. The resulting four systems, CE-104, CE-123, OG-104, and OG-123, were studied with MCMM and we obtained a wide array of local minima. We characterized those conformers using the orientation of the transition dipole moment and center-of-mass of dyes attached to the TMV protein. Such a characterization led to a better understanding of structural order and disorder associated with the dyes. CE-104 and CE-123 both exhibit a very broad geometric distribution, which makes any types of theoretical study more or less intractable. OG-104 and OG-123 are relatively spatially well confined, but OG-123 is more disordered than is OG-104 in terms of the spin-spin correlation function discussed in the main text. For future studies, we believe that OG-104 will be likely the easiest system to exhaustively study using theoretical methods.

Lastly, we combine the wide array of conformations found through MCMM with a semiempirical tight-binding Hamiltonian to produce a linear absorption spectrum of CE-104 and CE-123. We observed that it is necessary to account for the proper geometric distribution to properly reproduce the blue shift when going from the CE-123 system to the CE-104 system. Despite the high levels of static disorder in the CE-104 system, our simulations reveal that it exhibits geometric and optical properties that resemble an H-aggregate. We find that the typical Frenkel Exciton Hamiltonian with static site energies and dipole-dipole coupling for the offdiagonal elements is insufficient for modeling the optical properties for this system. The

methods described in this chapter for obtaining more accurate Hamiltonian matrix elements can be used to create a model that better captures the geometric and orientation dependence of these matrix elements, especially at closer intermolecular distances. While this model is more difficult to use than the dipole approximation, once the model is properly fit, it can efficiently generate tight-binding Hamiltonians for arbitrary geometries.

# Chapter 6

# Conclusion

The work presented in this dissertation both evaluates existing models and proposes new theoretical models that can be used to simulate the electronic and optical properties of chromophore aggregates. The Frenkel exciton model Hamiltonian was found to be inadequte in its original formulation when used for the intermolecular distances and orientations found in a prototypical light-harvesting system. We proposed a modified tight-binding Hamiltonian which performs much better at the closer intermolecular distances encountered in these photosynthetic systems. We also quantified the rate and efficiency of charge separation for a chromophore donor-acceptor system using a Lindblad master equation and a tight-binding model that treats electronic excitation transfer and charge separation at the same level of theory. The predictions from this model were able to match the trends found in experimental characterizations of the charge separation rate, and we found that it is important to include higher energy charge-transfer and exciton states to properly model this system. We also studied an artificial photosynthetic system that had been synthesized by attaching chromophores onto the TMV protein. We found that the amount of static disorder in the system is highly dependent on the synthetic choices (choice of chromophore, protein attachment site). It was necessary to account for this disorder in our model, in addition to using a more accurate tight-binding Hamiltonian, in order to properly simulate the linear absorbtion spectra for these systems.

## 6.1 Future Directions

One focus of the work presented in this dissertation was to create models that work well for real experimental systems, while balancing efficiency and accuracy. The Frenkel exciton model is often used to model molecular aggregates due to its

simplicity and ease of use. The approaches that we have presented have an overhead of requiring numerous TDDFT calculations, but once the model is trained on this data, the resulting effective Hamiltonian can be created just as efficiently as the Frenkel exciton model Hamiltonian, for arbitrary starting geometries. We suggest that theoretical studies of photosynthetic systems should consider the assumptions made in the Frenkel exciton model, and evaluate whether their system warrents using a more microscopic treatment of the Hamiltonian.

One future extension of this work would be to combine the techniques for simulating charge separation rates and linear absorption presented in ch. 4 and 5 into a single model. The ability to predict both linear absorption and charge separation in a unified model would be a useful theoretical tool to study artifical photosynthetic systems that include both a light harvesting component and a charge separation component. Such a study would be able to screen potential donor acceptor geometries, and discover the tradeoffs between light absorption and charge separation efficencies.

# References


(1) Blankenship, R. E., *Molecular Mechanisms of Photosynthesis*; Blackwell Science: 2002.

(2) Scholes, G. D. et al. Using coherence to enhance function in chemical and biophysical systems. *Nature* **2017**, *543*, 647–656.

(3) Engel, G. S.; Calhoun, T. R.; Read, E. L.; Ahn, T.-K.; Mancal, T.; Cheng, Y.-C.; Blankenship, R. E.; Fleming, G. R. Evidence for Wavelike Energy Transfer Through Quantum Coherence in Photosynthetic Systems. *Nature* **2007**, *446*, 782–6.

(4) Rozzi, C. A.; Falke, S. M.; Spallanzani, N.; Rubio, A.; Molinari, E.; Brida, D.; Maiuri, M.; Cerullo, G.; Schramm, H.; Christoffers, J.; Lienau, C. Quantum Coherence Controls the Charge Separation in a Prototypical Artificial Light-Harvesting System. *Nat. Commun.* **2013**, *4*, 1602.

(5) Scholes, G. D.; Fleming, G. R.; Olaya-Castro, A.; van Grondelle, R. Lessons From Nature About Solar Light Harvesting. *Nat Chem* **2011**, *3*, 763–774.

(6) Pillai, S.; Ravensbergen, J.; Antoniuk-Pablant, A.; Sherman, B. D.; van Grondelle, R.; Frese, R. N.; Moore, T. a.; Gust, D.; Moore, A. L.; Kennis, J. T. M. Carotenoids as Electron or Excited-State Energy Donors in Artificial Photosynthesis: an Ultrafast Investigation of a Carotenoporphyrin and a Carotenofullerene Dyad. *Phys. Chem. Chem. Phys.* **2013**, *15*, 4775–84.

(7) May, V.; Kuhn, O., *Charge and Energy Transfer Dynamics in Molecular Systems*, 3rd ed.; Wiley-VCH: Weinheim, 2011.

(8) Ishizaki, A.; Calhoun, T. R.; Schlau-Cohen, G. S.; Fleming, G. R. Quantum coherence and its interplay with protein environments in photosynthetic electronic energy transfer. *Physical chemistry chemical physics : PCCP* **2010**, *12*, 7319–7337.

(9) Scholes, G. D. Long-range resonance energy transfer in molecular systems. *Annual Review of Physical Chemistry* **2003**, *54*, 57–87.

(10) Agranovich, V., *Excitations in Organic Solids*; Oxford University Press: 2008.

(11) Knoester, J. In *Proceedings of the International School of Physics "Enrico Fermi" Course CXLIX*, Agranovich, V. M., LaRocca, G. C., Eds.; Amsterdam: IOS Press: 2002, pp 149–186.

(12) Scholes, G. D.; Ms, C.; Fleming, G. R. In *Advances in Chemical Physics*, Berry, R. S., Jortner, J., Eds.; Advances in Chemical Physics, Vol. i; John Wiley & Sons, Inc.: Hoboken, NJ, USA, 2005; Chapter 2, pp 57–129.

(13) Cheng, Y.-C.; Fleming, G. R. Dynamics of Light Harvesting in Photosynthesis. *Annu. Rev. Phys. Chem.* **2009**, *60*, 241–62.

(14) Van Amerongen, H.; Valkunas, L; van Grondelle, R, *Photosynthetic Excitons*; World Scientific: 2000.

(15) Scholes, G. D. Energy Transfer and Spectroscopic Characterization of Multichromophoric Assemblies. *J. Phys. Chem.* **1996**, *100*, 18731–18739.

(16) Cao, J.; Silbey, R. J. Optimization of Exciton Trapping in Energy Transfer Processes. *J. Phys. Chem. A* **2009**, *113*, 13825–38.

(17) Didraga, C.; Klugkist, J. A.; Knoester, J. Optical Properties of Helical Cylindrical Molecular Aggregates: The Homogeneous Limit. *J. Phys. Chem. B* **2002**, *106*, 11474–11486.

(18) Didraga, C.; Pugžlys, A.; Hania, P. R.; von Berlepsch, H.; Duppen, K.; Knoester, J.; Pugz, A.; Berlepsch, H. V. Structure, Spectroscopy, and Microscopic Model of Tubular Carbocyanine Dye Aggregates. *J. Phys. Chem. B* **2004**, *108*, 14976–14985.

(19) Sarovar, M.; Whaley, K. B. Design Principles and Fundamental Trade-Offs in Biomimetic Light Harvesting. *New J. Phys.* **2013**, *15*, 013030.

(20) Scholes, G. D. Quantum-Coherent Electronic Energy Transfer: Did Nature Think of It First? *J. Phys. Chem. Lett.* **2010**, *1*, 2–8.

(21) Collini, E.; Wong, C. Y.; Wilk, K. E.; Curmi, P. M. G.; Brumer, P.; Scholes, G. D. Coherently Wired Light-Harvesting in Photosynthetic Marine Algae at Ambient Temperature. *Nature* **2010**, *463*, 644–647.

(22) Sarovar, M.; Ishizaki, A.; Fleming, G. R.; Whaley, K. B. Quantum Entanglement in Photosynthetic Light-Harvesting Complexes. *Nat. Phys.* **2010**, *6*, 462–467.

(23) Ma, Y.-Z.Y.-Z.; Miller, R. A.; Fleming, G. R.; Francis, M. B. Energy Transfer Dynamics in Light-Harvesting Assemblies Templated by the Tobacco Mosaic Virus Coat Protein. *J. Phys. Chem. B* **2008**, *112*, 6887–92.

(24) Klug, A The Tobacco Mosaic Virus Particle: Structure and Assembly. *Phil. Trans. R. Soc. B* **1999**, *354*, 531–5.

(25) Endo, M.; Fujitsuka, M.; Majima, T. Porphyrin Light-Harvesting Arrays Constructed in the Recombinant Tobacco Mosaic Virus Scaffold. *Chemistry (Weinheim an der Bergstrasse, Germany)* **2007**, *13*, 8660–6.

(26) Nam, Y. S.; Shin, T.; Park, H.; Magyar, A. P.; Choi, K.; Fantner, G.; Nelson, K. A.; Belcher, A. M. Virus-Templated Assembly of Porphyrins into Light-Harvesting Nanoantennae. *J. Am. Chem. Soc.* **2010**, *132*, 1462–3.

(27) Miller, R. A.; Presley, A. D.; Francis, M. B. Self-Assembling Light-Harvesting Systems from Synthetically Modified Tobacco Mosaic Virus Coat Proteins. *J. Am. Chem. Soc.* **2007**, *129*, 3104–9.

(28) Witus, L. S.; Francis, M. B. Using Synthetically Modified Proteins to Make New Materials. *Acc. Chem. Res.* **2011**, *44*, 774–83.

(29) Scholes, G. D.; Rumbles, G. Excitons in Nanoscale Systems. *Nat. Mater.* **2006**, *5*, 683–696.

(30) Krueger, B. P.; Scholes, G. D.; Fleming, G. R. Calculation of Couplings and Energy-Transfer Pathways between the Pigments of LH2 by the ab Initio Transition Density Cube Method. *J. Phys. Chem. B* **1998**, *102*, 5378–5386.

(31) Kasha, M.; Rawls, H. R.; Ashraf El-Bayoumi, M. The Exciton Model in Molecular Spectroscopy. *Pure Appl. Chem.* **1965**, *11*, 371–392.

(32) Howard, I. A.; Zutterman, F; Deroover, G; Lamoen, D; Van Alsenoy, C. Approaches to Calculation of Exciton Interaction Energies for a Molecular Dimer. *J. Phys. Chem. B* **2004**, *108*, 19155–19162.

(33) Muñoz Losa, A.; Curutchet, C.; Krueger, B. P.; Hartsell, L. R.; Mennucci, B. Fretting about FRET: Failure of the Ideal Dipole Approximation. *Biophys. J.* **2009**, *96*, 4779–88.

(34) Scholes, G. D.; Jordanides, X. J.; Fleming, G. R. Adapting the Förster Theory of Energy Transfer for Modeling Dynamics in Aggregated Molecular Assemblies. *J. Phys. Chem. B* **2001**, *105*, 1640–1651.

(35) Madjet, M. E.; Abdurahman, a; Renger, T Intermolecular Coulomb Couplings from Ab Initio Electrostatic Potentials: Application to Optical Transitions of Strongly Coupled Pigments in Photosynthetic Antennae and Reaction Centers. *J. Phys. Chem. B* **2006**, *110*, 17268–81.

(36) Hsu, C.-P.; Fleming, G. R.; Head-Gordon, M.; Head-Gordon, T. Excitation Energy Transfer in Condensed Media. *J. Chem. Phys.* **2001**, *114*, 3065.

(37) Curutchet, C.; Scholes, G. D.; Mennucci, B.; Cammi, R. How Solvent Controls Electronic Energy Transfer and Light Harvesting: Toward a Quantum-Mechanical Description of Reaction Field and Screening Effects. *J. Phys. Chem. B* **2007**, *111*, 13253–13265.

(38) Sinnokrot, M. O.; Sherrill, C. D. High-Accuracy Quantum Mechanical Studies of Pi-Pi Interactions in Benzene Dimers. *J. Phys. Chem. A* **2006**, *110*, 10656–10668.

(39) Fink, R. F.; Pfister, J; Schneider, A; Zhao, H; Engels, B Ab Initio Configuration Interaction Description of Excitation Energy Transfer Between Closely Packed Molecules. *Chem. Phys.* **2008**, *343*, 353–361.

(40) Fink, R. F.; Pfister, J.; Zhao, H. M.; Engels, B. Assessment of Quantum Chemical Methods and Basis Sets for Excitation Energy Transfer. *Chem. Phys.* **2008**, *346*, 275–285.

(41) Zhao, H. M.; Pfister, J.; Settels, V.; Renz, M.; Kaupp, M.; Dehm, V. C.; Würthner, F.; Fink, R. F.; Engels, B. Understanding Ground- and Excited-State Properties of Perylene Tetracarboxylic Acid Bisimide Crystals by Means of Quantum Chemical Computations. *J. Am. Chem. Soc.* **2009**, *131*, 15660–15668.

(42) Liu, W.; Settels, V.; Harbach, P. H. P.; Dreuw, A.; Fink, R. F.; Engels, B. Assessment of TD-DFT- and TD-HF-based Approaches for the Prediction of Exciton Coupling Parameters, Potential Energy Curves, and Electronic Characters of Electronically Excited Aggregates. *J. Comput. Chem.* **2011**, *32*, 1971–1981.

(43) Stephens, P. J.; Devlin, F. J.; Chabalowski, C. F.; Frisch, M. J. Ab Initio Calculation of Vibrational Absorption and Circular Dichroism Spectra Using Density Functional Force Fields. *J. Phys. Chem.* **1994**, *98*, 11623.

(44) Ditchfield, R.; Hehre, W. J.; Pople, J. A. Self-Consistent Molecular-Orbital Methods. IX. An Extended Gaussian-Type Basis for Molecular-Orbital Studies of Organic Molecules. *J. Chem. Phys.* **1971**, *54*, 724.

(45) Hehre, W. J.; Ditchfield, R.; Pople, J. A. Self—Consistent Molecular Orbital Methods. XII. Further Extensions of Gaussian—Type Basis Sets for Use in Molecular Orbital Studies of Organic Molecules. *J. Chem. Phys.* **1972**, *56*, 2257.

(46) Hariharan, P.; Pople, J. The Influence of Polarization Functions on Molecular Orbital Hydrogenation Energies. *Theo. Chim. Acta* **1973**, *28*, 213.

(47) Runge, E.; Gross, E. K. U. Density-Functional Theory for Time-Dependent Systems. *Phys. Rev. Lett.* **1984**, *52*, 997.

(48) Gross, E.; Kohn, W. In *Density Functional Theory of Many-Fermion Systems*, Löwdin, P.-O., Ed.; Adv. Quant. Chem. Vol. 21; Academic Press: 1990, pp 255 –291.

(49) Zhao, Y.; Truhlar, D. G. Density Functional for Spectroscopy: No Long-Range Self-Interaction Error, Good Performance for Rydberg and Charge-Transfer States, and Better Performance on Average than B3LYP for Ground States. *J. Phys. Chem. A* **2006**, *110*, 13126.

(50) Peverati, R.; Truhlar, D. G. Improving the Accuracy of Hybrid Meta-GGA Density Functionals by Range Separation. *J. Phys. Chem. Lett.* **2011**, *2*, 2810–2817.

(51) Peverati, R.; Truhlar, D. G. M11-L: A Local Density Functional that Provides Improved Accuracy for Electronic Structure Calculations in Chemistry and Physics. *J. Phys. Chem. Lett.* **2012**, *3*, 117–124.

(52) Perdew, J. P.; Burke, K.; Ernzerhof, M. Generalized Gradient Approximation Made Simple. *Phys. Rev. Lett.* **1996**, *77*, 3865–3868.

(53) Perdew, J. P.; Burke, K.; Ernzerhof, M. Generalized Gradient Approximation Made Simple [Phys. Rev. Lett. 77, 3865 (1996)]. *Phys. Rev. Lett.* **1997**, *78*, 1396–1396.

(54) Clark, T.; Chandrasekhar, J.; Spitznagel, G. W.; Schleyer, P. V. R. Efficient Diffuse Function-Augmented Basis Sets For Anion Calculations. III. The 3-21+G Basis Set for First-Row Elements, Li-F. *J. Comput. Chem.* **1983**, *4*, 294.

(55) Krishnan, R.; Binkley, J. S.; Seeger, R.; Pople, J. A. Self-Consistent Molecular Orbital Methods. XX. A Basis Set for Correlated Wave Functions. *J. Chem. Phys.* **1980**, *72*, 650.

(56) Frisch, M. J.; Pople, J. A.; Binkley, J. S. Self-Consistent Molecular Orbital Methods 25. Supplementary Functions for Gaussian Basis Sets. *J. Chem. Phys.* **1984**, *80*, 3265.

(57) Piecuch, P.; Kucharski, S. A.; Kowalski, K.; Musiał, M. Efficient Computer Implementation of the Renormalized Coupled-Cluster Methods: The R-CCSD[T], R-CCSD(T), CR-CCSD[T], and CR-CCSD(T) Approaches. *Comput. Phys. Commun.* **2002**, *149*, 71.

(58) Kowalski, K.; Piecuch, P. New Coupled-Cluster Methods With Singles, Doubles, and Noniterative Triples for High Accuracy Calculations of Excited Electronic States. *J. Chem. Phys.* **2004**, *120*, 1715.

(59) Wloch, M.; Gour, J. R.; Kowalski, K.; Piecuch, P. Extension of Renormalized Coupled-Cluster Methods Including Triple Excitations to Excited Electronic States of Open-Shell Molecules. *J. Chem. Phys.* **2005**, *122* 214107, 214107.

(60) Ivanic, J.; Ruedenberg, K. Identification of Deadwood in Configuration Spaces Through General Direct Configuration Interaction. *Theo. Chem. Acc.* **2001**, *106*, 339.

(61) Cossi, M.; Barone, V. Time-Dependent Density Functional Theory for Molecules in Liquid Solutions. *J. Chem. Phys.* **2001**, *115*, 4708.

(62) Tawada, Y.; Tsuneda, T.; Yanagisawa, S.; Yanai, T.; Hirao, K. A Long-Range-Corrected Time-Dependent Density Functional Theory. *J. Chem. Phys.* **2004**, *120*, 8425.

(63) Schmidt, M. W.; Baldridge, K. K.; Boatz, J. A.; Elbert, S. T.; Gordon, M. S.; Jensen, J. H.; Koseki, S.; Matsunaga, N.; Nguyen, K. A.; Su, S.; Windus, T. L.; Dupuis, M.; Montgomery, J. A. General Atomic and Molecular Electronic Structure System. *J. Comput. Chem.* **1993**, *14*, 1347.

(64) M.S.Gordon; M.W.Schmidt In *Theory and Applications of Computational Chemistry, the First Forty Years*, C.E.Dykstra, G.Frenking, K.S.Kim, G.E.Scuseria, Eds.; Elsevier: 2005, p 1167.

(65) Shao, Y. et al. Advances in Methods and Algorithms in a Modern Quantum Chemistry Program Package. *Phys. Chem. Chem. Phys.* **2006**, *8*, 3172.

(66) Löwdin, P.-O. Quantum Theory of Many-Particle Systems. I. Physical Interpretations by Means of Density Matrices, Natural Spin-Orbitals, and Convergence Problems in the Method of Configurational Interaction. *Physical Review* **1955**, *97*, 1474–1489.

(67) Davydov, A. S. The Theory of Molecular Excitons. *Sov. Phys. Usp.* **1964**, *7*, 145–178.

(68) Agranovich, V. M.; Basko, D. M. Frenkel excitons beyond the Heitler-London approximation. *J. Chem. Phys.* **2000**, *112*, 8156–8162.

(69) Mulliken, R. S. Electronic Population Analysis on LCAO[Single Bond]MO Molecular Wave Functions. I. *J. Chem. Phys.* **1955**, *23*, 1833.

(70) Madjet, M. E.; Abdurahman, A; Renger, T. Intermolecular Coulomb Couplings from Ab Initio Electrostatic Potentials: Application to Optical Transitions of Strongly Coupled Pigments in Photosynthetic Antennae and Reaction Centers. *J. Phys. Chem. B* **2006**, *110*, 17268–17281.

(71) Muh, F.; Madjet, M. E.; Adolphs, J; Abdurahman, A; Rabenstein, B; Ishikita, H; Knapp, E.-W.; Renger, T. $\alpha$-Helices Direct Excitation Energy Flow in the Fenna-Matthews-Olson Protein. *Proc. Nat. Acad. Sc.* **2007**, *104*, 16862.

(72) Dreuw, A.; Head-Gordon, M. Failure of Time-Dependent Density Functional Theory for Long-Range Charge-Transfer Excited States: the Zincbacteriochlorin-Bacteriochlorin and Bacteriochlorophyll-Spheroidene Complexes. *J. Am. Chem. Soc.* **2004**, *126*, 4007–16.

(73) Pan, F.; Gao, F.; Liang, W.; Zhao, Y. Nature of Low-Lying Excited States in H-Aggregated Perylene Bisimide Dyes: Results of TD-LRC-DFT and the Mixed Exciton Model. *J. Phys. Chem. B* **2009**, *113*, 14581–7.

(74) Novoderezhkin, V. I.; Yakovlev, A. G.; van Grondelle, R.; Shuvalov, V. A. Coherent Nuclear and Electronic Dynamics in Primary Charge Separation in Photosynthetic Reaction Centers: a Redfield Theory Approach. *J. Phys. Chem. B* **2004**, *108*, 7445–7457.

(75) Liang, Y.; Xu, Z.; Xia, J.; Tsai, S.-T.; Wu, Y.; Li, G.; Ray, C.; Yu, L. For the Bright Future-Bulk Heterojunction Polymer Solar Cells with Power Conversion Efficiency of 7.4%. *Adv. Mater.* **2010**, *22*, E135–E138.

(76) Lin, Y.; Li, Y.; Zhan, X. Small Molecule Semiconductors for High-Efficiency Organic Photovoltaics. *Chem. Soc. Rev.* **2012**, *41*, 4245–4272.

(77) Chen, J. D.; Cui, C.; Li, Y. Q.; Zhou, L.; Ou, Q. D.; Li, C.; Li, Y.; Tang, J. X. Single-Junction Polymer Solar Cells Exceeding 10% Power Conversion Efficiency. *Adv. Mater.* **2015**, *27*, 1035–1041.

(78) You, J.; Dou, L.; Yoshimura, K.; Kato, T.; Ohya, K.; Moriarty, T.; Emery, K.; Chen, C.-C.; Gao, J.; Li, G.; Yang, Y. *Nat. Commun.*

(79) Janssen, R. A. J.; Nelson, J. Factors Limiting Device Efficiency in Organic Photovoltaics. *Adv. Mater.* **2013**, *25*, 1847–1858.

(80) Silinsh, E.; Capek, V., *Organic Molecular Crystals: Interaction, Localization, and Transport Phenomena*; AIP: Melville, 1994.

(81) Dunlap, W. C.; Watters, R. L. Direct Measurement of the Dielectric Constants of Silicon and Germanium. *Phys. Rev.* **1953**, *92*, 1396–1397.

(82) Bardeen, C. J. The Structure and Dynamics of Molecular Excitons. *Annu. Rev. Phys. Chem.* **2014**, *65*, 127–148.

(83) Knupfer, M Exciton Binding Energies in Organic Semiconductors. *Appl. Phys. A* **2003**, *77*, 623–626.

(84) Lakhwani, G.; Rao, A.; Friend, R. H. Bimolecular Recombination in Organic Photovoltaics. *Annu. Rev. Phys. Chem.* **2014**, *65*, 557–581.

(85) Dennler, G.; Scharber, M. C.; Brabec, C. J. Polymer-Fullerene Bulk-Heterojunction Solar Cells. *Adv. Mater.* **2009**, *21*, 1323–1338.

(86) Jørgensen, M.; Norrman, K.; Krebs, F. C. Stability/Degradation of Polymer Solar Cells. *Sol. Energ. Mat. Sol. C.* **2008**, *92*, 686–714.

(87) Gorczak, N.; Tarkuç, S.; Renaud, N.; Houtepen, A. J.; Eelkema, R.; Siebbeles, L. D. A.; Grozema, F. C. Different Mechanisms for Hole and Electron Transfer along Identical Molecular Bridges: The Importance of the Initial State Delocalization. *J. Phys. Chem. A* **2014**, *118*, 3891–3898.

(88) Iagatti, A.; Cupellini, L.; Biagiotti, G.; Caprasecca, S.; Fedeli, S.; Lapini, A.; Ussano, E.; Cicchi, S.; Foggi, P.; Marcaccio, M.; Mennucci, B.; Di Donato, M. Efficient Photoinduced Charge Separation in a BODIPY-$C_{60}$ Dyad. *J. Phys. Chem. C* **2016**, *120*, 16526–16536.

(89) Liu, L.; Eisenbrandt, P.; Roland, T.; Polkehn, M.; Schwartz, P.-O.; Bruchlos, K.; Omiecienski, B.; Ludwigs, S.; Leclerc, N.; Zaborova, E.; Leonard, J.; Mery, S.; Burghardt, I.; Haacke, S. Controlling Charge Separation and Recombination by Chemical Design in Donor-Acceptor Dyads. *Phys. Chem. Chem. Phys.* **2016**, *18*, 18536–18548.

(90) Gelinas, S.; Rao, A.; Kumar, A.; Smith, S. L.; Chin, A. W.; Clark, J.; van der Poll, T. S.; Bazan, G. C.; Friend, R. H. Ultrafast Long-Range Charge Separation in Organic Semiconductor Photovoltaic Diodes. *Science* **2014**, *343*, 512–516.

(91) Kaake, L. G.; Moses, D.; Heeger, A. J. Coherence and Uncertainty in Nanostructured Organic Photovoltaics. *J. Phys. Chem. Lett.* **2013**, *4*, 2264–2268.

(92) Guo, J.; Ohkita, H.; Benten, H.; Ito, S. Charge Generation and Recombination Dynamics in Poly(3-hexylthiophene)/Fullerene Blend Films with Different Regioregularities and Morphologies. *J. Am. Chem. Soc.* **2010**, *132*, 6154–6164.

(93) Marsh, R. A.; Hodgkiss, J. M.; Albert-Seifried, S.; Friend, R. H. Effect of Annealing on P3HT:PCBM Charge Transfer and Nanoscale Morphology Probed by Ultrafast Spectroscopy. *Nano Lett.* **2010**, *10*, 923–930.

(94) Grancini, G; Maiuri, M; Fazzi, D; Petrozza, A; Egelhaaf, H.-J.; Brida, D; Cerullo, G; Lanzani, G Hot Exciton Dissociation in Polymer Solar Cells. *Nat. Mater.* **2013**, *12*, 29–33.

(95) Whaley, K. B.; Kocherzhenko, A. A.; Nitzan, A. Coherent and Diffusive Time Scales for Exciton Dissociation in Bulk Heterojunction Photovoltaic Cells. *J. Phys. Chem. C* **2014**, *118*, 27235–27244.

(96) Shen, X.; Han, G.; Fan, D.; Xie, Y.; Yi, Y. Hot Charge-Transfer States Determine Exciton Dissociation in the DTDCTB/$C_{60}$ Complex for Organic Solar Cells: A Theoretical Insight. *J. Phys. Chem. C* **2015**, *119*, 11320–11326.

(97) Shao, Y. et al. Advances in Molecular Quantum Chemistry Contained in the Q-Chem 4 Program Package. *Mol. Phys.* **2015**, *113*, 184–215.

(98) Maitra, N. T.; Zhang, F.; Cave, R. J.; Burke, K. Double Excitations Within Time-Dependent Density Functional Theory Linear Response. *J. Chem. Phys.* **2004**, *120*, 5932–5937.

(99) McHugh, A. J.; Gouterman, M.; Weiss, C. Porphyrins XXIV. Energy, Oscillator Strength, and Zeeman Splitting Calculations (SCMO-CI) for Phthalocyanine, Porphyrins, and Related Ring Systems. *Theor. Chim. Acta* **1972**, *24*, 346–370.

(100) Te Velde, G.; Bickelhaupt, F. M.; Baerends, E. J.; Fonseca Guerra, C.; van Gisbergen, S. J. a.; Snijders, J. G.; Ziegler, T. Chemistry with ADF. *J. Comput. Chem.* **2001**, *22*, 931–967.

(101) Senthilkumar, K.; Grozema, F. C.; Bickelhaupt, F. M.; Siebbeles, L. D. A. Charge Transport in Columnar Stacked Triphenylenes: Effects of Conformational Fluctuations on Charge Transfer Integrals and Site Energies. *J. Chem. Phys.* **2003**, *119*, 9809.

(102) Wen, S.-H.; Li, A.; Song, J.; Deng, W.-Q.; Han, K.-L.; Goddard, W. A. First-Principles Investigation of Anistropic Hole Mobilities in Organic Semiconductors. *J. Phys. Chem. B* **2009**, *113*, 8813–8819.

(103) Kocherzhenko, A. A.; Whaley, K. B.; Sforazzini, G.; Anderson, H. L.; Wykes, M.; Beljonne, D.; Grozema, F. C.; Siebbeles, L. D. A. Effects of the Environment on Charge Transport in Molecular Wires. *J. Phys. Chem. C* **2012**, *116*, 25213–25225.

(104) Newton, M. D. Quantum Chemical Probes of Electron-Transfer Kinetics: the Nature of Donor-Acceptor Interactions. *Chem. Rev.* **1991**, *91*, 767–792.

(105) Ishizaki, A.; Fleming, G. R. Theoretical Examination of Quantum Coherence in a Photosynthetic System at Physiological Temperature. *Proc. Natl. Acad. Sci. USA* **2009**, *106*, 17255–17260.

(106) Jesenko, S.; Žnidarič, M. Excitation Energy Transfer Efficiency: Equivalence of Transient and Stationary Setting and the Absence of Non-Markovian Effects. *J. Chem. Phys.* **2013**, *138*, 174103.

(107) Kocherzhenko, A. A.; Lee, D.; Forsuelo, M. A.; Whaley, K. B. Coherent and Incoherent Contributions to Charge Separation in Multi-Chromophore Systems. *J. Phys. Chem. C* **2015**, *119*, 7590–7603.

(108) Lindblad, G On the Generators of Quantum Dynamical Semigroups. *Commun. Math. Phys.* **1976**, *48*, 119–130.

(109) Miller, A.; Abrahams, E. Impurity Conduction at Low Concentrations. *Phys. Rev.* **1960**, *120*, 745–755.

(110) Castro, A.; Appel, H.; Oliveira, M.; Rozzi, C. A.; Andrade, X.; Lorenzen, F.; Marques, M. A. L.; Gross, E. K. U.; Rubio, A. Octopus: a Tool for the Application of Time-Dependent Density Functional Theory. *Phys. Status Solidi B* **2006**, *243*, 2465–2488.

(111) Perdew, J. P. and Zunger, A. Self-Interaction Correction to Density-Functional Approximations for Many-Electron Systems. *Phys. Rev. B* **1981**, *23*, 5048–5079.

(112) Baumgratz, T.; Cramer, M.; Plenio, M. B. Quantifying Coherence. *Phys. Rev. Lett.* **2014**, *113*, 1–5.

(113) Aurenhammer, F. Voronoi Diagrams—a Survey of a Fundamental Geometric Data Structure. *ACM Comput. Surv.* **1991**, *23*, 345–405.

(114) Blankenship, R. E., *Molecular Mechanisms of Photosynthesis*, Second; Chichester, UK: Wiley-Blackwell: 2014.

(115) Van Amerongen, H.; Valkunas, L.; Van Grondelle, R., *Photosynthetic excitons*; World Scientific: 2000.

(116) McDermott, G.; Prince, S.; Freer, A.; Hawthornthwaite-Lawless, A.; Papiz, M.; Cogdell, R.; Isaacs, N. Crystal structure of an integral membrane light-harvesting complex from photosynthetic bacteria. *Nature* **1995**, *374*, 517–521.

(117) Ganapathy, S.; Oostergetel, G. T.; Wawrzyniak, P. K.; Reus, M.; Chew, A. G. M.; Buda, F.; Boekema, E. J.; Bryant, D. A.; Holzwarth, A. R.; de Groot, H. J. Alternating syn-anti bacteriochlorophylls form concentric helical nanotubes in chlorosomes. *Proceedings of the National Academy of Sciences* **2009**, *106*, 8525–8530.

(118) Gilat, S. L.; Adronov, A.; Frechet, J. M. Light harvesting and energy transfer in novel convergently constructed dendrimers. *Angewandte Chemie International Edition* **1999**, *38*, 1422–1427.

(119) Kim, J.; McQuade, D. T.; Rose, A.; Zhu, Z.; Swager, T. M. Directing energy transfer within conjugated polymer thin films. *Journal of the American Chemical Society* **2001**, *123*, 11488–11489.

(120) Choi, M.-S.; Yamazaki, T.; Yamazaki, I.; Aida, T. Bioinspired molecular design of light-harvesting multiporphyrin arrays. *Angewandte Chemie International Edition* **2004**, *43*, 150–158.

(121) Wang, Z.; Medforth, C. J.; Shelnutt, J. A. Porphyrin nanotubes by ionic self-assembly. *Journal of the American Chemical Society* **2004**, *126*, 15954–15955.

(122) Finley, D. Synthesis and Development of Viral Capsid Templated Light Harvesting Systems., PhD, UC Berkeley, 2014, p 110.

(123) Kaminski, G. A.; Friesner, R. A.; Tirado-Rives, J.; Jorgensen, W. L. Evaluation and reparametrization of the OPLS-AA force field for proteins via comparison with accurate quantum chemical calculations on peptides. *Journal of Physical Chemistry B* **2001**, *105*, 6474–6487.

(124) MacroModel., New York, NY, USA, 2012.

(125) Polak, E.; Ribiere, G. Note sur la convergence de méthodes de directions conjuguées. *ESAIM: Mathematical Modelling and Numerical Analysis* **1969**, DOI: `Zbl0174.47906`.

(126) Becke, A. D. Density-functional thermochemistry. III. The role of exact exchange. *The Journal of Chemical Physics* **1993**, *98*, 5648–5652.

(127) Petersson, G. A.; Bennett, A.; Tensfeldt, T. G.; Al-Laham, M. A.; Shirley, W. A.; Mantzaris, J. A complete basis set model chemistry. I. The total energies of closed-shell atoms and hydrides of the first-row elements. *The Journal of Chemical Physics* **1988**, *89*, 2193–2218.

(128) Petersson, G. A.; Al-Laham, M. A. A complete basis set model chemistry. II. Open-shell systems and the total energies of the first-row atoms. *The Journal of Chemical Physics* **1991**, *94*, 6081–6090.

(129) Shao, Y. et al. Advances in molecular quantum chemistry contained in the Q-Chem 4 program package. *Mol. Phys.* **2015**, *113*, 184–215.

(130) Koch, H.; Kobayashi, R.; De Merás, A. S.; Jørgensen, P. Calculation of size-intensive transition moments from the coupled cluster singles and doubles linear response function. *The Journal of Chemical Physics* **1994**, *100*, 4393–4400.

(131) Lee, D.; Greenman, L.; Sarovar, M.; Whaley, K. B. Ab initio calculation of molecular aggregation effects: A coumarin-343 case study. *Journal of Physical Chemistry A* **2013**, *117*, 11072–11085.

(132) Knoester, J. Modeling the optical properties of excitons in linear and tubular J-aggregates. *International Journal of Photoenergy* **2006**, *2006*, 1–10.